COLD TARGET RECOIL ION MOMENTUM SPECTROSCOPY: A 'MOMENTUM MICROSCOPE' TO VIEW ATOMIC COLLISION DYNAMICS

R. DÖRNER[a], V. MERGEL[a], O. JAGUTZKI[a], L. SPIELBERGER[a], J. ULLRICH[b], R. MOSHAMMER[b], H. SCHMIDT-BÖCKING[a]

[a] *Insitut für Kernphysik, Universität Frankfurt, August Euler Str. 6, D60486 Frankfurt, Germany*
[b] *Fakultät für Physik, Universität Freiburg, Hermann-Herder-Str. 3, D79104 Freiburg, Germany*

ELSEVIER

AMSTERDAM – LAUSANNE – NEW YORK – OXFORD – SHANNON – TOKYO

ELSEVIER

Physics Reports 330 (2000) 95–192

PHYSICS REPORTS

www.elsevier.com/locate/physrep

Cold Target Recoil Ion Momentum Spectroscopy: a 'momentum microscope' to view atomic collision dynamics

R. Dörner[a,*], V. Mergel[a], O. Jagutzki[a], L. Spielberger[a], J. Ullrich[b], R. Moshammer[b], H. Schmidt-Böcking[a]

[a]*Institut für Kernphysik, Universität Frankfurt, August Euler Str. 6, D60486 Frankfurt, Germany*
[b]*Fakultät für Physik, Universität Freiburg, Hermann-Herder-Str. 3, D79104 Freiburg, Germany*

Received September 1999; editor: J. Eichler

Contents

Abstract

Cold Target Recoil Ion Momentum Spectroscopy (COLTRIMS) is a novel momentum space imaging technique for the investigation of the dynamics of ionizing ion, electron or photon impact reactions with atoms or molecules. It allows the measurement of the previously undetectable small three dimensional

* Corresponding author.
E-mail address: doerner@hsb.uni-frankfurt.de (R. Dörner)

PII: S0370-1573(99)00109-X

momentum vector of the recoiling target ion created in those reactions with high resolution and 4π solid angle. Combined with novel 4π electron momentum analysers it is a momentum microscope for kinematically complete scattering experiments. We review the technical development, outline the kinematics of atomic reactions from the perspective of the recoil ion, and give an overview of the studies performed with this technique. These studies yield kinematically complete pictures of the correlated motion of the fragments of atomic and molecular breakup processes, unprecedented in resolution, detail and completeness. The multiple-dimensional momentum-space images often directly unveil the physical mechanism underlying the many-particle transitions investigated. The experiments reviewed here include reactions of single and multiple capture and ionization induced by keV proton to GeV/u U^{92+} impact, electron and antiproton impact ionization as well as single and double ionization by photoabsorbtion and Compton scattering from threshold to 100 keV. We give an outlook on the exciting future prospects of the method for atomic physics and other fields of science.

PACS: 34.50.Fa; 34.70. + e; 32.80.Cy; 31.25. − v; 39.30. + w; 39.90. + d

Keywords: Recoil ion; Ionization; Imaging; Spectroscopy; Ion–atom collisions; Photoionization

1. Introduction

Stationary systems in which the interaction potential is exactly known, can be described by quantum mechanics with an extremely high precision. For the energy eigenvalues, the central stationary observable, nearly perfect agreement between experiment and theory has been obtained (see, e.g. [1–8]). *Dynamical many-body systems* on the other hand are still a major challenge for theory and experiment. Today they are the basic issue of many fields of physics such as solid state, nuclear and atomic physics. The last is in the fortunate situation that in atomic systems the interaction potential is exactly known. Thus all disagreement between theory and experiment in this field can be attributed to the many-body aspects and the dynamics of the problem. This makes it even more surprising that such apparently simple problems as the emission of a single electron from an atom by slow charged-particle impact or the emission of two electrons by absorption or Compton scattering of a single photon still challenge theory and experiment. This puzzling lack of understanding of the dynamics of many-body systems is in troubling contrast to the importance of such systems for our everyday world. Structure and evolution of our macroscopic world is to a large extent determined by the dynamics of many-electron processes. They are responsible for many solid state effects such as superconductivity but most prominently they govern and fuel chemical reactions and all biological systems.

Atomic and molecular many-particle reactions are characterized by fully differential cross-sections (FDCS), i.e. cross-sections differential in all observables of the final-state. In an ionization process this typically corresponds to the vector momenta, spins and internal excitation of all reaction products. Such FDCS provide the most stringent test for theory. Any integration over observables often masks important characteristics of the process. In turn, experimental FDCS in the best case directly unveil mechanisms of the many-particle transition. The lack of experimental data on such important details of simple and hence fundamental atomic reactions has for long delayed the development of many-particle collision theory. The goal of Cold Target Recoil Ion Momentum Spectroscopy COLTRIMS is to provide a tool for kinematically complete studies of three- and more-particle atomic collision systems. By kinematically complete we mean that the momenta (and thus angle and energy) of all involved particles are observed in coincidence but the spin is not determined.[1]

For electron impact target single ionization (so called (e,2e)-experiments), systematic experimental and theoretical studies of FDCS exist (see [9–11] for reviews). For target double ionization induced by electron impact so far only very few complete differential cross sections (see [11] for a review and [12–18]) have been published. These data typically view a very small fraction of the final state momentum space. In the field of photoionization tremendous progress has been made in the recent years. Following the pioneering work of Schwarzkopf et al. [19], experimental data for FDCS for double ionization of He have been obtained by several groups [19–27].

All these data have been measured using traditional electron-spectroscopy techniques. To yield sufficiently high resolution for the momentum of the ejected electron, the solid angle Ω of the electron spectrometer is strongly limited, typically to less than 10^{-3} of 4π. In a two- or even

[1] Despite of its importance, we neglect the spin for the rest of this review. The lack of efficient spin-sensitive electron detectors up to today is prohibitive for spin selective many-particle coincidence experiments.

three-electron coincidence experiment the total coincidence efficiency is thus extremely small (10^{-8}). This explains why, so far, systematic investigations of FDCS could be performed only for a few many-particle reactions. In addition, the low counting rate and the geometry of the experimental setup mostly restricted those studies to specific kinematical conditions (e.g. all emerging particles in one plane). Obtaining a desirable overview over the complete final state with this techniques would in general require hundreds of separate experiments (see [28] for such an attempt in (e,2e)-experiments).

In this paper we review a rapid development of a new experimental approach, the COLTRIMS-technique, which overcame many of these problems on a basic level (for earlier reviews on this field see [29–33]). The experimental solution is an imaging technique using a well localized reaction zone and electromagnetic fields to guide all charged fragments towards large-area position- and time-sensitive detectors. From the measurement of the time-of-flight and the position of impact for each particle its momentum vector can be determined. Such an imaging technique has first been used for measuring the ion momenta from atomic reactions and has soon been generalized to electron detection as well.

For an atomic reaction it is for at least three reasons particularly desirable to determine the vector momentum of the recoiling ion. First, the charge state of the ion gives the multiplicity of the process. Second, there are many reactions of charged particles or photons with atoms where the momentum imparted to the ion gives unique information on the dynamical mechanism of the reaction. The measurement of the ion momentum alone allows, e.g. already the separation of Compton scattering from photo absorption, the identification of the electron–electron interaction between two centers or higher-order processes in transfer ionization or the determination of the final state of a capture reaction. These and many more examples of the richness of information inherent in the ionic momentum will be discussed in detail in Sections 4 and 5. Third, for a kinematically complete experiment with n particles in the final state, it is necessary to measure $3n-3$ momentum components ($3n-4$ if the Q-value is known). The remaining 3(4) momenta can be inferred from the others by exploiting the momentum- and energy-conservation laws. In fast ion impact atomic reactions the projectile suffers typically a very small relative momentum change. Only for very selective collisions systems this momentum change could be measured [34–36]. For reactions like 3.6 MeV Ni^{24+} on He (see Section 4.2.6) for example the energy loss of the projectile ($\Delta E/E$) is in the range of 10^{-7} and the typical scattering angle leads to a deflection in the range of 1 mm over 1 km (μrad). Thus for such fast heavy particle collisions the coincident detection of ion and electron momenta gives, via momentum conservation, the only practical access to the projectile momentum change and thus to a kinematically complete experiment. Historically this problem of the unmeasurably small projectile momentum change motivated the development of the first spectrometer for measuring transverse momenta of recoil ions [37].

The idea of such a recoil ion momentum measurement has certainly been considered by many experimental atomic physicists. One immediately recognizes, however, that the target atom at room temperature has already such a large initial momentum spread that typical momenta of the recoil ions gained in the collision are largely covered by the target thermal motion at room temperature (He at room temperature has about 4.6 a.u. mean momentum). This was the reason why the measurement of the momentum of the recoil ion was for a long time not seriously exploited as an alternative high-resolution spectroscopy technique in ion-atom collisions [38]. Using existing techniques for gas target cooling, however, the initial target momentum spread can be reduced

dramatically. As will be shown below, the target can be cooled to temperatures far below 1 K. With modern laser-cooling techniques, in particular successful for cooling of the alkali atoms, temperatures in the few μ K range, i.e. a few neV kinetic energy of the target atoms, are feasible. The use of such cold trapped atoms for ion momentum measurements is currently explored in several laboratories. Using supersonic gas target devices for He a few mK has already been obtained, which is equivalent to a He kinetic energy of below 1 μeV. In present COLTRIMS devices based on supersonic gas jet targets a momentum resolution of 0.05–0.2 a.u. for the recoil ion and a detection efficiency of about 60% of all ions from a reaction (4π solid angle but 60% detection efficiency) is routinely achieved.

Before high-resolution COLTRIMS was developed recoil ion momenta in atomic physics have been measured already in the sixties for slow or small impact parameter collisions, which lead to ion energies of 10^1–10^3 eV. The momenta of those ions, whose energies in the present context were extremely high, have been measured for example by Everhard and Kessel [39,40] and Federenko [41]. For fast charged-particle collisions and photoionization, the recoil ion energies are in the meV regime or even below. The charge state distribution of such slow ions has been measured in numerous experiments using a time-of-flight technique or magnetic deflection (see [42] for a review). First attempts on measuring angles and momenta of slow recoil ions were reported already in the seventies [43–48]. Ullrich and Schmidt-Böcking [37] succeeded 1987 in the first quantitative measurement of transverse recoil ion momenta in 340 MeV U^{32+} on Ne collisions [37,49,50]. They used a static room temperature gas target, time-of-flight measurement in a field-free drift tube and magnetic ion charge state selection. The technical development from this first recoil ion momentum spectrometer to todays most advanced momentum microscopes will be discussed in detail in Section 3. The momentum resolution of this gas cell spectrometer was considerably improved using a cooled gas cell (30 K) [51,52], and first Multiple-DCS have been measured by coincident detection of recoil ion and projectile transverse momenta [51–61]. Parallel to this development at University Frankfurt Germany, Cocke and coworkers at Kansas State University have used warm effusive gas-jet targets and an electric projection field [62,63]. They measured the first recoil ion longitudinal momentum distributions, deducing the Q-value of the collision. Since 1991 at the University Frankfurt (Germany) [64] and at CIRIL/GANIL (Caen, France) [65] recoil ion momentum spectrometers based on supersonic gas-jet targets have been developed. The extremely low internal temperature of such gas-jets (typically below 1 K) yielded a momentum resolution of 0.2 a.u. and below, more than a factor of 10 better than effusive or static target devices. An even colder gas target has been built using precooling of the target gas to 15 K [66,67]. The ionic momentum resolution in these devices was in most cases not limited by the internal target temperature but by the extension of the target in the ion momentum spectrometer. Spectrometers with electrostatic lenses today eliminate this problem by focussing in all three spatial dimensions and yield an ion-momentum resolution of 0.05 a.u. [31,68–70]. Presently at least in seven laboratories such COLTRIMS devices are in operation (Argonne, GANIL, GSI, Frankfurt, KSU, LBNL, RIKEN) and many more are in preparation.

The latest step in this rapid development was the combination of such COLTRIMS spectrometers with novel electron projection spectrometers. These electron imaging systems apply the basic principle of COLTRIMS to electron detection. For very low electron energies (typically < 5 eV) the same electric field which projects the positive ions onto one detector guides the negative electrons towards another detector [71–75]. Moshammer and coworkers have developed an

electron spectrometer which superimposes a solenoidal magnetic field parallel to the electrostatic field. This novel electron analyzer extends the projection technique for electrons towards much higher electron energies [76,77]. Such electron projection spectrometers achieve high resolution and 2π–4π solid angle even for zero energy electrons. A resolution of $\pm$ 5 meV at zero energy and full solid angle up to 300 eV has been reported [77]. In particular the detection of such very low-energy electrons is extremely difficult by conventional spectrometers. These projection spectrometers can be equipped with fast delayline detectors, capable of handling multiple hits [78]. Thus, all electrons from multi-electron reactions can be analyzed simultaneously [79]. Merging a high resolution recoil ion with such a multi-electron projection spectrometer creates an extremely versatile and powerful tool for atomic and molecular collision physics. Kinematically complete experiments for single ionization in slow, adiabatic collisions, for collisions of fast protons and antiprotons, for highly charged projectile impact, for relativistic collisions, for electron-impact and photon-induced double ionization by linearly and circularly polarized light have been performed already. In pioneering experiments for multiple ionization by fast ion impact, more than two electrons have been detected together with the recoil ion momentum [80].

This review paper is organized as follows: In Section 2 we present the kinematics of atomic reactions induced by heavy projectiles, electrons and photons from the perspective of the momentum transfer to the recoiling ion. The goal is to give guidance for the interpretation of recoil ion momentum spectra and to illustrate the large amount of information on the reaction which can be obtained from the momentum of the recoiling ion. This is followed (Section 3) by a review of the technical development from the first recoil ion spectrometers to the most advanced ion-electron momentum imaging systems, termed reaction microscopes. We complete this experimental section by a brief discussion of supersonic gas-jet targets and position sensitive detectors, the two most important ingredients of COLTRIMS. In Section 4 we give an overview on the experimental results obtained by this technique so far for charged particle impact and in Section 5 for photon impact. The overview covers most fields of atomic collision physics, including single capture and single ionization by ion impact, multiple-electron processes like double capture, transfer ionization and multiple ionization, electron impact ionization, photon-induced double ionization by linearly and circularly polarized light, Compton scattering and electron emission from aligned molecules. The energies of the projectiles range, for charged particles, from a hundred eV electrons to GeV/u bare uranium and, for photons, from threshold to 100 keV. This broad range of topics illustrates the fruitful and wide impact which the still young technique of COLTRIMS has already had. We conclude this review with an outline of some of the future perspectives of this technique and by at least naming some of the possible applications to other fields of physics.

2. Kinematics of recoil ion production

Independent of the dynamics of the ionization process, the observable momenta of collision fragments (recoiling ion, electrons and scattered projectile) are interrelated by the conservation laws of momentum and energy. The final state of a reaction with n fragments in the exit channel is described by $3n$ momentum components (neglecting the spin) plus internal excitation energies (Q-value). Due to momentum and energy conservation, however, only $3n - 3$ of these momenta are independent. Thus the reaction is kinematically fully determined by $(3n - 3)$ linearly independent

scalars or a $(3n-3)$-fold differential cross section. In the case of complete fragmentation (i.e. no internal excitation energy) the reaction kinematics is fully determined by $3n-4$ scalars. In this section we give a short outline of these kinematical relations from the perspective of the recoiling ion.

Throughout this paper we use atomic units (a.u.) with

$$m_e \equiv \hbar \equiv e \equiv 1 \quad \text{and} \quad c \equiv 137. \tag{1}$$

2.1. Ion–atom collisions

The typical momentum transfer in most ion–atom collisions is in the range of a few atomic units. This is only a small fraction of the initial momentum of the projectile in most collisions. For example in MeV p on He collisions the momentum exchange will be less than 10^{-4} of the initial projectile momentum. Thus observation of momentum transfer in ion–atom collisions by projectile detection (scattering angle and/or energy gain or loss measurements) is restricted in resolution by the fact that in the laboratory system a small change of a huge momentum must be resolved. Much higher resolution can be achieved by measuring quantities like electron or recoil ion momenta since these reaction products are initially nearly at rest in the laboratory frame. Because any momentum change of the projectile must be compensated by the sum momentum of the recoiling ion and all emitted electrons, the complete momentum balance of the reaction can be measured with much improved resolution by detecting recoil ion and electrons (i.e. by the so called inverse kinematics).

Utilizing relativistic mechanics, the change of the projectile longitudinal momentum $\Delta k_{\|\mathrm{pro}}$ for an ion atom collision in which n_r target electrons and n_p projectile electrons are emitted to the continuum and n_c target electrons are captured to projectile bound states, is given by

$$\Delta k_{||\mathrm{pro}} = \frac{Q}{v_{\mathrm{pro}}} - \frac{\sum_{j=1}^{n_r+n_p} E^j_{\mathrm{cont}}}{v_{\mathrm{pro}}} + \frac{n_c - n_p}{1+\gamma^{-1}} v_{\mathrm{pro}} \,. \tag{2}$$

Q is the difference of the sum of all atomic and ionic binding energies before and after the reaction, ($Q<0$ denotes endothermic reactions), E^j_{cont} is the kinetic energy of electron j which is emitted to the continuum measured in its parent atom rest frame, v_{pro} is the projectile velocity and the relativistic factor $\gamma = 1/\sqrt{1-v^2_{\mathrm{pro}}/c^2}$. A detailed derivation can be found in [68]. In the nonrelativistic case Eq. (2) is valid if the projectile energy change is small compared to the projectile kinetic energy. In the ultrarelativistic case, if the energy change is small compared to the relativistic total energy. Additionally Eq. (2) is only valid if the change of mass of the projectile is small compared to its relativistic initial mass. Both approximations are well fulfilled in practically all (distant) ion–atom collisions. From the three terms of the projectile momentum change in Eq. (2) the first and second one reflect the fact that all kinetic and potential energy delivered to electrons has to come from the projectile and thus leads to a projectile momentum loss. The third term reflects the projectile momentum change due to its change of mass by capturing or losing electrons.

For the recoiling ions the momenta in the transverse and longitudinal directions completely decouple within the approximation outlined above. For a polar projectile scattering angle $\vartheta_{\mathrm{pro}} \ll 1$ the recoiling ion momenta in the two directions perpendicular to the beam $k_{x,y\mathrm{rec}}$

are given by:

$$k_{x\mathrm{rec}} = -\left(m_{\mathrm{pro}} v_{\mathrm{pro}} \vartheta_{\mathrm{pro}} \cos \Phi_{\mathrm{pro}} + \sum_{j=1}^{n_r+n_p} k_x^j\right),$$

$$k_{y\mathrm{rec}} = -\left(m_{\mathrm{pro}} v_{\mathrm{pro}} \vartheta_{\mathrm{pro}} \sin \Phi_{\mathrm{pro}} + \sum_{j=1}^{n_r+n_p} k_y^j\right), \tag{3}$$

where Φ_{pro} is the azimuthal scattering angle of the projectile with mass m_{pro} and $k_{x,y}^j$ are the momentum components of electron j. For pure capture reactions where no electron is emitted to the continuum thus the recoil ion transverse momentum alone reflects the scattering angle of the projectile. This allows for extremely precise scattering angle measurements even for fast collisions where the typical projectile scattering angles are unmeasurably small.

The recoil ion momentum in the longitudinal direction ($k_{||\mathrm{rec}}$) can be calculated using energy and momentum conservation to be

$$k_{||\mathrm{rec}} = k_{||\mathrm{rec}}^{\mathrm{capture}} + k_{||\mathrm{rec}}^{\mathrm{ionization}} + k_{||\mathrm{rec}}^{\mathrm{loss}}\,, \tag{4}$$

$$k_{||\mathrm{rec}}^{\mathrm{capture}} = -\frac{n_c v_{\mathrm{pro}}}{1+\gamma^{-1}} - \frac{Q_c}{v_{\mathrm{pro}}}\,, \tag{5}$$

$$k_{||\mathrm{rec}}^{\mathrm{ionization}} = \sum_{k=1}^{n_r} \frac{E_{\mathrm{bind}}^k + E_{\mathrm{cont}}^k}{v_{\mathrm{pro}}} - k_{||e}^k\,, \tag{6}$$

$$k_{||\mathrm{rec}}^{\mathrm{loss}} = \sum_{l=1}^{n_p} \frac{E_{\mathrm{bind}}^l + \gamma^{-1} E_{\mathrm{cont}}^l}{v_{\mathrm{pro}}}\,. \tag{7}$$

The three terms of the sum originate from contributions of electron transfer to the projectile, ionization of the target and ionization of the projectile (loss). The initial state binding energies E_{bind} of electrons of the projectile or target are taken to be positive. The kinetic energies of the electrons lost from the projectile E_{cont}^l are measured in the projectile frame (not in the laboratory as all other quantities in the equation). Eqs. (4)–(7) are valid for relativistic and nonrelativistic collisions ($\gamma = 1$ for the latter) within the same approximation as above, that the energy and mass change of the projectile are both small compared to the initial energy and relativistic mass. As can be seen from Eq. (6) elastic collisions resulting in small scattering angles do not transfer longitudinal momentum to the recoiling ion. Furthermore the transverse and longitudinal momenta of recoil ion as well as of the projectile are fully decoupled. The recoil ion longitudinal momentum reflects the inelasticity of the reaction and the electron longitudinal momenta. We will briefly discuss the physical consequences of Eqs. (4)–(7) for capture (Section 2.1.1), target ionization (Section 2.1.2) and projectile energy loss (Section 2.1.3). A more detailed discussion is given in Section 4 along with the experimental results.

2.1.1. Kinematics of electron capture reactions

For electron-capture reactions ($k_{||\mathrm{rec}}^{\mathrm{ionization}} = k_{||\mathrm{rec}}^{\mathrm{loss}} = 0$) $k_{||\mathrm{rec}}$ has discrete values since the Q-value of the reaction is quantized. Thus measuring $k_{||\mathrm{rec}}$ is equivalent to traditional translational spectroscopy, with similar resolution at low projectile velocities but decisive advantages for fast

collisions or heavy projectiles. The Q-value for single capture reactions is related to the recoil ion final state longitudinal momentum by

$$Q = -\frac{v_{\mathrm{pro}}^2}{1+\gamma^{-1}} - v_{\mathrm{pro}} k_{||\mathrm{rec}} \,. \tag{8}$$

A recoil resolution of 0.05 a.u. results in a Q-value resolution of about 6 eV for a 10 MeV Ne projectile ($\Delta E/E < 10^{-6}$). This is already more than factor of 10 better than the best resolution obtainable by projectile energy gain spectroscopy. Even in the slow collision regime the resolution reachable by COLTRIMS for energy gain measurements is in many cases much superior to even the best energy gain measurements performed so far. For example, for 5 keV/u Ar projectiles one reaches a Q-value resolution of 0.6 eV or $\Delta E/E = 3 \times 10^{-6}$. In addition to the Q-value COLTRIMS studies yield automatically the transverse momentum distribution of the ion for each final state. The recoil ion transverse momentum for pure capture reactions mirrors the projectile scattering angle (see Eq. (3)). For slow collisions thus the impact parameter can be inferred. Examples of applications will be discussed in Section 4.1.1.

2.1.2. Kinematics of target ionization

For pure target ionization $k_{||\mathrm{rec}}$ can be obtained from the momenta of all electrons. For multiple ionization $k_{||\mathrm{rec}}$ reflects the sum energy and longitudinal momenta of all electrons, allowing for a detailed check of theories of multiple electron processes without detecting all electrons in coincidence. For fast collisions and slow electrons the first term in Eq. (6) is small and Eq. (6) simplifies to

$$k_{||\mathrm{rec}} = -\sum_{k=1}^{n_R} k_{||\mathrm{e}}^k \,. \tag{9}$$

The recoil ion longitudinal momentum just mirrors the sum longitudinal momenta of all emitted electrons. This has been demonstrated and widely used in experiments at GSI (Darmstadt) and CIRIL/GANIL (Caen) [32,76,77,81,82].

Two illustrations of Eqs. (9) and (6) are given in Figs. 1 and 2. For single ionization of He by 0.5 MeV protons ($v_{\mathrm{pro}} = 4.5$ a.u.) the term $E_{\mathrm{e}}/v_{\mathrm{pro}}$ is, for most events, a small contribution. The main contribution to the cross section found close to $k_{||\mathrm{rec}} = -k_{||\mathrm{e}} + E_{\mathrm{bind}}/v_{\mathrm{pro}}$ (Fig. 1). For smaller projectile velocities ($v_{\mathrm{pro}} = 0.77$ a.u. in Fig. 2) however, the term $E_{\mathrm{cont}}/v_{\mathrm{pro}}$ cannot be neglected. As a consequence of this a lower threshold for the recoil ion longitudinal momentum becomes visible. From Eq. (6) it follows that this lowest kinematically allowed value of $k_{||\mathrm{rec}}^{\mathrm{min}}$ for ionizing collisions corresponds to electrons travelling with the projectile in forward direction (electron capture to the continuum, ECC) [83] with

$$k_{||\mathrm{rec}}^{\mathrm{min}} = -\frac{v_{\mathrm{pro}}}{2} - \frac{E_{\mathrm{bind}}}{v_{\mathrm{pro}}} \,. \tag{10}$$

Such electrons are known to produce a singularity in zero degree electron spectra. In the distribution of $k_{||\mathrm{rec}}$ the ECC shows up as a step instead of a smooth onset of the cross section at $k_{||\mathrm{rec}}^{\mathrm{min}}$ [83,84].

Another prominent feature in electron spectra is the binary-encounter (BE) peak at an energy of $E_{\mathrm{BE}} = 2v_{\mathrm{pro}}^2 \cos\vartheta_{\mathrm{e}}^2$ for a polar emission angle of ϑ_{e}. Inserting this relation in Eq. (6) leads to

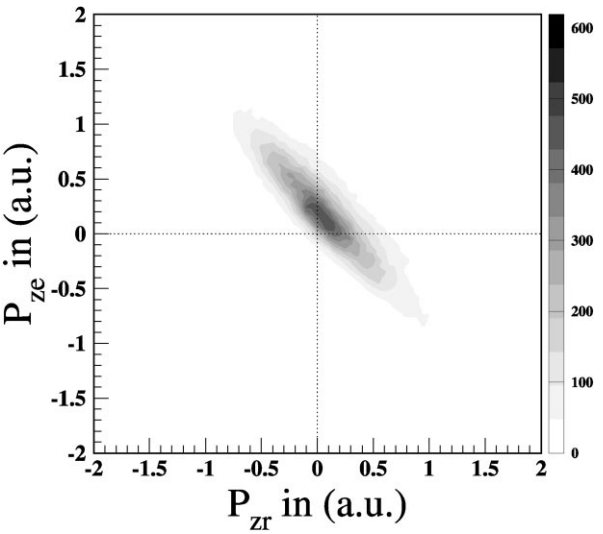

Fig. 1. Correspondence of He^{1+} $k_{\|e}$ and $k_{\|rec}$ for 500 keV proton impact single ionization of He. The distribution has been integrated over the transverse momenta of all particles. The distribution is shifted forward from the origin by a momentum of E_{bind}/v_{pro}, the E_{cont}/v_{pro} is small and yields some broadening of the diagonal (from [84]).

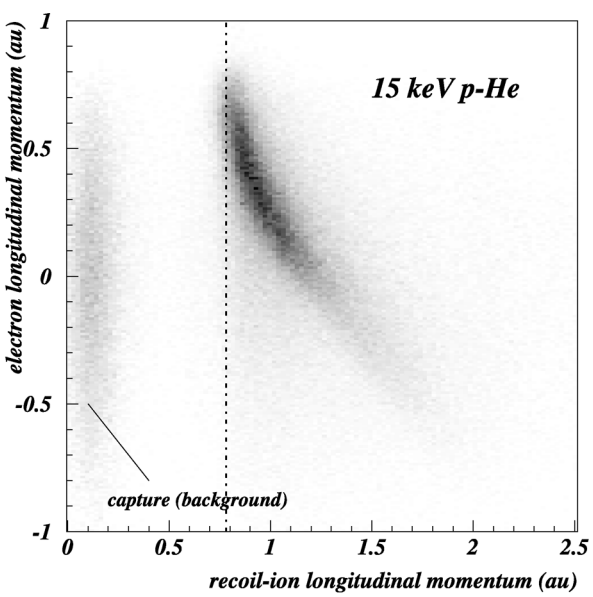

Fig. 2. Correspondence of $k_{\|e}$ and He^{1+} $k_{\|rec}$ for 15 keV proton impact single ionization of He. The distribution has been integrated over the transverse momenta of all particles. The threshold at $k_{\|rec}^{min} = 0.78$ a.u. (dashed dotted line) corresponding to electrons traveling with the velocity of the projectile ($v_{pro} = 0.77$ a.u.) is visible (from [90]).

$k^{BE}_{||rec} = E_{bind}/v_{pro}$. Thus, if one neglects this binding energy term, the recoil ion indeed remains a spectator in the production of BE electrons.

The relation between electron momentum vector and recoil ion longitudinal momentum (Eq. (6)) has been used by Tribedi and coworkers [85–87] to obtain recoil ion longitudinal momentum distributions by high resolution electron spectroscopy.

The features of capture and ionization can be seen in the longitudinal recoil ion momentum distribution for He^{1+} ions produced by 15 keV protons (Fig. 3). The discrete peaks correspond to Q-values for capture to excited states of the proton and to capture plus simultaneous excitation of the target. The Rydberg series of capture to bound projectile states converges from the left side towards $k^{min}_{\|rec}$ corresponding to capture to the continuum. It is followed by the continuous spectrum of ionization.

2.1.3. Kinematics of projectile ionization

For pure projectile ionization the momentum transfer to the target is, in the nonrelativistic limit, given by $(E_{bind} + E^{l}_{cont})/v_{pro}$ where the electron energy E^{l}_{cont} is measured in the projectile system.

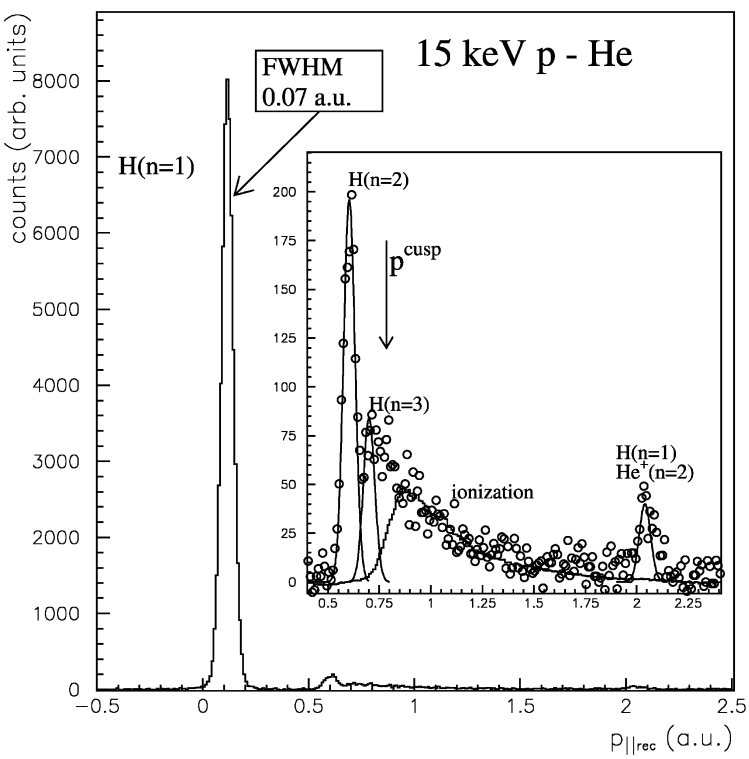

Fig. 3. Longitudinal momentum distribution of He^{+} ions from 15 keV proton impact. The dominant peak is due to capture to the projectile ground state. The arrow indicates the position of the capture to the projectile continuum ($k^{min}_{\|rec}$ of Eq. (10)). The distribution for ionization has been measured separately by detecting an electron in coincidence with the recoil ion. The momentum resolution is $\pm$ 0.035 a.u., equivalent to an energy gain resolution of $\pm$ 0.7 eV and a recoil ion energy resolution of $\pm$ 4.5 μeV (from [30]).

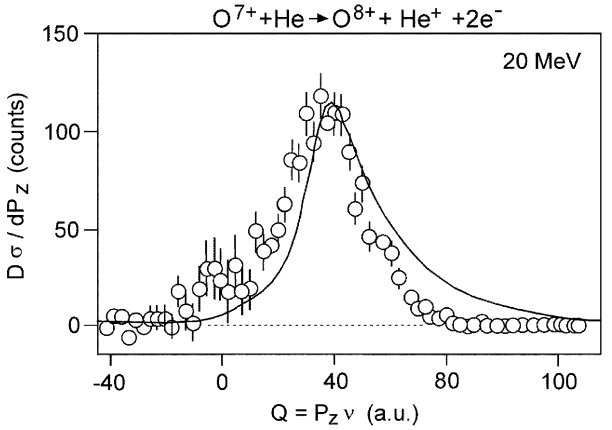

Fig. 4. Distribution of recoil ion longitudinal momenta for the reaction $O^{7+} + He \rightarrow O^{8+} + He^{1+} + 2e^{-}$(from [88]).

Thus, the recoil ion longitudinal momentum can be transformed directly in an energy spectrum of loss electrons. As for target ionization, the longitudinal recoil momentum distribution has a lower threshold. Fig. 4 reported by Wu and coworkers [88,89] shows strong forward emission of the recoil ion in an electron loss reaction. COLTRIMS requires the production of an ion, thus projectile ionization can only be investigated if it is accompanied by simultaneous target ionization. In this case the momentum transfer to the target can be shared between the recoiling ion and the target electron. Observing the recoil ion for such reactions gives a unique fingerprint to distinguish between projectile ionization by the electron–electron interaction and by the electron-nuclear interaction (see Section 4.2.3).

2.2. Electron–atom collisions

For electron-impact ionization in general none of the above approximations is valid. The energy loss of the projectile is in many cases not negligible and the projectile scattering is much more likely to lead to larger scattering angles. Both effects couple the longitudinal and transverse momenta of the recoil ion to projectile scattering and energy loss. The two components cannot be treated separately. Eqs. (4)–(7) hold only for fast collisions with small momentum transfer. In this case for example the binary peak, as it shows up in (*e*,2*e*) experiments, corresponds to the binary-encounter electrons from ion impact discussed in Section 2.1.2.

2.3. Photon–atom collisions

For photon impact we consider the two cases of photoabsorption (Section 2.3.1), and Compton scattering (Section 2.3.2). In both cases we restrict the discussion to nonrelativistic photo electrons.

2.3.1. Kinematics of photoabsorption

For absorption of a photon propagating in z direction leading to emission of a single electron and a recoiling ion momentum conservation yields

$$0 = k_{x,\mathrm{yrec}} + k_{x,\mathrm{ye}} \tag{11}$$

$$E_\gamma/c = k_{z\mathrm{rec}} + k_{z\mathrm{e}} \tag{12}$$

combining this with the conservation law of energy one obtains [91]

$$k_{x\mathrm{rec}}^2 + k_{y\mathrm{rec}}^2 + \left(k_{z\mathrm{rec}} - \frac{m_{\mathrm{rec}}}{m_{\mathrm{rec}} + m_{\mathrm{e}}}\frac{E_\gamma}{c}\right)^2 = 2\frac{m_{\mathrm{e}} m_{\mathrm{rec}}}{m_{\mathrm{e}} + m_{\mathrm{rec}}}(E_\gamma - E_{\mathrm{bind}}^{\mathrm{i}} + E_{\mathrm{bind}}^{\mathrm{f}}) - \frac{m_{\mathrm{e}} m_{\mathrm{rec}}}{(m_{\mathrm{e}} + m_{\mathrm{rec}})^2}\left(\frac{E_\gamma}{c}\right)^2. \tag{13}$$

If one neglects the (small) photon momentum E_γ/c, which is a good approximation in many cases, this equation describes a sphere in momentum space with radius

$$\sqrt{\frac{m_{\mathrm{e}} m_{\mathrm{rec}}}{m_{\mathrm{e}} + m_{\mathrm{rec}}}(E_\gamma - E_{\mathrm{bind}}^{\mathrm{i}} + E_{\mathrm{bind}}^{\mathrm{f}})}$$

($E_{\mathrm{bind}}^{\mathrm{i,f}}$ being the difference in total binding energies of the atom and ion in the initial and final state). In this approximation electron and recoil ion emerge antiparallel with the above momentum. Due to the mass of the ion, however, most of the energy is in the electronic motion, only a fraction of $m_{\mathrm{e}}/(m_{\mathrm{e}} + m_{\mathrm{rec}})$ is in the kinetic energy of the recoiling ion. For single ionization of 80 eV photons by He atoms Fig. 5 shows a two-dimensional slice through the momentum sphere of the ions [92]. The rings result from He^{1+} ions in different excited states (different $E_\gamma - E_{\mathrm{bind}}^{\mathrm{i}} + E_{\mathrm{bind}}^{\mathrm{f}}$). For a more detailed discussion see Section 5.1.

If one takes the photon momentum into account, two small corrections arise. First, both momentum spheres, of photo electron and ion, are slightly shifted into the forward direction by the photon momentum. Due to the electron/recoil ion mass ratio most of this photon momentum couples to the ionic motion. The ionic momentum sphere given by Eq. (13) is shifted by

$$\frac{m_{\mathrm{rec}}}{m_{\mathrm{rec}} + m_{\mathrm{e}}}\frac{E_\gamma}{c}$$

while the respective shift for the electron momentum is smaller by $m_{\mathrm{e}}/m_{\mathrm{rec}}$. The second correction is a shrinking of the momentum sphere of electrons and ions by the term

$$\left(\frac{m_{\mathrm{e}} m_{\mathrm{rec}}}{(m_{\mathrm{e}} + m_{\mathrm{rec}})^2}\frac{E_\gamma}{c}\right)^2.$$

This results from the tiny shift of the center of mass of the system by the photon. This correction is of the range of 10^{-18} of the momenta and, thus, irrelevant for all practical purposes.

For multiple ionization by photon impact one has to replace the electron momentum in the above equations by the sum momenta of all emitted electrons. Since these electrons can be emitted in all directions the ionic momentum for double ionization for example can range from $k_{\mathrm{rec}} = 0$ to a maximum of $k_{\mathrm{rec}} = 2\sqrt{E_{\mathrm{excess}}}$, where E_{excess} is the energy of the photon minus the electron

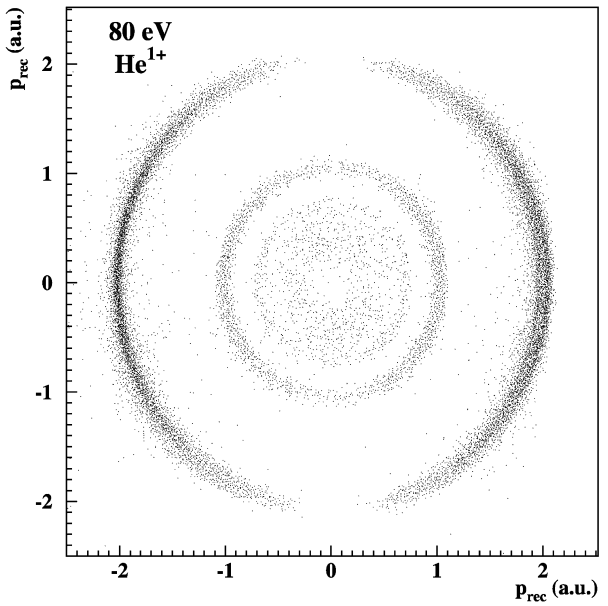

Fig. 5. (a) Momentum distribution of He^{1+} ions emitted after 80 eV photon impact. The x-axis is the direction of the polarization axis of the linear polarized light from an undulator (and at the same time the direction of the electric field of the spectrometer), the y-axis is the direction of the gas-jet, perpendicular to the propagation of the light and the polarization axis. The data represent a slice through a three-dimensional distribution and are integrated over a range of $\pm$ 0.1 a.u. in the third direction. The outer ring corresponds to ions in the ground state, the inner rings to excited states (from [90]).

binding energy. The zero value corresponds to equal energy electrons emerging back to back, the latter to two equal energy electrons emitted to the same direction. For the investigation of multiple photoionization processes, the recoil ion momentum measurement yields information on the correlated emission of the electrons. It mirrors the sum momentum of all emitted electrons.

2.3.2. Kinematics of compton scattering

Compton scattering can occur for unbound electrons. The momentum transfer takes place between the photon and the emitted electron. Momenta and energies are balanced between photon and electron. The recoil ion momentum reflects the initial momentum of the bound electron. Thus contrary to photoabsorption Compton scattering can be expected to create slow recoil ions. Spielberger and and coworkers have shown this difference between photoabsorption and Compton scattering experimentally [93] (see Section 5.5).

3. Experimental technique

Today's recoil ion momentum spectroscopy is the result of 15 yr of experimental development. Historically, the first recoil ion momentum spectrometers used extended gas targets and a field free drift path for the ions. We will first briefly review these devices (Section 3.1), which were used for

some of the pioneering experiments in recoil ion momentum spectroscopy. They allowed a measurement of the transverse recoil ion momentum with a solid angle of a few percent. The resolution was restricted by the thermal motion of the target and was 4.2 a.u. for He in the first spectrometer operating at room temperature and 1.2 a.u. in the next version operating at 30 K. Similar resolution, but for the first time 4π solid angle and information on the longitudinal momentum, was obtained by using an effusive gas target and projection fields (Section 3.2). The key to today's high-resolution COLTRIMS systems is a combination of a cold localized gas-jet target, large area position-sensitive detectors for low-energy ion and electron detection and arrangement of electric and in some cases magnetic fields to guide the ions and electrons from the target region to the detectors. We will therefore give a brief description of the supersonic gas-jet used (Section 3.3). This section naturally cannot review the very active field of research on and with supersonic gas-jets but only outline some of the basic properties of such jets which are of importance for their application in COLTRIMS. Different designs for spectrometers, i.e. for creation of the electric fields, are used at different laboratories. In Section 3.4 we will present these different concepts and will describe the way the momentum information can be obtained from the measured positions and time of flights. We will in particular discuss the range of accepted momenta and the momentum resolution achievable. The imaging concept for ions has been adopted for electron momentum space imaging as well. We briefly discuss the concept of such novel electron imaging devices in Section 3.5.

Large area position-sensitive detectors have to be used for COLTRIMS. Since the ions and electrons have much too low energies to produce a signal in any kind of detector material or to penetrate even a very thin detector window or dead layer, efficient and position sensitive secondary electron multipliers have to be used. Again we have to refer the reader to special literature on this subject, e.g. [94–96] for comprehensive information and only give a brief description of the micro-channel-plate detectors with wedge-and-strip read out and with delay-line read out which have mostly been applied in the work reviewed here.

3.1. Extended gas-target devices

The goal of the first recoil ion momentum spectroscopy (RIMS) experiments was to measure multiple ionization and capture cross-sections for fast (1.4–5.6 MeV/u) heavy-ion-atom collisions differential in projectile scattering angle [37]. Since the projectile scattering in those collisions leads only to a deflection of the projectile of a few μm over 10 m it cannot be measured directly. Thus, the first RIMS experiments intended to measure the transverse momentum transfer to the projectile by measuring the transverse momentum of the recoil ion. An extended cylindrical static gas target of 4 cm cylinder length and 1 cm diameter was used. The beam passed along the axis of the cylinder designed as a Faraday cage 'free' of electric fields. The ions, created along the beam path, drifted towards the wall of the cylinder in a time Δt inverse proportional to their transverse momentum. The ions left the cylinder through a small aperture, which was a 1 mm hole in a first setup and a slit of 20×1 mm in a second version of the spectrometer. They were accelerated over 500 V, pass a focussing einzellens and were charge state analyzed by a magnet before they hit a position-sensitive channel-plate detector. The drift region was shielded from the acceleration field by a woven mesh (similar to the spectrometer shown in Fig. 6). The transverse momentum was obtained from the time of flight measured in coincidence with the projectile and the recoil ion

charge state is obtained from the position on the channel-plate detector. In the first spectrometer of this type the gas cell was at room temperature. The momentum distribution from thermal motion of the target gas before the collision restricted the transverse momentum resolution to 4.2 (8.3) a.u. for He (Ne) targets. Typical recoil ion time of flights in such field free spectrometers were up to 20 μs [37]. A detailed description of this spectrometer can be found in [97]. To compare the experimental result to theoretical predictions in most cases the theory was folded with the thermal momentum distribution. The pioneering experiment yielding the transverse momentum distribution in fast U–Ne collisions are described in Section 4.2.6. A significant improvement in resolution was achieved by precooling the target gas and operating the gas cell on a temperature of 30 K [51–61]. A sketch of this spectrometer is shown in Fig. 6. The cooling reduced the influence of thermal motion to 1.2 a.u. for He gas, which corresponds to a recoil ion energy of 2.5 meV. On this level great care has to be taken to avoid any contact potential inside the field free drift region. The cylinder was gold plated and a woven copper mesh of 0.12 mm by 0.12 mm spacing covered the inside walls and shielded the acceleration field from the drift region. Before each experiment the apparatus was carefully cleaned in a supersonic bath. From the reproducibility of the results the absolute accuracy of the recoil ion energy measurements was estimated to be $\pm$ 5 meV. A more detailed discussion of this spectrometer can be found in [98]. The apparatus was used mainly for coincident measurement of recoil ion transverse momenta with the projectile polar and azimuthal scattering angle (see Section 4 [51–61]).

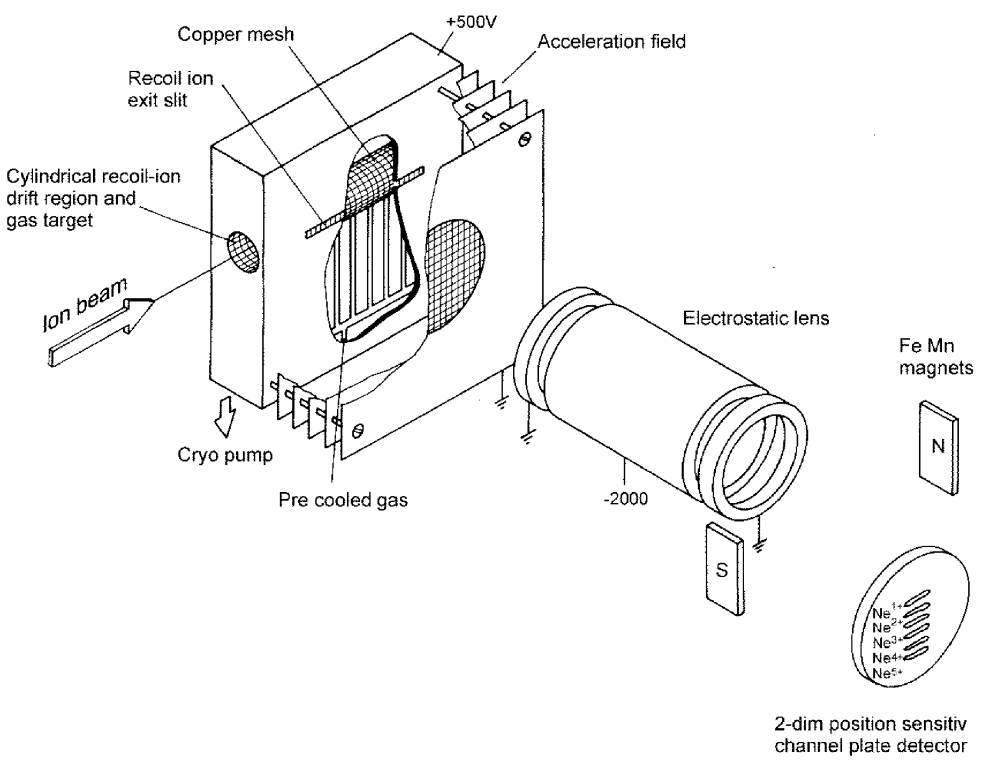

Fig. 6. Recoil ion spectrometer with cooled static gas cell. The spectrometer is mounted on a cryogenic cold head (from [53]).

3.2. Effusive gas targets

Frohne et al. [62] and Ali et al. [63] measured recoil ion momenta using an effusive gas jet target. The directed gas flow was achieved by a multi-capillary array. The collimated projectile beam passed only few mm above this gas outlet. The ions created in this region were extracted by an electric field onto a position-sensitive channel-plate detector. The gas-jet was directed onto this detector. The momentum resolution achieved with this technique for a Ne target was about 6 a.u. in the direction transverse to the jet and 8–10 a.u. in the longitudinal direction [99,63], comparable to what was achieved with the cooled gas cell for Ne [60,61]. The collimation of the gas flow in the channels of the capillary array lead to this effective cooling. With this device for the first time a measurement of the longitudinal recoil ion momentum could be performed. In addition these devices were the first to yield a 4π solid angle for all ions. The recoil ion charge state was determined from the mean time of flight in the spectrometer, the momentum from the position on the channel plate and the deviation of the time of flight from the center of the TOF distribution for a given charge to mass ratio. This will be described in more detail in the next section. Wu and coworkers reported on a much improved longitudinal momentum resolution achieved by collimating the effusive jet with a skimmer leading to a resolution of 1.5 a.u. [100].

3.3. Supersonic gas-jet targets

A decisive step forward in resolution for recoil ion momentum measurement became possible with the use of supersonic gas-jet targets. Such jets provide a dense (local target pressures of more than 10^{-4} mbar can be achieved with standard pumps), well localized and internally cold gas target which makes them ideally suited for recoil ion momentum measurements. They are used in many fields of physics, for example for providing mono energetic projectiles for atom–atom scattering experiments. A detailed description of free jet sources can be found in [101]. Fig. 7 shows for comparison the momentum distribution of ions from room temperature gas and ions from a supersonic gas jet.

If the gas expands through a nozzle and the ratio of pressures on the two sides is larger than typically 2 [101] the flow reaches supersonic speed. In the ideal case of an adiabatic isochore expansion of an ideal gas, the internal energy ($\frac{3}{2}kT_0$, with the Boltzmann constant k and the gas temperature T_0 before the expansion) and the compressional energy are converted to kinetic energy of the gas atoms. For mono-atomic gases the compressional energy is kT_0. Thus under ideal conditions the directed motion of the atoms after supersonic expansion tends towards an asymptotic momentum of

$$k_{\mathrm{jet}} = \sqrt{5mkT_0} \tag{14}$$

with the mass m of the target gas. For He at room temperature we have $k_{\mathrm{jet}} = 5.8$ a.u. The width of the velocity distribution around this mean velocity is described by the speed ratio S of the expansion. With the internal temperature T of the jet the speed ratio for an ideal mono atomic gas is defined as

$$S = \sqrt{\frac{5}{2}\frac{T_0}{T}}\ . \tag{15}$$

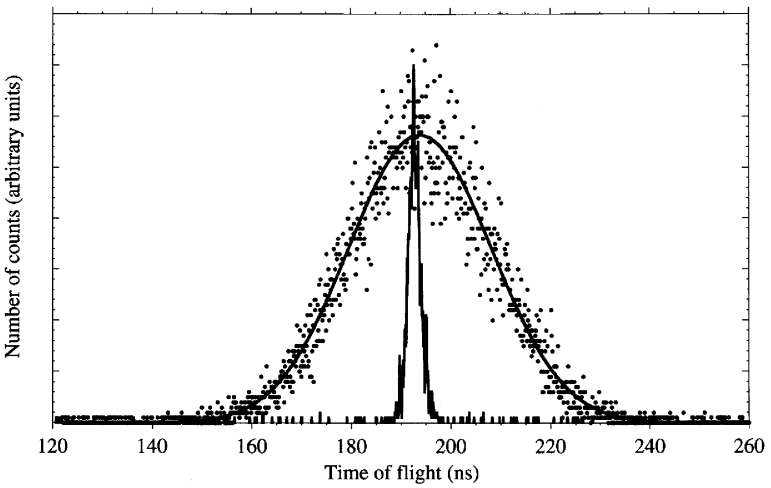

Fig. 7. Time-of-flight distribution of recoil ions from room temperature gas (dots) compared to ions from a supersonic gas jet (histogram). The deviation of the TOF from the mean value is proportional to the momentum of the ions in the direction of the electric field. The full line shows the thermal momentum distribution (from [65]).

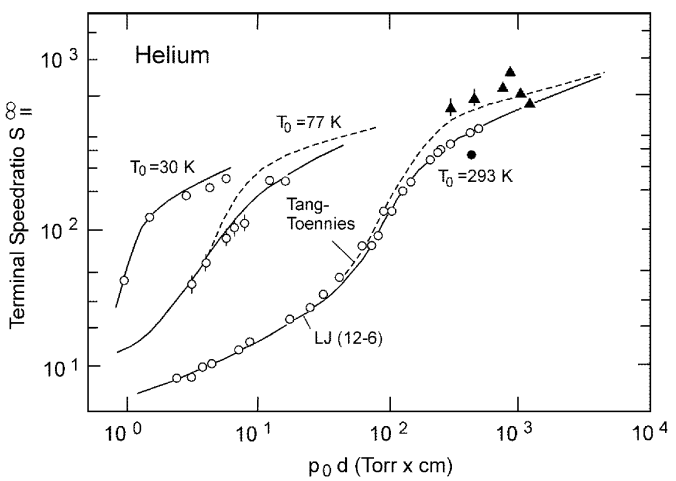

Fig. 8. Speed ratio of a He gas-jet for different temperatures (T_0) of the nozzle (from [103]).

The speed ratio of an expansion depends on the intra jet scattering cross-sections and, thus, the gas species, the gas temperature and on the product of driving pressure p_0 and nozzle diameter d. The speed ratio for He at various temperatures is shown in Fig. 8 as a function of $p_0 d$ (see also [102]).

The region in front of the nozzle where the expansion is still supersonic is called the zone of silence. A typical value for the spatial extension x_s of this region beyond the aperture is

given by [101]

$$x_s = \frac{2}{3}\sqrt{\frac{p_0}{p_s}}d \tag{16}$$

with p_s being the pressure downstream of the nozzle. To achieve a real supersonic gas beam a skimmer must be placed inside the zone of silence. The transmitted gas beam follows an unperturbed motion in the high vacuum environment of the scattering chamber.

The gas flow through the nozzle a nd thus the load to the pump is proportional to $p_0 d^2\sqrt{T_0}$. For the practical application in COLTRIMS one aims to achieve high density, narrow collimation (typically 1–2 mm at the intersection with the beam, in a distance of 3–5 cm from the nozzle) and narrow internal momentum distribution in jet direction as well as perpendicular to the jet. The width of the momentum distribution in the jet direction is the product of the jet velocity and the inverse speed ratio, both of which improve with cooling the gas. Perpendicular to the jet the momentum distribution is determined by the jet velocity, skimmer diameter and skimmer–nozzle distance.

As examples we list three versions of gas jets which have been successfully used in COLTRIMS setups. All are operating with a nozzle diameter of 0.03 mm. Smaller nozzles would improve the speed ratio for a given pumping speed, but are less practical since they tend to get clogged by dust particles. Jagutzki and coworkers [64,93,104,105] used a single stage gas jet with a 8000 l/s oil-diffusion pump backed by a 500 m^3/h roots pump and a 120 m^3/h roughing pump. Due to the large pumping speed this jet can be operated at room temperature still having a good speed ratio and high target density (local target pressure at the beam intersection is several 10^{-4} mbar). Mergel and coworkers used a cryogenic cold head to cool the nozzle to 14 K. This allowed to operate the single stage jet with only one 360 l/s turbomolecular pump. The trade-off for the small pumping speed is a much lower target density (several 10^{-5} mbar). With the cooling, however, the internal temperature improves in all three dimensions. In particular useful for ion–atom collisions is the low momentum spread in the direction perpendicular to the jet. With the same geometry the cooling improves also the resolution in this direction due to the lower jet velocity. A further advantage of a smaller velocity is a reduced gas load for the same target density. This is of particular interest for the implementation of such jets in the ultra-high vacuum of a storage ring as it is in preparation for the CRYRING (Stockholm) [106]. A third concept of a two-stage jet has been used by Moshammer and coworkers [77] and others. The region between the nozzle and the first skimmer is in this system pumped by a 250 m^3/h roots pump. It can operate at higher pressures than most turbopumps and thus take a higher gas load at a smaller pumping speed. The driving pressure is comparable to the one-stage device with a large diffusion pump but it is much smaller in size. For this setup a second stage with a skimmer (typical skimmer–skimmer distance: 2 cm), pumped by a turbopump is required for two reasons. First the high background pressure of only 10^{-1} mbar leads to a diffusion of warm background He gas through the first skimmer. Second the pressure condition achieved with the roots pump leads to a small zone of silence (see Eq. (16)) and thus requires a small nozzle–skimmer distance of typically 2–4 mm resulting in a large divergence of the jet. A two stage jet can additionally by cooled to further improve the jet quality but some thermal shielding is necessary in the first stage.

In all the setups discussed the gas jet leaves the scattering chamber through an opening of typical 1 cm into a jet dump, pumped by a separate turbo pump. For UHV applications more than one

stage of jet dump pumping is necessary to reduce back streaming of gas from the jet dump to the chamber [106].

The internal momentum distribution and, thus, the resolution obtainable is different in the three spatial directions. In the direction of the jet it is defined by the ratio of mean jet velocity and speed ratio. Typical momentum resolution values in jet direction range in 0.01–0.07 a.u. [102]. In the direction of the projectile beam the resolution is to first approximation given by the collimation geometry of the skimmer system and can thus be varied (this also changes the target density). However, as outlined in [101] there is a small non-Gaussian tail extending to large transverse momenta. A typical value for the resolution achieved perpendicular to the jet in beam direction for a cooled jet is 0.05 a.u. In the third direction perpendicular to the jet and the projectile beam the latter is often narrower than the jet which improves the resolution. This can be an important further improvement of resolution for well collimated ion beams (0.1 mm) or well focussed light from third generation synchrotron radiation sources where a focus of below 0.05 mm can be achieved. For a 30 K cooled jet a 0.05 mm focus would correspond to a resolution of 0.002 a.u. or an ion energy of 0.006 μeV.

3.4. Projection spectrometers for slow ions

All COLTRIMS spectrometers used with supersonic gas-jet targets apply a projection technique. An electric field guides the ions from the small overlap volume of the gas jet with the projectile beam (i.e. ion, electron or photon beam) onto a position-sensitive detector. From the position of impact on the detector and the ion time of flight the starting momentum can be calculated.

The various spectrometers used so far differ in the details of the field geometry and field direction. An example for the simplest configuration is shown in Fig. 9. The ions are accelerated over 3 cm by a weak homogeneous static electric field (typically 0.3–10 V/cm). They pass a woven mesh (typical wire spacing of 0.25 mm) and enter a field free drift region of 6 cm length. After passing a second grid (typically 0.1 mm wires spacing) they are postaccelerated over 2000–3000 V onto a channel-plate detector. The exact ratio of 1 to 2 between the length of acceleration and drift region assures that ions starting at slightly different positions (i.e. potentials) along the electric field lines arrive at the same time at the detector [107]. Such McLaren focussing geometry is indispensable since one wants to resolve recoil ion energy differences of far below 1 meV, where the typical width of the target of 1 mm would already corresponds to 30 mV difference in the starting potential. In the McLaren geometry different starting momenta in direction of the field result in different time of flights. Varying starting momenta in the two directions perpendicular to the electric field yields different displacement on the channel-plate detector. Care has to be taken to assure proper field conditions in the spectrometer area.

In the spectrometer shown in Fig. 9 the extraction region is shielded from external potentials by a carbon fiber (not visible on the figure). One fiber of 7 μm diameter and 10 m length is wound in a spiral with 1 mm spacing around the four supporting germanium coated insulator screws. The fiber defines a very well controlled field in the extraction region [108,67,66]. All grids and the inside of the drift tube are germanium coated. Instead of the carbon fiber in other setups wires or rings of thin sheet metal, which are connected by resistors, have been used successfully [64,89,109,110]. Fig. 10 shows a typical time-of-flight spectrum obtained with such a spectrometer. The width of the

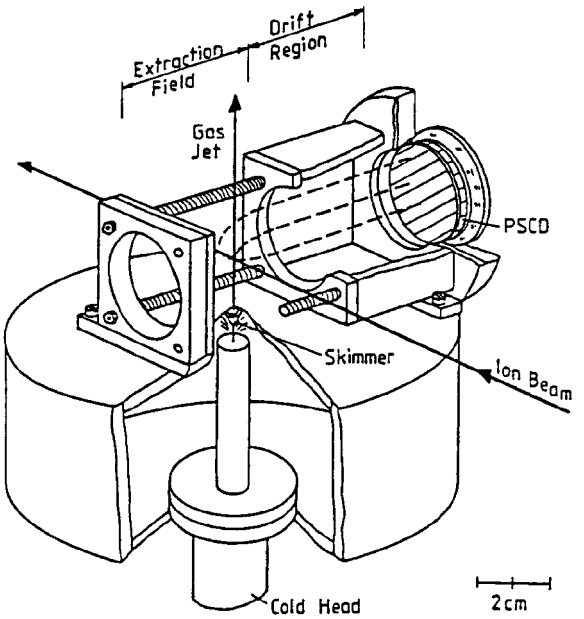

Fig. 9. COLTRIMSpectrometer. The nozzle is cooled to 14 K. Carbon fibers (not visible in the figure) are wound around the four rods to create a homogeneous extraction field (from [108]).

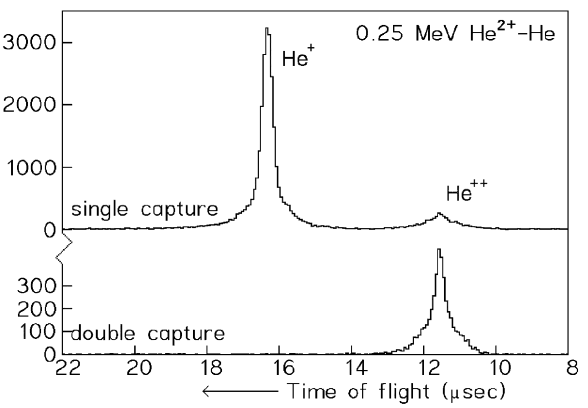

Fig. 10. Time-of-flight distribution of He ions from 250 keV/u He^{2+} on He collisions, coincident with charge exchanged ejectiles. The width of the peaks reflects the starting momentum of the ions (from [111]).

time peaks reflects the different starting momenta in field direction. The position distribution of counts on the channel-plate detector is shown in Fig. 11. The narrow peak results from ions created in the overlap of jet and ion beam. The small ridge in front of the peak results from residual gas ions which are created along the ion beam. The width of this band reflects mainly the thermal momentum distribution of the residual gas before the ionization. It is displaced from the peak ions due to the directed velocity of the jet.

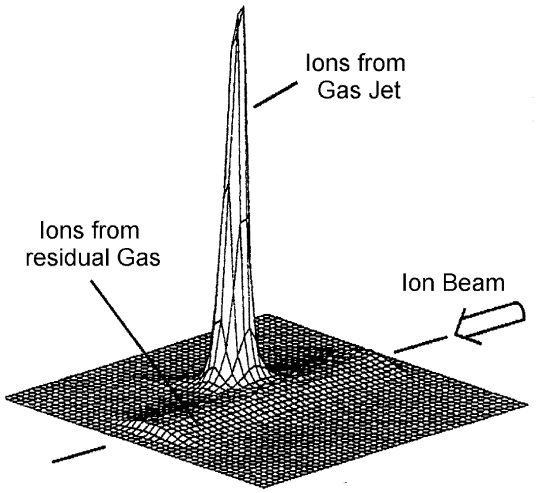

Fig. 11. Image of He ions created by ionization by a fast heavy ion beam. The electric field is perpendicular to the ion beam and the surface of the detector. The small ridge results from warm residual gas ionized along the beam, the peak results from the interaction with the gas jet (from [77]).

To obtain the recoil ion momentum in field direction $k_{x\mathrm{rec}}$ from the time of flight (t) it turns out that it is for all practical purposes sufficiently accurate to account only for the linear term:

$$k_{x\mathrm{rec}} = \frac{Uq}{s}(t_0 - t) \,, \tag{17}$$

where q is the ionic charge, U/s is the field in the spectrometer and t_0 is the time of flight of ions starting with momentum $k_{x\mathrm{rec}} = 0$. Physically, this approximation assumes that the time focussing is ideal, i.e. that the time of flight of zero momentum ions is exactly independent of the starting position in the field. With an extraction region of 3 cm and a field of 0.33 V/cm Eq. (17) is at a momentum of 10 a.u. accurate within 1.6%.

For the two directions perpendicular to the extraction field there is no force acting on the ions, thus the y and z momenta are simply given by

$$k_{y\mathrm{rec}} = \frac{\Delta y}{t} m_{\mathrm{rec}} \,,$$

$$k_{z\mathrm{rec}} = \frac{\Delta z}{t} m_{\mathrm{rec}} \,, \tag{18}$$

where $\Delta y, z$ is the displacement of the recoil ion from the position where an ion with zero momentum transfer would hit. The jet velocity results in a displacement of the zero point. In practice the zero point in the direction of the jet is simply given by the center of the peak, since the momentum distribution is rotationally symmetric around the ion beam. In the direction of the ion beam (longitudinal momentum) there is no intrinsic symmetry of the ionization process providing the zero point. In principal this zero could be found by varying the extraction field. This is,

however, in most cases not accurate enough. Thus, one can either use reference data or calibrate the spectrometer with capture reactions which result in lines of known longitudinal momenta. Electron impact is well suited for a reference measurement, since an electron gun can be easily implemented in a collision chamber and fast (e.g. 5 keV) electrons yield a maximum in the recoil ion distribution very close to zero [105,64]. For such a calibration measurement no coincidence is necessary, since the time of flight is not needed. One can simply use the position distribution and a mean time of flight estimated from the voltages at the spectrometer. An example for a calibration of a spectrometer using different capture reactions can be found in [112].

In spectrometers which exploit homogeneous electric fields only, the momentum resolution in the two dimensions perpendicular to the electric field is determined by the extension of the interaction volume and the ion time of flight. For a typical time of flight of 15 μs for He^{1+} ions a diameter of the gas jet of 1 mm results in a momentum resolution of 0.2 a.u.. Mergel and coworkers have reported a resolution of 0.26 a.u. FWHM in the direction of the projectile beam obtained with the spectrometer shown in Fig. 1 of [108]. To circumvent these restrictions of the extended reaction volume, electrostatic focussing lenses in the extraction field can be used. If the detector is placed in the focal point, ions created at slightly different positions but with the same momentum vector hit the detector at the same position. The field geometry of one the first three-dimensional focussing spectrometer designed by Mergel following a suggestion by Cocke [68] is shown in Fig. 12. With this field geometry the displacement on the detector is still proportional to the starting momentum. The implementation of a lens in the extraction field changes, however, the focussing properties in the third, the time-of-flight direction. Thus, lens and length of the drift tube have to be adjusted such, that the focus length for the time of flight and the spacial focussing by the lens coincide. In general the implementation of a lens requires a longer drift tube compared to a spectrometer with homogeneous fields. The spectrometer shown in Fig. 12 focuses an extended target region of 5 mm to a focus spot of below 0.25 mm on the detector. With such focussing spectrometers finally the grid which shields the field free drift region from the high postacceleration field (typically 1 kV/mm) in front of the ion detector becomes crucial. The individual pores of the mesh act as strong lenses restricting the achievable position resolution for such low-energy ions to the mesh width. A stack of several meshes produces significant Moire patterns; therefore the use of one narrow grid (typically 100 μm mesh width) is preferable to a stack of wider meshes [70]. The use of electrostatic lenses for imaging of photoelectrons and photofragment ions has recently been reported by Eppkin and Parker [113] who investigated photodissociation of molecular oxygen.

Instead of perpendicular to the gas jet and to the projectile beam the ions can alternatively be extracted almost parallel to the beam. This extraction geometry has been widely used by the group at GSI [77] (Fig. 13). In the extremely flexible spectrometer developed there the extraction field is

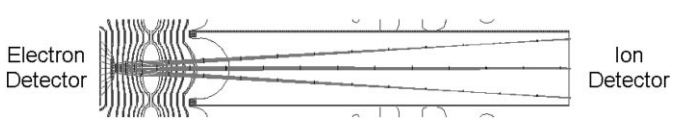

Fig. 12. Field geometry with three-dimensional focussing properties. The three groups of trajectories result from ions starting with different momenta in the direction perpendicular to the field (from [68,70]). In such focussing spectrometers the momentum resolution becomes independent of the size of the target.

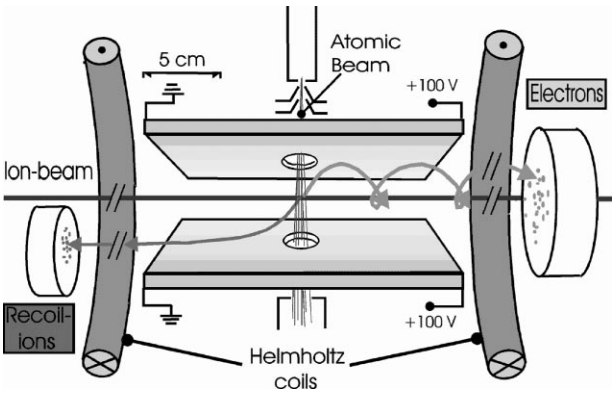

Fig. 13. Combined recoil ion electron spectrometer with extraction (almost) parallel to the beam. The electric field is generated by resistive plates. A solenoidal magnetic field is superimposed to the electric field to guide the electrons to the electron detector (from [77]).

generated by two ceramic plates with resistive layers. By adjusting the potentials at the four corners of each plate the ions can be easily steered to any direction. Thus, the extraction can be switched from parallel to perpendicular to the beam without breaking the vacuum. As a further advantage of this configuration the offset velocity of the ions from the gas jet can easily be compensated by steering the ions back to the center of the channel-plate detector.

Whether perpendicular or parallel extraction of the ions is preferable strongly depends on the physical process to be investigated. In many cases it is advantageous to have extraction parallel to a symmetry axis of the physical process (like the polarization axis for photoionization studies or the beam axis for ion impact).

3.5. Projection spectrometers for electrons

Electrons can be detected by a projection technique analogous to the one discussed for ions. The method has first been applied to image photoelectrons formed in intense laser fields [114]. In a COLTRIMS setup the same electric field which guides the positively charged ions to one direction accelerates the electrons in the opposite one. The mass difference between ions and electrons has, however, some severe consequences for projection techniques. The first difference is given by the physics of the ionization process; in many ionizing atomic reactions the fragments (e.g. ions and electrons) have momenta of the same order of magnitude. Thus, typical electron energies are of the order of m_e/m_{rec} times the recoil ion energies. While the ion energies are mostly small compared to the energy the ions gain in the electric field of the spectrometer this approximation is not valid for most of the electrons. Therefore 4π collection efficiency is harder to achieve for electrons than for ions. The second important difference in ion and electron imaging is that for the motion in a homogeneous electric field for low-energetic particles the total time-of-flight scales with $\sqrt{m}$ while the measured displacement on the detector for a given momentum scales linearly with the mass. As a consequence spectrometers which use homogenous electrostatic fields are much shorter on the electron side than on the recoil side, to achieve large electron detection solid angle.

Such combined electron-ion-projection spectrometers based on electric fields only have been used with great success in photoionization studies close to threshold [70,115–117] and for imaging of electron emission in slow ion atom collisions [31,71–75] and fast proton and antiproton–helium collisions [84,118,119].

To extend this 4π electron imaging to higher electron energies a novel spectrometer type has been developed and extensively applied at GSI (see Fig. 13). In this extremely versatile spectrometer a solenoidal magnetic field is superimposed parallel to the electric field. The electrons travel on spiral trajectories from the reaction volume to the detector. From the two position informations and the measured time of flight, this trajectory, and the three initial momentum components, can be reconstructed, in most cases uniquely. For illustration Fig. 14 shows the radius on the channel plate versus the measured time of flight. If the electron time of flight is an integer multiple of the inverse of the cyclotron frequency in the two dimensions perpendicular to the magnetic field all electrons (independent of the momentum in this plane) return to their starting point which leads to the nodes visible in Fig. 14. Therefore in these nodes the information on the momenta perpendicular to the field is lost. The resolution is best in the center between the nodes. The existence of these nodes, however, gives a very good control of the experimental conditions. For example the cyclotron frequency and thus the magnetic field is measured very precisely via these nodes. Thus, the magnetic field is known very well. Details on this spectrometer can be found in [77,120]. The main advantage of this solenoidal magnetic field spectrometer is the quasi decoupling of the motion perpendicular and parallel to the fields. Therefore the electric field can be optimized for good resolution in the time-of-flight direction for electrons and ions. The electron detector can be placed at any distance from the interaction zone to achieve good resolution even for higher energetic electrons which have short time of flights. The magnetic field can be adjusted independently to confine electrons up to a certain momentum perpendicular to the field. Typical operating conditions are for example a magnetic field of 15 G. This field results in a revolution time of 24 ns. With an active detector area of 8 cm diameter the spectrometer yields 4π solid angle for electrons up to

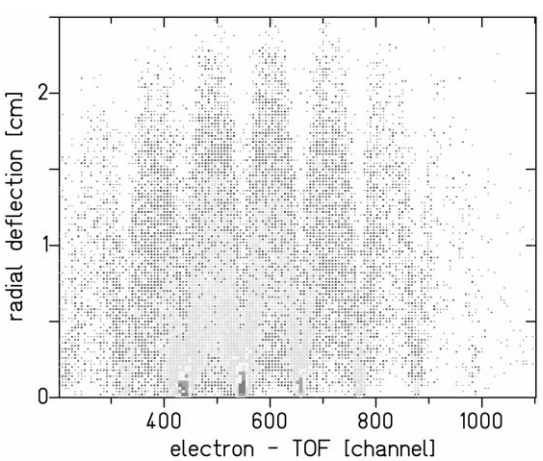

Fig. 14. Radial deflection of electrons on the electron detector in the spectrometer shown in Fig. 13 versus electron time of flight, for 3.6 MeV/u Ni^{24+} impact on He. The frequency of the nodes is given by the cyclotron frequency of the magnetic field (from [77]).

an energy of about 100 eV. Since the recoil ions are accelerated to a very high momentum by the electric field the magnetic field has only a small influence on their trajectories. In most cases it is sufficient to account for this in a global way by rotating the position distribution of the ions on their detector by a few degrees.

The GSI spectrometer has been used for kinematically complete measurements of the single and multiple ionization process in fast highly charged ion atom collisions [76,121,122] and (e,3e) studies [17]. A similar setup has been used for investigation of photo double ionization of He [123]. The full solid angle makes such electron spectrometers especially well suited for coincident detection of many electrons from multiple ionization processes. They can be equipped with a multi-hit capable detector and there is no restriction on the number of electrons which can be detected from one single event. Moshammer et al. succeeded in the first kinematically complete study of double ionization by fast ion impact [79,81] using the spectrometer shown in Fig. 13 and detecting both electrons. An alternative approach using non-homogeneous electrostatic fields instead of the magnetic field has recently been proposed by Mergel and coworkers [124] for imaging of electrons emitted from surfaces.

3.6. Position-sensitive detectors

For recoil ion and electron momentum imaging large-area position-sensitive detectors which combine good position resolution (typically 0.1 mm) with good time resolution (below 1 ns) are essential. Channel-plate detectors with wedge-and-strip or with delay line position encoding have been most widely used for this purpose. For a more complete overview on such detectors see [124,78], for wedge and strip readout see [125]. Channel-plate detectors have a typical detection efficiency for charged particles of about 60% given by the open area. For imaging purposes chevron (two plates) or z-stack (3 plates) configurations of 48 mm or 86 mm diameter are used. The ions are typically accelerated by 2000 V onto the surface of the channel plate. For electrons, maximum efficiency is reached at about 200–300 eV. A typical pulse height distribution from a channel-plate z-stack and the detection efficiency of He^{1+} ions as function of the acceleration voltage is shown in Figs. 15 and 16.

A detector with wedge-and-strip read out is shown in Fig. 17. The electron cloud of about 10^5–10^6 electrons created by avalanche amplification in the channels are accelerated onto a high-resistivity Ge layer evaporated on a 1.5 mm ceramic plate (see [126]). The image charge is picked up on the backside of the ceramic plate by the three areas of the wedge-and-strip structure. The area of the wedges and stripes grows linearly with the x and y position, respectively. A proper adjustment of the resistivity and the thickness of the ceramic plate assures that the image charge covers more than one structure. This is essential to allow for a determination of the centroid of the charge cloud. The typical period of the structure is 1.4 mm. The charge signals of the wedge, strip and meander structures are amplified by charge-sensitive preamplifiers and main amplifiers and recorded by analog to digital converters. By normalizing the wedge and the strip signal to the total pulse height one obtains the position of the centroid of the charge cloud. For a 5 cm diameter anode a position resolution of 0.05 mm can be achieved. The position resolution is mainly determined by the signal to noise ratio of the three signals. Therefore a good pulse-height resolution and high gain is desirable. The timing information is picked up either from the front or the back side of the channel-plate stack. Time resolution of 400 ps has been obtained this way [123].

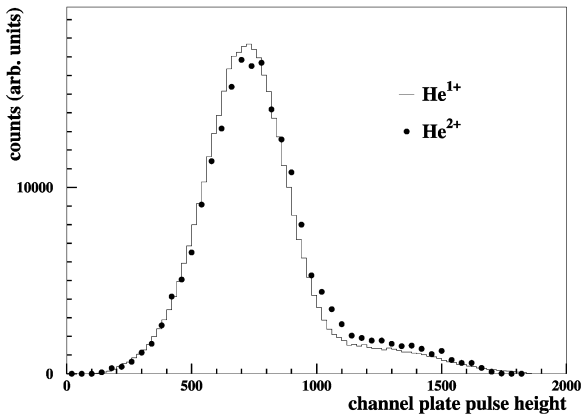

Fig. 15. Pulse height distribution for He^{1+} and He^{2+} ions on a z-stack channel-plate detector (i.e. three plates). The ions hit the detector with an energy of $3000\,eV \times q$ (from [92]).

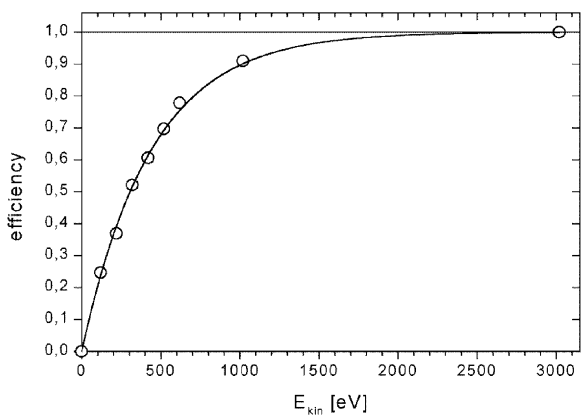

Fig. 16. Relative detection efficiency of a z-stack of channel plates for He^{1+} ions as a function of the acceleration voltage to the surface. At 3000 eV the curve is arbitrarily normalized to 1 (from [68]).

A delayline position read out for channel-plate detectors has been suggested by Sobottka [127]. For one dimension a pair of wires is wound around a supporting structure. The spacing between the wires is 0.5 mm. By a potential difference of 50 V between the two wires the electrons are collected by only one of the wires (see Fig. 18). The wire pair acts as a Lecher cable. At both ends of the double wire spiral the signals are processed by a differential amplifier. Both wires pick up the same capacitively coupled noise, but their signals differ by the real electrons from the charge cloud collected by the more positively biased wire. These differential amplifiers yield extremely low noise signals. The time differences between a start signal, picked at front or back of the channel plate and the two signals from both ends of the wire pair is measured with two time-to-digital converters. The time difference is proportional to the position in the respective direction. For the position information in the perpendicular direction a second pair of wires is wound perpendicular

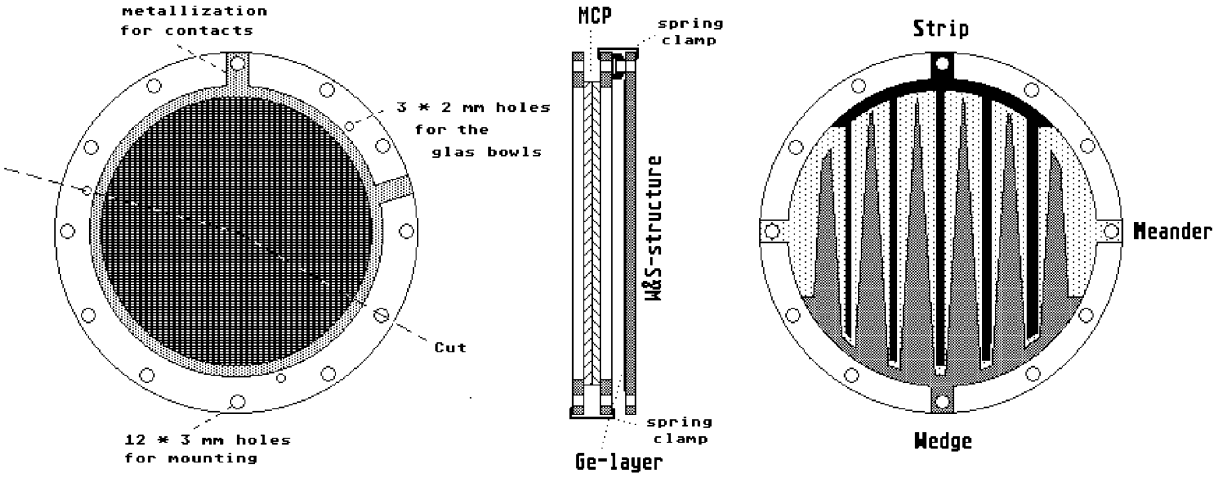

Fig. 17. Channel-plate detector with wedge-and-strip read out (from [124]).

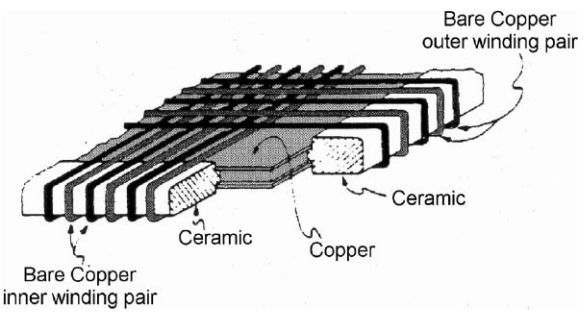

Fig. 18. Delay-line anode for multi channel-plate position read out (from [127]). The inner and outer winding pair are for x and y encoding. The two wires of each pair are on different potential such that the electrons are collected on one of them.

to the first one. Depending on the TDC used a position resolution of better than 0.1 mm can be achieved.

Compared to position encoding by charge division (as in a wedge-and-strip or resistive anode), the delay-line read out has many advantages. Since only fast timing electronics (fast amplifiers, constant fraction discriminators and TDCs) is used it is much faster, allowing for much higher rates (MHz). Furthermore, the absolute position resolution is constant, thus larger detectors with better relative resolution can be build easily. The position resolution does not directly depend on the gain but stays rather constant, once sufficient gain is achieved. The most important advantage for ion and electron imaging is the capability to handle multiple hits in ns time intervals. The dead time is mainly determined by the electronics. In practice 10–20 ns dead time between double hits has been achieved [79,128,129]. This dead time, however, is no principal limitation for up to two hits. The main reason is that in each spatial direction the arrival time of the signal is measured on both ends of the delay line. To obtain the position information only the arrival time on one of the ends is

needed. For more than two hits arriving within the delay time of the detector anode, which is 30–100 ns, depending on the size of the detector, some information is lost. Such multi-hit delay-line detectors have been used for detection of two and more electrons from a multiple ionizing collision [79] and for detection of ionic fragments from molecular coulomb explosion [128,129].

4. Experimental results for charged particle impact

4.1. One-electron processes

Two types of one-electron processes have been investigated with COLTRIMS: First the transfer of one electron from a bound state of the target to a bound state of the projectile and second the emission of one target electron to the continuum. A third possible one-electron process, target excitation, does not result in a charged recoil ion and is thus in most cases impossible to detect by COLTRIMS. The same is true for projectile ionization or excitation in a one-electron process, since these reactions do not result in a charged target ion either. We will first discuss single capture. It is the simplest process from the point of view of the final momenta since there are only two particles in the final state. We will then deal with single ionization which is more complex due to the three particles in the final state. Both processes are most important in ion-atom collisions: electron capture is by far the dominant process at low impact energies, while at high velocities target ionization dominates.

4.1.1. Single capture

For single capture the quantized nature of the Q-value (i.e. discrete values for the projectile energy loss or gain) leads to discrete values of $k_{||\mathrm{rec}}$. Thus, as outlined in Section 2 the measurement of $k_{||\mathrm{rec}}$ is equivalent to energy loss or gain spectroscopy and gives information about the final state to which the electron is captured. The simultaneous determination of $k_{\perp\mathrm{rec}}$ gives the information on the projectile scattering angle (i.e. on the impact-parameter dependence of the process). While in principle the measurement of the recoil ion momentum is, for single capture, equivalent to measuring the change of momentum (energy gain and scattering angle) of the projectile there are many practical advantages in detecting the recoil ion momentum. Detecting the projectile it is necessary to measure a very small change of a large incoming momentum. For the traditional projectile energy gain measurement this restricts the experiments to relatively low impact energies (keV/u). Typical resolutions are $\Delta E/E > 10^{-4}$. For the scattering angle measurement, depending on how well the incoming beam is collimated, $\Delta\vartheta_{\mathrm{pro}} > 10^{-5}$ is a practical limit for the resolution (for energy gain spectroscopy see, e.g. [130] and references therein). The recoil ion momentum measurement, however, is almost independent on the preparation of the incoming beam. Therefore it allows a high resolution energy gain measurement even for MeV impact energies, and very high resolution scattering angle measurement without a well collimated beam.

Mergel and co-workers have applied COLTRIMS to study the capture reaction

$$0.25 - 1\,\mathrm{MeV}\ \mathrm{He}^{2+} + \mathrm{He} \rightarrow \mathrm{He}^{1+} + \mathrm{He}^{1+}\ . \tag{19}$$

The distribution of $k_{||\mathrm{rec}}$ for 0.25 MeV is shown in Fig. 19.

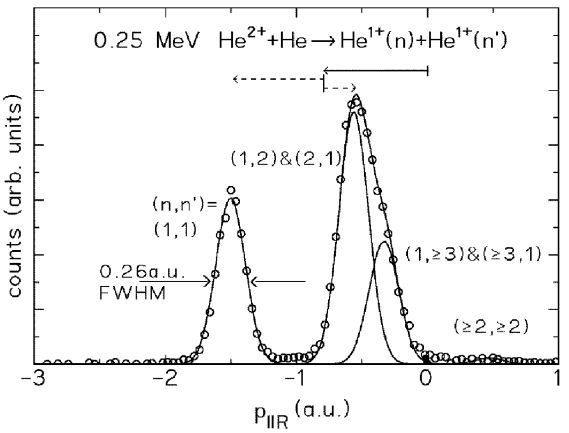

Fig. 19. Longitudinal momentum distribution for He^{1+} recoil ions from 0.25 MeV $He^{2+} \rightarrow$ He single capture collisions. The different lines correspond to capture to different final state configurations of target (n) or projectile (n′). The full arrow shows the momentum of $-v_{pro}/2$ due to the mass transfer and the dashed arrow the Q-value effect with $-Q/v_{pro}$ (K- and L-shell) (see Eq. (5)) (from [108]).

The left peak is due to capture to the He^{1+} ground state, the right peaks to capture to excited states. The experimental resolution of $\Delta k_{||rec} = 0.26$ a.u. was achieved with a spectrometer with extraction perpendicular to the ionic beam. This spectrometer had no electrostatic lens and a field of 0.33 V/cm at the target was applied (Fig. 9). Therefore, the limited resolution reflects approximately the diameter of the gas jet of 1.1 mm. This corresponds to an energy gain or loss resolution of the projectile of about $\Delta E/E_p = 1 \times 10^{-5}$. The full arrow indicates the backward momentum shift resulting from the mass transfer of the electron ($v_{pro}/2$) while the energy gain (for capture to the K shell) or energy loss (for capture to excited states) lead to momentum transfers shown by the dashed arrows. At about 0.5 MeV capture to the K and L is about equally likely. As can be expected from the consideration of velocity matching between electron and projectile, increasing projectile velocity results in a relative increase of K-capture compared to capture to excited states. Fig. 20 shows the recoil ion transverse momentum distribution $d\sigma/dk_{\perp rec}$ separated for capture to the K shell and to excited states. The resolution in the transverse direction is much better than in the longitudinal direction, because the source volume in this direction is given by the very well collimated beam (0.1 mm). Thus, a resolution of a few μrad can be achieved, much superior to any direct scattering angle measurement. The L-capture shows a smooth decrease while the K-capture exhibits an oscillatory structure which is well known for K-K vacancy transfer at lower impact energies [131]. Mergel and coworkers found these K-K interference structure up to a projectile velocity of about 2.5 a.u. [132,108].

Wu and coworkers [88] and Kambara and coworkers [133] have employed COLTRIMS to study single electron capture by 0.5–3.7 MeV/u O^{7+} and F^{9+} on He collisions. They could separate capture to the projectile K-shell from capture to higher excited states (see Fig. 21). In later studies this group achieved even much higher resolution [134] by using supersonic gas and focussing spectrometers. At the lowest velocity of 0.5 MeV/u capture to $n = 4$ and higher dominates by far. K-shell capture plays an increasing role at higher impact energies. The measured ratio of K-capture

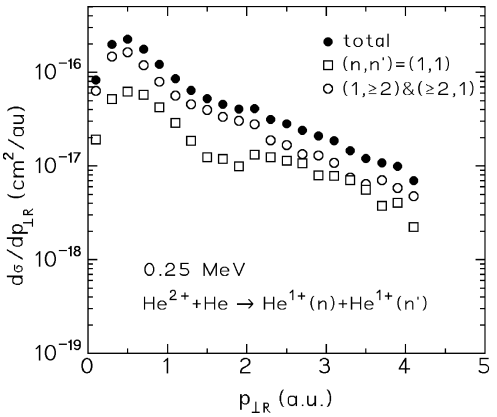

Fig. 20. Recoil ion transverse momentum transfer (i.e. scattering angle) distribution for 0.25 MeV $He^{2+} + He \rightarrow He^{1+} + He^{1+}$ for different final states of the capture process (from [108]).

to capture to excited states is well described by the Oppenheimer, Brinkmann Cramers theory. Thus, the projectile tends to capture to states which have mean orbital velocities similar to the projectile velocity.

At 8.7 MeV/u Kambara and coworkers reported also the transverse momentum distribution of the recoil ions. They found a maximum at around $k_{\perp \mathrm{rec}} = 1$ a.u. but could not confirm oscillations in the differential cross-section predicted by close coupling calculations [133].

For slow (6.8 keV/u) bare Ne and Ar on He collisions Cassimi and coworkers [109] have studied state selective cross-sections for single capture. With a recoil ion momentum resolution of 0.4 a.u. they obtained a resolution of 5 eV for the Q-value measurements. This allowed to separate capture to the $n = 4$ and $n = 5$ which was found to be the main channel for Ne^{10+} impact and $n = 7$ and $n = 8$ for Ar^{18+} impact. Their data confirm the predictions of the over-the-barrier model for the scaling of the average quantum number of the electron capture. In addition to $k_{||\mathrm{rec}}$ they measured the transverse momentum, too (see Fig. 22).

nCTMC (n-body classical trajectory Monte Carlo, see, e.g. [135,136]) calculation for this process reproduce the final-state distributions very well. The results of these calculations were also used to convert the measured transverse momenta to impact parameters. For Ne^{10+} impact the maxima in Fig. 22 correspond to impact parameters of 6.5 and 4.5 a.u. This is consistent with quantum mechanical curve crossing calculations. In a subsequent study by the same group Flechard et al. [110] have extended this study to double electron capture. In this work a major improvement in resolution by using a focussing lens was achieved.

Single capture for in the comparable collision system of Ar^{8+} on He has been investigated by Abdallah and coworkers [137]. They find that as the projectile velocity is raised from 0.2 to 1.0 a.u. the reaction window spreads and higher n and l values become the favored capture channels.

4.1.2. Target single ionization

The study of the reaction dynamics of single ionization has concentrated mostly on He targets. It is experimentally the easiest accessible target for COLTRIMS, allowing for the highest resolution.

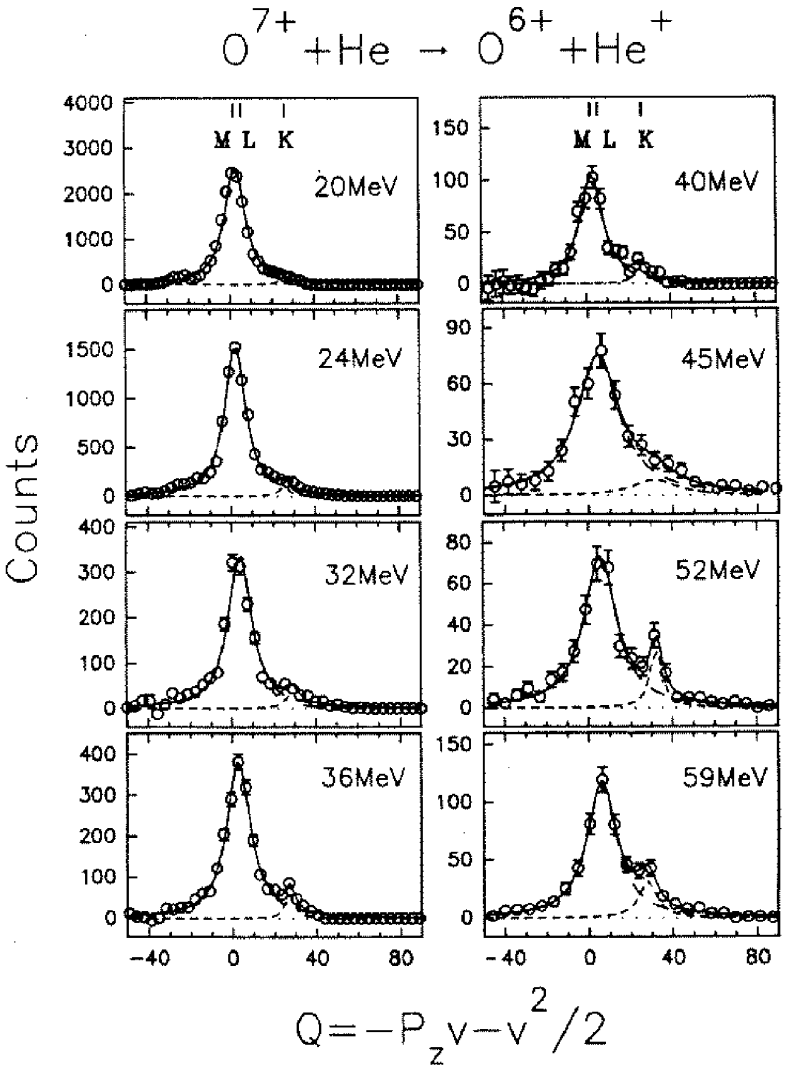

Fig. 21. Q-value spectra for single capture in O^{7+} He collisions. The spectra are obtained from the recoil ion longitudinal momentum. The location of expected Q-values for capture to K,L and M shells is indicated. The lines show Lorentzian fit for capture to K and L-and-higher shells (from [88]).

In general the collision dynamics for single ionization is almost unaffected by electron–electron correlation effects.

In general single ionization is a three-body momentum exchange process. One can approximate it by splitting it in three separate two-body momentum exchange processes, projectile–electron, projectile–ion and electron–ion. Although all three pairwise interactions are always present, there are paradigmatic cases where one of the three dominates. The fully differential studies of single ionization for different collision systems and studies performed in the CTMC model for the first time gave complete descriptions of the final momentum space of ionizing ion–atom collisions.

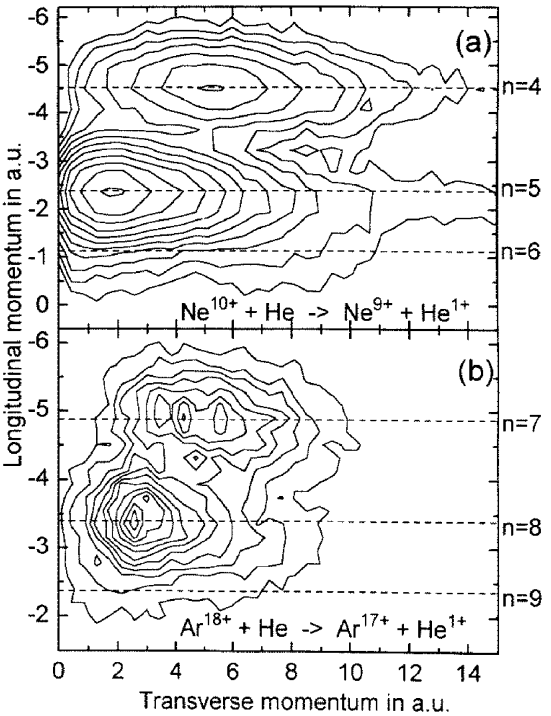

Fig. 22. Momentum distribution of recoil ions from single capture by 6.8 keV/u Ne^{10+} (a) and Ar^{18+} (b) projectiles. The dashed lines give the positions of capture to specific n states according to Eq. (5) (from [109]).

These multi-dimensional images unveil directly which of the momentum exchange processes is most important for the reaction. These studies reach for ion impact the same level of detail as has been reached for (e,2e) reactions using traditional coincident electron spectroscopy (see [9–11] for reviews). They go beyond (e,2e) studies by covering the full final state momentum space. Where traditional (e,2e) experiments result in angular distributions for fixed momentum transfer the fully differential ion impact studies discussed here give a complete overview in momentum space and therefore highlight the processes which contribute most to the total ionization cross-section (see [17,138,139]).

Figs. 23–25 demonstrate three paradigmatic collision systems. For slow p on He collisions the momentum exchange between projectile and target nucleus is by far the dominating one (Fig. 23), for fast proton on He collisions the projectile–electron momentum exchange becomes important (Fig. 24) and for very fast highly charged ion impact the electron-recoil ion momentum exchange dominates (Fig. 25). Each of these momentum exchange patterns suggest simple models for the ionization mechanism. We will group our discussion of target single ionization along this line and discuss single ionization in slow collision in Section 4.1.2.1, in fast proton and antiproton on He collisions in Section 4.1.2.2 and fast highly charged ion collisions in Section 4.1.2.3. For all three collision systems the recoil ion and electron momentum vector has been measured in coincidence event by event. Therefore knowing $\boldsymbol{k}_{\mathrm{rec}}$ and $\boldsymbol{k}_{\mathrm{e}}$ for each event $\boldsymbol{\Delta k}_{\mathrm{pro}} = -(\boldsymbol{k}_{\mathrm{rec}} + \boldsymbol{k}_{\mathrm{rec}})$ can be calculated.

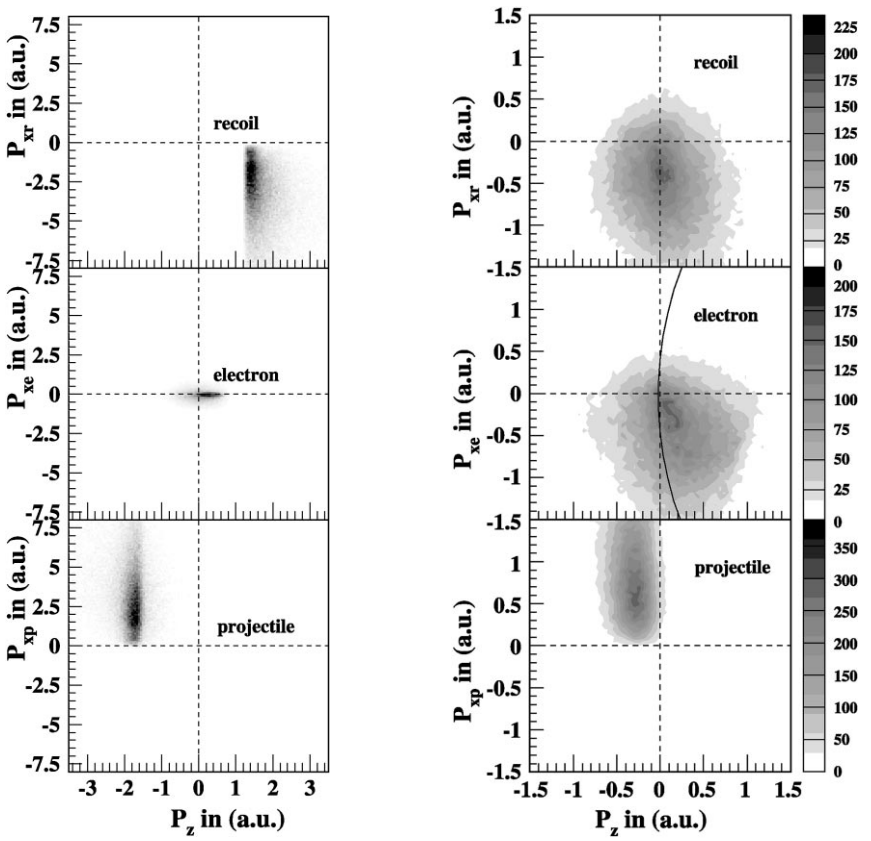

Fig. 23. Projection of the momentum transfer vectors of recoil ion (upper) electron (middle) and projectile (lower) in the final state onto the plane defined by the projectile beam and the momentum vector of the recoil ion for 10 keV/u $p + \mathrm{He} \rightarrow \mathrm{He}^{1+} + e^- + p$. The $+p_z$ axis is parallel to the incoming projectile direction, the $+p_y$ axis is parallel to the final transverse momentum component of the recoil ion. The grey scale represents the corresponding doubly differential cross section $\mathrm{d}^2\sigma/(\mathrm{d}k_x\,\mathrm{d}k_{||})$ on a linear scale (similar to [31]). A blowup of the electron distribution is shown in Fig. 26.

Fig. 24. 0.5 MeV/u $p + \mathrm{He} \rightarrow \mathrm{He}^{1+} + e^- + p$. Projection of the momentum transfer vectors of recoil ion (upper) electron (middle) and projectile (lower) in the final state onto the plane defined by the projectile beam and the scattered projectile (not by the recoil ion as Figs. 23 and 25). The $+p_z$ axis is parallel to the incoming projectile direction, the $+p_y$ axis point in the direction of the scattered projectile. The grey scale represents the corresponding doubly differential cross section $\mathrm{d}^2\sigma/(\mathrm{d}k_x dk_{||})$ on linear scale. The circular arc in the middle figure shows the location of the binary encounter ridge for electrons (from [84]).

4.1.2.1. Slow collisions. In slow collisions, i.e. if the projectile velocity is smaller than the mean electron velocity in a Bohr orbit, promotion of an electron to the continuum is typically less likely then capture to a projectile bound state (see, for example, Fig. 3). The question of which mechanism is responsible for electron emission in such slow collisions is far from answered. The momentum exchange between projectile and target nucleus is generally much larger than the momentum transfer to the emitted electrons in such slow collisions (see Fig. 23). In the transverse direction recoil ion and projectile are scattered oppositely as a result of the internuclear repulsion. From this

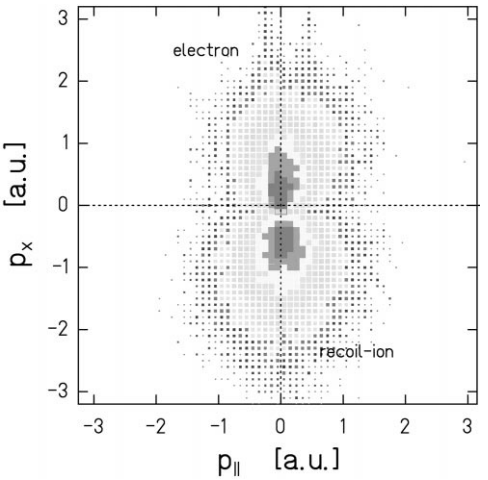

Fig. 25. 1 GeV/u $U^{92+} + He \rightarrow He^{1+} + e^- + U^{92+}$. Projection in momentum transfer components of electron and recoil ion in the final state onto the plane defined by the recoil ion and the beam (as in Fig. 23). The $p_\parallel$ axis is parallel to the incoming projectile direction, the $-p_x$ axis is parallel to the final transverse momentum component of the recoil ion. The momentum change of the relativistic heavy ion is much smaller than the electron and ion momenta. It is not shown, since it reflects mainly the experimental resolution. The cluster size represents the corresponding doubly differential cross section $d^2\sigma/(dk_x dk_\parallel)$ on logarithmic scale (from [81]). Compare also Fig. 36.

transverse momentum exchange the impact parameter can be inferred, if the effective potential is known. The scattering plane is defined by the beam direction and the final state recoil ion momentum vector. In the longitudinal direction the recoil ions are emitted strongly in forward direction. This large longitudinal momentum transfer to the recoil ion requires a strong coupling of the ionic core to the forward motion of the slow projectile. In the intermediate quasimolecular system the electrons act as a 'glue' which allows the recoil ion to follow the forward motion of the projectile. As can be seen in Fig. 3, in most of the cases the electron in the quasimolecular orbital is, however, not emitted to the continuum but captured to projectile orbital (see also [140]). Those few electrons released to the continuum are found mostly with very little momentum in between target and projectile frame (see Fig. 23).

Thus in terms of mechanisms (i.e. dynamics) the forward emission of the recoil ions in slow collisions can be seen as a manifestation of the molecular character of the ionization process. From the perspective of kinematics this forward emission follows directly from Eq. (6). E.g. at 10 keV/u impact energy the momentum exchange resulting from the energy transfer of the He target binding energy is already $E_{\text{bind}}/v_{\text{pro}} = 1.4$ a.u.

To investigate the mechanism of ionization in slow collisions it is helpful to look for the details of the electron momentum distribution. Dörner and coworkers [73] have used a spectrometer as shown in Fig. 12. For the reaction

$$5 - 15\,\text{keV}p + \text{He} \rightarrow p + \text{He}^{1+} + e^- \tag{20}$$

they have mapped the square of the continuum wave function of the emitted electron in momentum space for fully controlled motion of the nuclei. Figs. 26(a)–(c) show the two-dimensional velocity

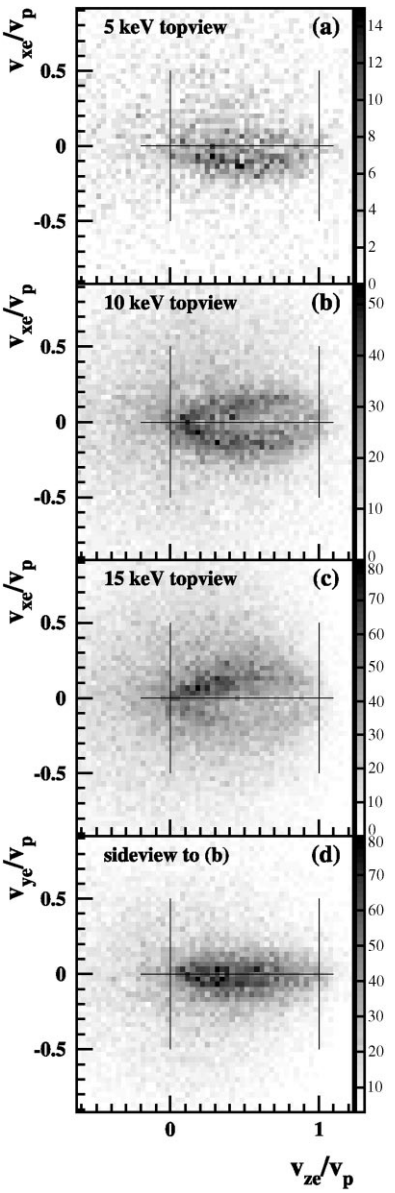

Fig. 26. Projection of the velocity distribution of electrons for single ionization in 5 (a), 10 (b) and 15 (c) keV p–He collisions onto the scattering plane, defined by the incoming projectile axis (z) and the final momentum vector of the recoil ion, emerging to the -x direction. The target center is at (0,0) the projectile at (1,0) and the saddle at (0.5,0) The data for 10 keV are for a transverse momentum transfer in the interval $k_{\perp\mathrm{rec}} = 1$–5 a.u.. For the other energies this momentum range is scaled by $1/v_{\mathrm{pro}}$ in order to sample approximately the same range of impact parameters. (d) sideview to (b), i.e. projection onto the y–z plane perpendicular to the x–z scattering plane (from [73]).

distribution of the electrons from reaction 20 projected onto the scattering plane, defined by the beam and the recoil ion momentum vector. The horizontal z-axis is the direction of the incoming projectile. The y-axis points to the direction of the scattered projectile transverse momentum, while

the recoil ion is emitted into direction-y in Figs. 26(a)–(c). The x-axis in figure (d) is perpendicular to the beam and the recoil ion momentum. Velocities are scaled to the projectile velocity. Target centered electrons are located at (0,0) while electrons captured to the projectile continuum (ECC) could show up at (1,0). The saddle point of the potential is located at (0.5,0). A sideview onto the distribution of (b) is shown in (d), i.e. a projection onto the y,z plane. The electron momentum distributions shown in Fig. 26 for 10 keV are in coincidence with recoil ions within $1 < k_{\perp\mathrm{rec}} < 5$ a.u. This is the region where most of the ionization cross-sections results from. For all projectile velocities shown the electrons are strongly forward emitted. While for 5 keV the electrons are emitted preferentially onto the side where the projectile passes by, at 15 keV they are emitted to the direction of the recoiling ion. At 10 keV even a horseshoe-shaped emission pattern is observed. All these distributions are very different from the well-known structures in the electron spectra at high energies. They are a result of quasimolecular promotion via different series of transitions [141–144]. The part of the structure at 10 keV around the saddle point indicates a π state in the continuum on the saddle point. It can be populated via a rotational coupling from the 1s ground state (T001 series of transitions [141]). Such promotion patterns have been predicted by the theory of hidden crossings [141,142]. Recently, Macek and Ovchinnikov showed that an interference between sigma and pi components of the electronic wave function can give rise to the observed rapid oscillation in the electron emission as a function of projectile velocity [145].

On grounds of classical mechanics Olson and coworkers have suggested the mechanism of promotion of the electron on the saddle of the internuclear potential [146–148]. For 15 keV impact energy CTMC calculations yielded very good agreement with the observed $k_{\perp\mathrm{rec}}$ distributions for ionization and were able to reproduce the main features of the electron emission [73]. The final state momentum distribution from these calculations was very sensitive to the initial state momentum and spatial distribution, for which a Wigner distribution of 10 initial binding energies had to be used. This reproduces the quantum mechanical radial distribution very well over 4 orders of magnitude.

Abdallah and coworkers reported a study of the electron emission Ne^{1+} on Ne [75] collisions and He^{1+} and He^{2+} on He collisions [75]. Their continuum structures for the Ne and He case differ significantly. The authors conclude that the continuum momentum distribution of the electrons is determined by the final molecular orbit the electron occupied. For He on He collisions the continuum shows π structure similar to the p on He case shown in Fig. 26 while for Ne^{1+} on Ne a spiral electron distribution is found together with the fact that ionization occurs in a small impact parameter window. This indicates a promotion of the electron through the $4f\sigma_u$ MO.

4.1.2.2. Fast p and $\bar{p}$ on He collisions. For fast p-on-He collisions (v_{pro} several a.u.) the target electrons do not have enough time to adiabaticlly adapt to the rapidly changing two-center potential. On the other hand, now the projectile is fast enough that even a pure two-body collision with the target electron can transmit sufficient energy to ionize the electron. Fig. 24 suggests that in most of the collision this projectile-electron momentum exchange is important. (Note that in Fig. 24 the scattering plane is defined by the incoming and scattered projectile momentum vector.)

This has been first suggested by measurements of the projectile scattering angle dependence $(\mathrm{d}\sigma/\mathrm{d}\vartheta_{\mathrm{pro}})$ for single ionization [149–153] at much larger momentum transfer. The details, however, could only be unveiled in coincidence experiments which measured the projectile scattering (polar

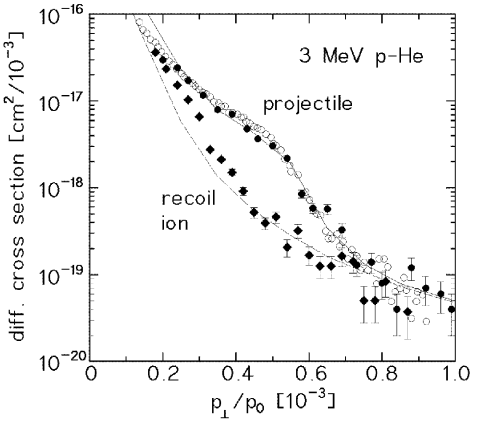

Fig. 27. Differential cross section for 3 MeV p + He $\rightarrow p + He^{1+} + e^{-}$ as function of the transverse momentum transfer to the projectile $k_{\perp pro}$ (equivalent to the projectile scattering angle) and to the recoil ion $k_{\perp rec}$. Full circles: experiment $k_{\perp pro}$ [59], open circles: experiment $k_{\perp pro}$ [149], diamonds: experiment $k_{\perp rec}$ [59]. Lines: *n*CTMC (from [59]).

and azimuthal angle) in coincidence with the transverse momentum of the recoiling ions [51–59,98,154,155].

For scattering from an electron at rest the maximum projectile scattering angle ϑ_{crit} is given by arctan $\vartheta_{crit} = m_e/m_p$ ($\vartheta_{crit} = 0.55$ mrad for protons). Kamber and coworkers [149,150] have found a shoulder at this critical angle in the differential cross section $d\sigma/d\vartheta_p$ for ionizing collision of 3 and 6 MeV p on He (see Fig. 27). They showed that for scattering angles between 0.2 and 0.55 mrad, the cross-section could be well described by a Rutherford scattering process from a free electron. Over this angular range the transverse momentum exchange would thus be dominated by a hard binary encounter between projectile and target electron. These collisions are dominated by large impact parameters with respect to the target nucleus, but small impact parameters between projectile and emitted electron. Gensmantel and coworkers [59,54] could experimentally manifest this interpretation by measuring the transverse momentum distribution of the recoiling ions $d\sigma/dk_{\perp rec}$ (Fig. 27) with a cooled target gas cell (see Fig. 6). They found, as expected from the above interpretation, a smooth $d\sigma/dk_{\perp rec}$ with no shoulder.

At a projectile scattering polar angle of 0.73 mrad they found two peaks in the transverse recoil ion momentum distribution, which could be associated with the scattering of the projectile at the target nucleus (leading to large recoil momenta) and at the electron (leading to small recoil momenta), respectively (see Fig. 2 in [59]). More recently DeHaven and coworkers [156] confirmed these findings. For 6 MeV *p*-on-He collisions they measured the scattering angle of the projectile in coincidence with the recoil ion momentum component in the direction of the projectile scattering and found two clear cut ridges originating from projectile scattering at the nucleus and at the electron (see Fig. 28).

At smaller impact energies the shoulder in the $d\sigma/d\vartheta_{pro}$ washes out due to the momentum distribution of the electrons in the initial state [151,153]. For 0.5 MeV *p*–He collisions Dörner and coworkers [51] measured the transverse recoil ion energy as a function for the projectile scattering angle (see Fig. 29). They distinguished three regions of projectile scattering. At large scattering angles ($\vartheta_{pro} > 0.9$ mrad) the projectile scattering is determined by the interaction between the two

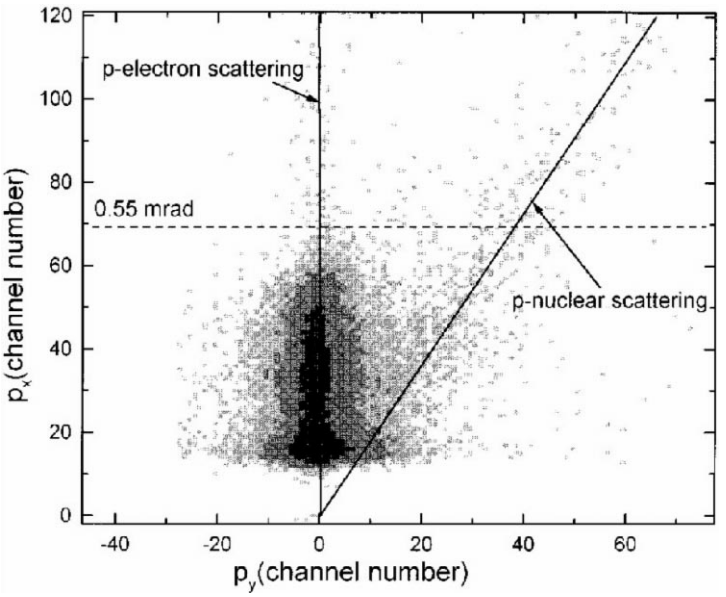

Fig. 28. Single ionization in 6 MeV p-on-helium collisions. The horizontal axis is the recoil ion momentum component transverse to the beam and in the plane defined by the scattered projectile (0.39 a.u./channel). The vertical axis show the projectile transverse momentum (0.21 a.u./channel). The cutoff for small scattering angles results from a beam block on the projectile detector. The dashed line locates a projectile scattering angle of 0.55 mrad. The loci of events corresponding to projectile–nucleus and projectile–electron scattering are indicated by full lines (compare also Fig. 2 of [59]).

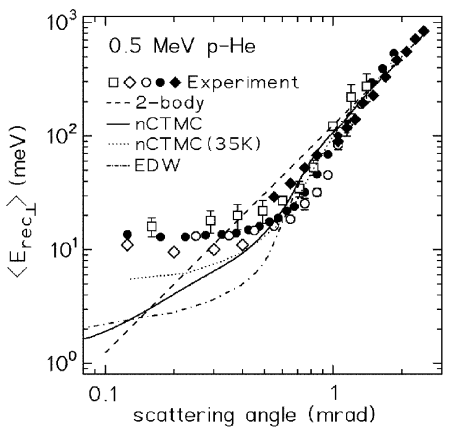

Fig. 29. Mean transverse energy of He^{1+} ions from 0.5 MeV p–He collisions as a function of the projectile scattering angle. Symbols: different experiments (partly from [51,58]). The scatter in the data represents the systematical error due to uncontrolled electric fields in the cooled gas cell used in this experiment. Dashed line: two-body scattering of the projectile at the target nucleus, full line: nCTMC calculation [98] (see also [58]), these results are different from the nCTMC results in [51], which were found to be in error (see [54]), dotted line: nCTMC folded with the target thermal motion at 30 K, dashed dotted line: Eikonal distorted wave calculation [157,158] (from [53]). Recent experiments with a supersonic gas-jet target by Weber et al. [84] give evidence that the saturation energy of 10 ± 5 meV at small scattering angles is at the upper limit of the error bart including the shift to higher energies due to the target thermal motion. They measured energies down to 1 meV.

nuclei. At these close collisions the recoil ion energy is given by the nuclear–nuclear two-body collision kinematics and the He^+ and the proton are emitted back to back [55]. At scattering angles around 0.55 mrad, the recoil ion energy is much smaller than expected from a nuclear two body scattering, giving evidence that the projectile deflection is mainly caused by a hard collision with the emitted electron. As a consequence the recoil ion and projectile are no longer emitted back to back (see [55]).

At small scattering angles the recoil energy becomes independent of the projectile scattering. In this regime the electron–recoil ion momentum exchange dominates. These transverse momentum exchange processes are well described by *n*CTMC calculations [51,58,159,160] as well as by quantum mechanical calculations in the Continuum Distorted Wave approach [157,158,161,162].

In these early RIMS studies the transverse momenta of the He^{1+} ions was measured in coincidence with the projectile scattering angle. Recently Weber et al. [84] investigated the same collision system measuring the three-dimensional momentum vector of the electron and the ion in coincidence using a spectrometer as shown in Fig. 12. They succeeded in imaging the complete 9 dimensional final-state momentum space with a resolution of about 0.2 a.u. (see Fig. 24). The high resolution allows to focus on the region of small momentum exchange, which yields by far the dominant contribution to the total cross-section. In this recent study they found transverse recoil ion energies as low as 1 meV for projectile scattering angles below 0.1 mrad. Thus, one can conclude, that the early results from static gas target devices shown in Fig. 29 give a much too high 'saturation' energy for the ions at small projectile scattering angles.

As outlined above, the coincident recoil ion electron momentum space imaging with todays COLTRIMS systems yields for single ionization the momentum vectors of all particles for each registered event. This multi-dimensional array of data can be looked at from many different perspectives. One perspective on such data for He single ionization by fast projectiles has already been discussed with Fig. 24. Here the three-body momentum distributions are projected onto the plane defined by the incoming projectile (z) and the scattered projectile (x). As a second useful perspective at the same data is a projection onto the plane perpendicular to the projectile beam (xy plane) (Fig. 30). For this projection one is free to choose one axis along the transverse momentum of one of the particles and than display the momenta of the others in this coordinate frame. In Fig. 30(a) the vertical axis is given by the transverse momentum vector of the recoil ion ($k_{\perp \mathrm{rec}}$) (the direction of the recoil ion is indicated by the arrow). The horizontal axis is perpendicular to the beam and $k_{\perp \mathrm{rec}}$. The momentum distributions of the projectile is plotted. Fig. 30(b) shows the electron momentum distribution in the same coordinate system. In Fig. 30(c) again the electron momenta are shown, but now in a coordinate system where the vertical axis is given by the transverse momentum of the scattered projectile (arrow). The distributions show that the projectile is scattered at both the target nucleus and the electron, and that there are a large number of events where the electron and recoil ion emerge to opposite sides. A more complete view on these data in different coordinate systems can be found in [84].

It is obvious from Fig. 30 that the projectile–electron momentum exchange is important in most of the ionizing collisions. This is supported by Fig. 31 which shows the azimuthal angles between the three transverse momenta. One finds strong contributions with back-to-back emission between electron and projectile.

Moshammer and coworkers have first used the azimuthal angular plot of Fig. 31 to illustrate the ionization mechanism in fast highly charged ion–atom collisions (see Section 4.1.2.3 and Fig. 37).

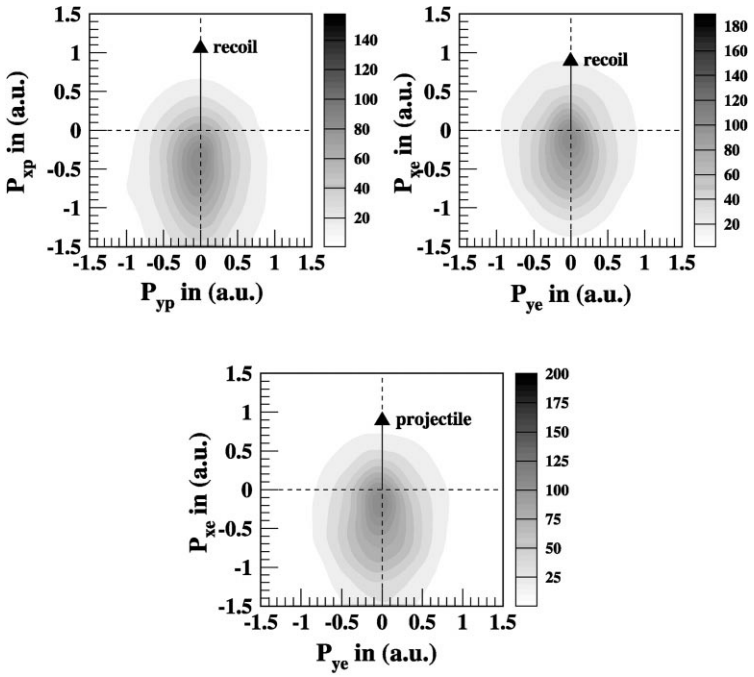

Fig. 30. 0.5 MeV $p + \mathrm{He} \rightarrow p + \mathrm{He}^{1+} + e^-$ All three panels show the momentum plane perpendicular to the incoming projectile, which moves into the plane of the paper. (a) shows the momentum distribution of the projectile, the vertical axis (labelled ΔP_{xp}) is along the transverse momentum of the recoil ion. (b) shows the momentum distributions of the electrons in the same coordinate frame as (a), in (c) the vertical axis is the direction of the transverse momentum of the scattered projectile, the electron momenta are shown (see text) (from [84]).

They pointed out that the three borders of the triangle have a direct connection to a particular ionization mechanism. The diagonal line $\phi_{\text{pro-rec}} + \phi_{\text{e-rec}} = 180 = \phi_{\text{e-pro}} = 180^\circ$ corresponds to a binary-encounter between projectile and electron, $\phi_{\text{pro-rec}} = 180^\circ$ to a pure nuclear–nuclear deflection as observed for slow collisions (see Section 4.1.2.1) and $\phi_{\text{e-rec}} = 180$ is the kinematics equivalent to photoionization (see Sections 4.1.2.3 and 5).

We now focus on the longitudinal momentum balance in fast p–He collisions. For single ionization by fast heavy particle impact the recoil ion longitudinal momentum $k_{\|\text{rec}}$ for each collision can be calculated from the electron ejection angle (ϑ_e) and the electron energy (Eq. (6)). Thus, the information about the electron spectra can be obtained from the $k_{\|\text{rec}}$ distributions and vice versa. As a consequence of this there are simple formulas to connect differential cross sections for electron emission and those for $k_{\|\text{rec}}$ [83]

$$\frac{\mathrm{d}\sigma}{\mathrm{d}k_{\|\text{rec}}} = \int_{\varepsilon_e^-}^{\varepsilon_e^+} \frac{1}{k_e} \frac{\mathrm{d}^2\sigma}{\mathrm{d}\varepsilon_e\, \mathrm{d}(\cos\vartheta_e)}\, \mathrm{d}\varepsilon_e \tag{21}$$

The integration limits for the electron energy $\varepsilon_e^{\pm} = 1/2(k_e^{\pm})^2$ are

$$k_e^{\pm}(\vartheta_e) = v_{\text{pro}} \cos\vartheta_e \pm \sqrt{v_{\text{pro}}^2 \cos\vartheta_e^2 + 2(k_{\|\text{rec}}\, v_{\text{pro}} - |\varepsilon_{\text{bind}}|)}\ . \tag{22}$$

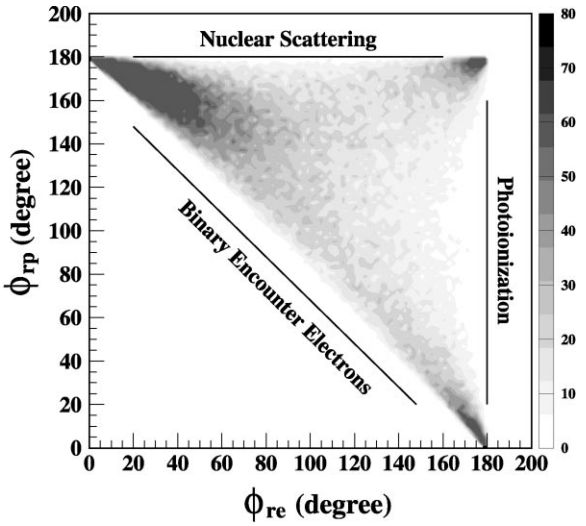

Fig. 31. 0.5 MeV $p + He \rightarrow p + He^{1+} + e^-$ Azimuthal angle between recoil ion and electron plotted versus that between recoil ion and projectile. Indicated are the kinematical lines assuming the specified two body interaction and considering the third particle as a spectator. The region below is kinematically forbidden. (from [84]) (compare to same presentation for fast highly charged ion impact, Fig. 37).

Tribedi and coworkers have used these relations to calculate recoil ion longitudinal momentum distributions from measured doubly differential electron spectra [85]. From this perspective the advantage of measuring $k_{||rec}$ is that it always samples all electrons (at all angles and energies), which is difficult with traditional electron spectroscopy. And even more important, since $k_{\perp rec}$ is simultaneously measured, the detection of only one particle, provides information about electron emission differential in the transverse momentum exchange (i.e. for closer collisions the impact parameter).

Besides from its kinematical connection to electron emission, the $k_{||rec}$ distribution can be, and has always been, discussed in terms of forces which act on the nucleus and mechanisms which dominate the ionization process. For 0.25–1 MeV p and He^{2+} impact on He Dörner and coworkers [112] have measured the $k_{||rec}$ distribution. They observed very similar recoil ion longitudinal momentum distribution $d\sigma/dk_{||rec}$ for these projectile velocities and charge states. The mean value of the $k_{||rec}$ distribution is only slightly shifted backward from 0. At 0.5 MeV impact energy it is very close to the Compton profile of the He (see Fig. 32). Thus the final state momentum distribution reflects closely the momentum in the initial state. Only for close collisions, i.e. large $k_{\perp rec}$ the $k_{||rec}$ distribution gets much broader, indicating faster electrons and more coupling between the projectile, electron and ionic motion. The data are in reasonable agreement with nCTMC calculations which implicitly include the interaction between ion, emerging electron and projectile to all orders. Rodriguez and coworkers have shown [83] that in a quantum mechanical treatment one has to go beyond the Plane Wave Born Approximation to describe the distribution at 0.25 MeV while at 1 MeV a first-order treatment gives very good results. They employed the Continuum Distorted Wave Eikonal Initial State (CDW-EIS) approximation to include a post

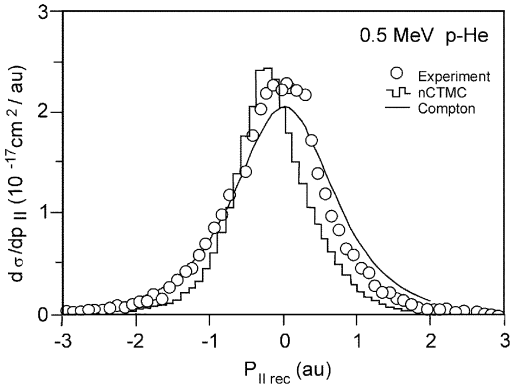

Fig. 32. Longitudinal recoil ion momentum distribution for single ionization in 0.5 MeV p–He collision. Open circles: experiment, full line: nCMTC, histogram: nCTMC (from [112]).

collision interaction. Including these higher-order effects results in a backward shift of the calculated distribution in agreement with the experiment.

Wang and coworkers [163] illustrated the correspondence between the $\mathrm{d}^2\sigma/\mathrm{d}E_\mathrm{e}\,\mathrm{d}\vartheta_\mathrm{e}$ and $\mathrm{d}\sigma/\mathrm{d}k_{||\mathrm{rec}}$ by looking at recoil ion momentum distributions for fixed electron emission angle $\vartheta_\mathrm{e} = 0$. They emphasize that electrons in the binary-encounter peak of the electron spectrum lead to recoil ions with a momentum distribution given by approximately the Compton profile, centered at $k_{||\mathrm{rec}} = 0$.

Weber et al. [84] and Khayyat et al. [118,119] have measured the longitudinal momentum distribution of electrons and recoil ions for single ionization by fast protons and antiprotons. For 1 MeV impact energy they find almost identical longitudinal electron and ion momentum distributions for proton and antiproton impact (see Fig. 33). This is in good agreement with CDW-EIS and CTMC calculations at this impact energy. The ionic momentum distributions found in these studies for proton impact are in agreement with the earlier work shown in Fig. 32 [112]. For smaller impact velocities a post-collision effect is expected, which separates electrons and ions in momentum space. Two experiments confirm this prediction and observed a significant forward emission of electrons from proton impact at velocities of 2–4 a.u. [84,71]. A detailed analysis of the charge state dependence of these momentum exchange patterns at an impact velocity of 100 keV/u within the nCTMC approach can be found in Ref. [164]. This post-collision effect is much stronger for highly charged ion impact, as illustrated in the following section (see, e.g. [76]).

4.1.2.3. Fast highly charged ion collisions. For collisions of fast highly charged ions with He the momentum exchange patterns are very different from those by fast proton impact (see Fig. 25). Moshammer and coworkers have investigated 1 GeV/u U^{92+} impact on He [81]. They found that for relativistic collisions the momentum exchange between recoil ion and emitted electron by far dominates over the momentum exchange with the projectile. The projectile carrying 0.24 TeV of energy induces an 'explosion' of the atom by delivering only the energy but almost no momentum. This fragmentation pattern has the characteristics of the photoionization process (see Sections 2.3 and 5). The common nature of fast charged particle and photons interacting with matter was discussed already by Fermi et al. [165,166]. In their approach ionization of an atom by charged

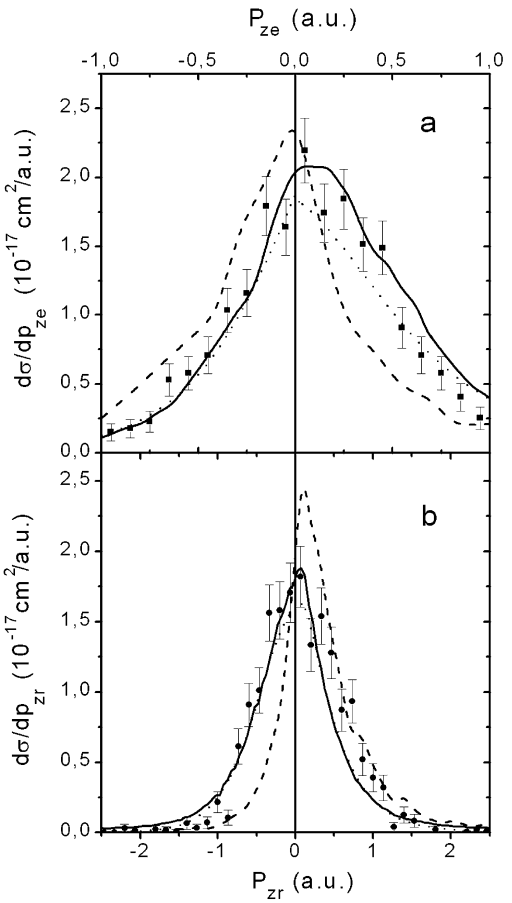

Fig. 33. Longitudinal momentum distribution for single ionization of Helium by 1 MeV antiproton (data points) in comparison with proton collision (solid line). (a) represents electron momentum data, (b) recoil ion momentum data. The theoretical calculations represent antiproton impact, where the dotted line shows CDW and the dashed line a CTMC-results. (from [119]).

particles is modeled as photoionization by a field of equivalent photons of various energies (equivalent photon method). The photon field is obtained by a Fourier transformation of the time and impact parameter depended electromagnetic field of the passing projectile. A 1 GeV/u U^{92+} ion generates a sub attosecond (10^{-18} s) superintense ($I > 10^{19}$ W/cm^2) field of virtual photons, shorter and more intense than any laser. The momentum exchange pattern in these relativistic collisions could also be well reproduced in relativistic *n*CTMC calculations [167].

Fig. 34 shows that the longitudinal momentum distributions of electrons and ions in such collisions are identical and symmetric around zero. The ionization cross-section is very well described by a calculation using the equivalent photon method (see Refs. [81,165,166,168,169]) and by relativistic *n*CTMC calculations [167].

Going to nonrelativistic collisions (e.g. single ionization by 3.6 MeV/u Se^{28+} and Ni^{24+} impact) Moshammer et al. have shown that electrons and ions are still emitted mainly back to back [76,121,122,170]. Even though the equivalent photon method is generally not expected to be valid

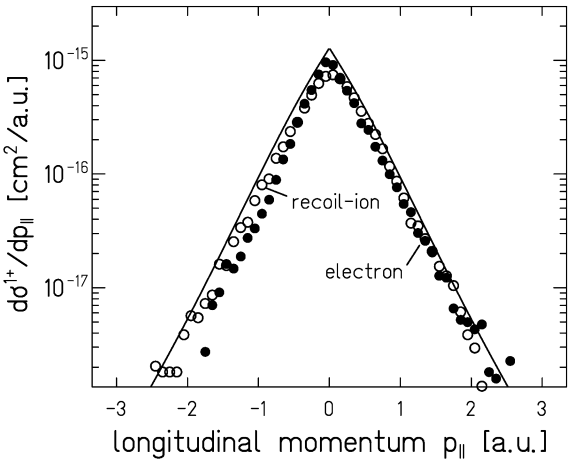

Fig. 34. Longitudinal momentum distribution of electrons (dots) and of recoil ions (open circles) for single ionization of He in collisions with 1 GeV/u U^{92+}. Full line: equivalent photon method (from [81]).

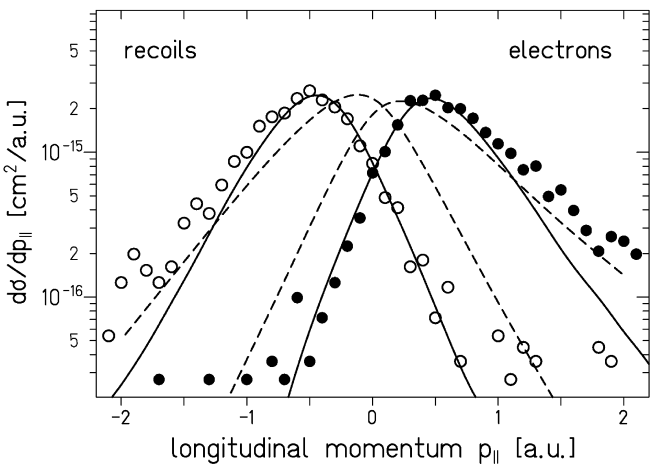

Fig. 35. Longitudinal momentum distribution of low-energy electrons (full circles) and recoil ions (open circles) for single ionization of He in collisions with 3.6 MeV/u Ni^{24+} (from [76]). (The experimental data are distorted by a calibration error and need to be shifted by about $+0.2$ a.u. for the recoil ions and -0.2 a.u. for electrons (see text).)

in this velocity regime, the experiments show that the projectile momentum exchange is much smaller than the recoil ion and electron momenta. On the outgoing part of the trajectory the post-collision interaction with the potential of the Ni^{24+} becomes important pushing the He^{1+} ions backward and pulling the electron forward (see Fig. 35). These conclusions are supported by *n*CTMC calculations. If in the calculations the sign of the projectile charge is changed from $+24$ to -24, the recoil ions are moved forward while the electrons are pushed backward. More accurate new studies [171] indicate that the experimental electron distribution in Fig. 35 and in Refs. [76,79,122] need to be recalibrated by about 0.2 a.u. into the negative $k_{\|}$ direction whereas the

recoil ion distribution is shifted forward by the same amount. These corrected data along with recent results on Au^{54+} on He collisions [172] are in very close agreement with the CDW calculations. The data of Fig. 34 from the same group are not affected by this correction of the early calibration. Thus the CTMC seems to overestimate the post-collision effect systematically. Recently, the initial state distribution of the electrons in the CTMC model was improved. Using a Wigner distribution with 10 different binding energies the quantum-mechanical initial state distribution of the electron momentum as well as of its radial distribution was reproduced over many orders of magnitude. The improved model predicts a significantly reduced post-collision effect and the theoretical results are in close agreement with the experiment [172].

CDW-EIS calculations by Rodriguez and coworkers [83] and CDW calculations by O'Rourke et al. [173,174] which include the effect of post collision interaction did reproduce the electron as well as the recoil ion momentum spectra.

In a systematic study of a very similar system (3.6 MeV/u Se^{28+} on He) Moshammer et al. have discussed the transverse momentum balance as well. Fig. 36 shows the two-dimensional momentum distributions of all fragments in the plane spanned by the beam and the recoil ion momentum. A comparison of Figs. 36 and 25 strikingly shows the polarization of the fragment distribution by the post collision interaction with the projectile.

The similarity to photoionization is again highlighted by the azimuthal angular dependence of the transverse momentum exchange. In the longitudinal direction the approximate compensation of electron and ion longitudinal momenta for large v_{pro} results already from the conservation laws (see Eq. (6)). In the transverse direction however there are no kinematical restrictions. Thus the transverse momentum balance gives an even clearer probe of the dominating ionization mechanism. Fig. 37 shows the azimuthal angular distribution of the fragments. The main contribution to the cross-section comes from azimuthal angles of close to 180° between recoil ion and electron as it

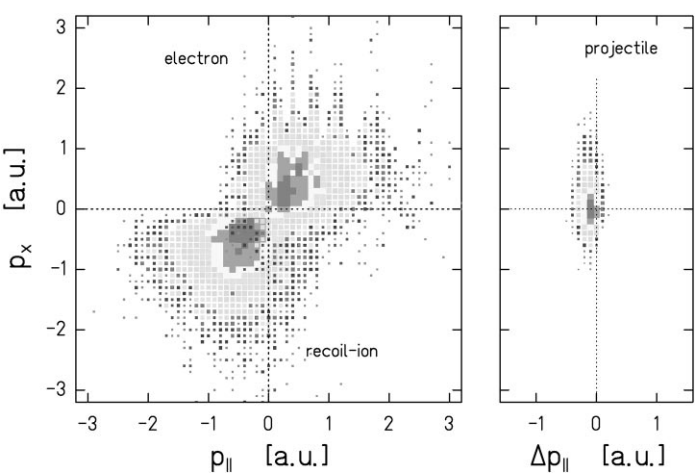

Fig. 36. 3.6 MeV/u $Se^{28+} + He \rightarrow He^{1+} + e^- + Se^{28+}$. Projection in momentum space of all particles in the final state onto the plane defined by the beam (horizontal axis) and the recoil ion transverse momentum (negative vertical axis). The cluster size represents the corresponding doubly differential cross-section $d^2\sigma/(dk_x\, dk_{||})$ on logarithmic scale (from [122]). Compare to Figs. 23–25.

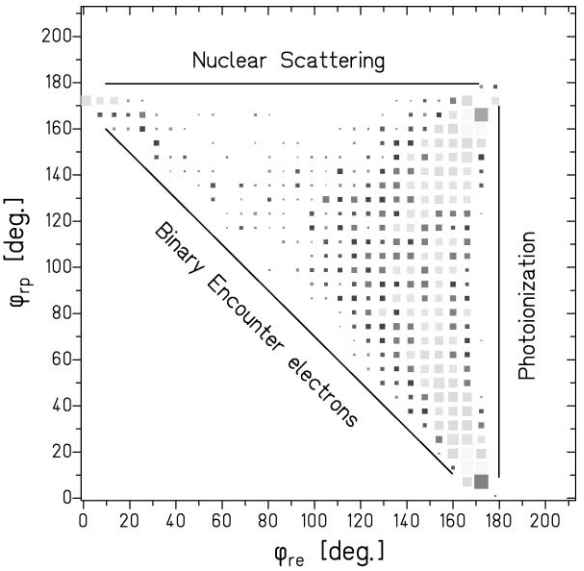

Fig. 37. 3.6 MeV/u $Se^{28+} + He \rightarrow Se^{28+} + He^{1+} + e^-$ Relative azimuthal angle between recoil ion and electron (ϕ_{re}) plotted versus that between recoil ion and projectile (ϕ_{re})p. Indicated are the kinematical lines assuming the specified two-body interaction and considering the third particle as a spectator. The region below the line entitled '*Binary encounter electron*' is kinematically forbidden. (from [122]) (compare to same presentation for fast proton impact, Fig. 31).

is the characteristics of photoionization. This is in striking contrast to the same presentation for single ionization by fast protons shown in Fig. 31.

4.1.3. Connection of single ionization and single capture in the recoil ion kinematics

Electrons stripped from the target will either be in the continuum (ionization) or in a bound state of the projectile (electron capture). The transition between capture and ionization can be viewed from the perspective of all particles: the electron, the projectile and the recoil ion. In the doubly differential cross-section for electron emission ($d^2\sigma/dE_e\, d\vartheta_e$) the attractive potential of the projectile leads to a divergence at $\vartheta_e = 0$ and $E_e = 1/2v_{pro}^2$. This 'cusp'-shaped maximum in the electron spectra, resulting from electrons travelling with the projectile but not being bound has been studied extensively in electron spectroscopy (for a review see [175]). In electron energy space there is a clear cut between capture and ionization. From the perspective of the recoil ion momentum, however, there is a natural and smooth transition from capture to ionization. All recoil ions with $k_{||rec} < k_{||rec}^{min}$ (see Eqs. (4)–(7) and (10) for definition) result from capture while those with $k_{||rec} > k_{||rec}^{min}$ are due to ionization. The threshold $k_{||rec}^{min}$ corresponds to electrons in the 'cusp', travelling with the projectile without being bound (see Eq. (10)). Rodriguez and coworkers [83] emphasized that the cusp yields a step (i.e. a finite cross-section and not a soft onset) in the $d\sigma/dk_{||rec}$ at $k_{||rec}^{min}$. Weber et al. have measured the longitudinal momentum distribution of He^{1+} ions from 100 to 250 keV/u p impact. Their results (Fig. 38) clearly show the predicted sudden onset of the cross-section at the kinematical threshold. Ions from capture reactions smoothly continue

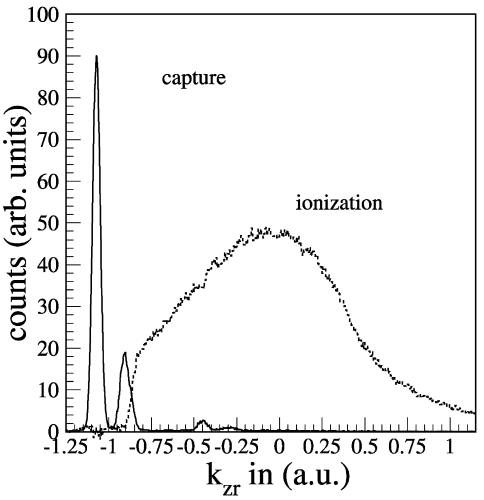

Fig. 38. Longitudinal momentum distribution of He^{1+} ion from 150 keV/u p impact on He. The full line with the peaks corresponds to capture to ground state, excited states and capture plus target excitation. The dashed line results from ionization (from [84]).

the $k_{||\mathrm{rec}}$ distribution from ionization in this intermediate velocity range where capture and ionization have comparable cross-sections.

4.2. Multiple electron processes in fast collisions

In this section we first discuss processes involving two active target electrons (double ionization, transfer ionization and double capture), then reactions involving one electron of the target and one of the projectile and finally multiple electron processes leading to highly charged recoil ions.

4.2.1. Double ionization of He

Most of the studies of double ionization of He by charged particle impact are devoted to ratios $R_z = \sigma^{2+}/\sigma^{+}$ of the total cross-sections only. From the dependence of R_z on the strength of the perturbation $q^2/v_{\mathrm{pro}}^2 \ln v_{\mathrm{pro}}$ it was established that in the limit of small perturbations an asymptotic ratio of $R = 0.26\%$ is approached, independent of the projectile charge and mass (see, e.g. [176,177] for a recent review). For stronger perturbation R_z increases which has been attributed to a two-step process of two independent interactions of the projectile with the two electrons [177].

Pioneering multiple differential cross-sections for He double ionization by 0.3 MeV proton impact have been reported by Skogvall and Schiwietz [178]. They measured angle and energy resolved electron emission cross-sections for close impact parameters and found strong deviations from predictions of the independent-particle model. The first recoil ion momentum studies for double ionization of He determined the transverse recoil ion energy as a function of the projectile scattering angle experimentally as well as theoretically within the dCTMC approach [58,98]. The results differ from those obtained for single ionization (discussed in detail in Section 4.1.2.2) in two ways: For very small scattering angles (< 0.25 mrad) the recoil ion energy is higher than for single ionization. This effect could qualitatively be reproduced by dCMTC calculations including

a dynamical screening for the second electron [58,98]. Second, the region where the transverse recoil ion momenta are much smaller than the projectile transverse momenta extends to larger projectile scattering angles as for single ionization. The latter is caused by the fact that in the two-step process the projectile is scattered sequentially at two electrons. Thus, while for single ionization the maximum scattering angle at an electron at rest is 0.55 mrad, twice this value can be reached for double ionization. This simple fact solves a puzzle originating from single differential measurements of Giese and Horsdal [151,152,179,180]. They have measured R_z as a function of projectile scattering angle for 0.3–1 MeV p–He collisions and found a distinct peak at a scattering angle of about 0.9 mrad. Taking into account the dynamics of the projectile scattering, this can be interpreted as a manifestation of the double scattering mechanism in the double ionization process. While for single ionization close impact parameter collisions with the nucleus are required to reach a scattering angle of 0.9 mrad, the two-step process for double ionization contributes to all scattering angles up to 1.1 mrad. This explanation has been supported by nCTMC calculations [154,58,52] and has been confirmed by the measurements of the recoil ion energies of the He^{2+} ions [58,181,98] and by quantum mechanical calculations [182], too.

The transverse momentum distribution of He^{2+} recoil ions has been determined for fast p [98], C^{5+} [183] and Xe^{44+} projectiles [184,185]. They all show much larger transverse momenta for double ionization than for single ionization indicating closer impact parameters (see Fig. 39). This can be expected from an independent particle model. Unfortunately, no quantum mechanical calculations are available for comparison, since the problem of coupling two electron momenta and the nuclear momentum exchange has not yet been solved. The only quantum mechanical approach which incorporates the electron–electron interaction in the ground state and during the collision (forced impulse methode FIM [179,186–190]) uses the impact-parameter approximation and thus does not provide differential cross-sections.

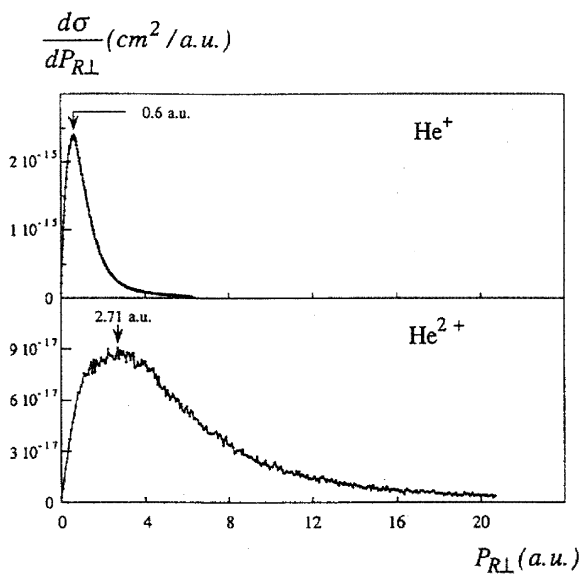

Fig. 39. Transverse momentum distribution of He^{1+} and He^{2+} ions from 6.7 MeV/u Xe^{44+} ion impact (from [185]).

Recently, Moshammer and coworkers succeeded in determining the first fully differential cross-section for He double ionization by charged particle impact. They measured the momenta of both emitted electrons in coincidence with the recoil ion momentum for 3.6 MeV/u Se^{28+}–He collisions. For this collision system double ionization is completely due to the two-step process ($R_z = 15\%$). In addition, the projectile velocity is fast enough, that the energy loss of the projectile, given by the sum of both electron energies and their binding energy results in a projectile momentum change $\Delta k_{\|\mathrm{pro}} = \Delta E/v_{\mathrm{pro}}$ which is very small compared to the electron and recoil momenta. As outlined in Section 4.1.2.3 the projectile acts as an extremely intense, short and broad band virtual photon pulse. Double ionization under these conditions would be dominated by coupling with two virtual photons. This interpretation within the Weizsäcker-Williams formulation is supported by a theoretical study by Keller and coworkers [169]. Fig. 40 shows the longitudinal momenta of two electrons for double ionization of He and double and triple ionization of Ne. The distribution is strongly forward shifted as a result of the long-range Coulomb

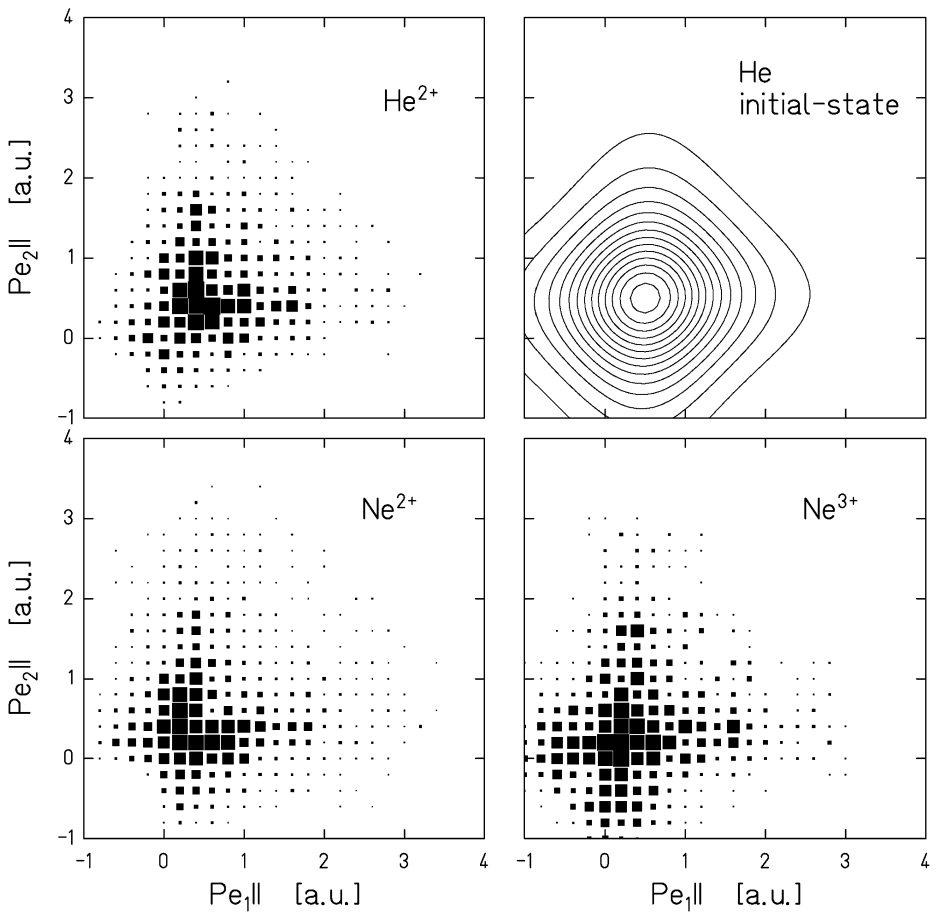

Fig. 40. Longitudinal momentum of two electrons ($k_{\|e1}$ vs. $k_{\|e2}$) for 3.6 MeV/u Se^{28+} on He and Ne double and triple ionization. The upper right figure shows for comparison the correlated He initial state (from [79]).

potential of the emerging ejectile. More interestingly, the momenta of the two electrons are found to be strongly correlated. Such patterns cannot be explained by any independent particle model or, more precisely, in the absence of the explicit $1/r_{12}$-interaction between the two electrons. In CTMC calculations the experimentally observed pattern is partially reproduced only if the $1/r_{12}$ potential is included. The basic features of the measured distributions are already present in the correlated He ground state wave function (see Fig. 40). At GSI these experiments have been continued to much higher impact velocities like 1 GeV/u [81], where the classical revolution time of the electrons in the ground state is below 1% of the collision time. Thus, one can hope to achieve a 'snapshot' of the correlated initial-state wave function of atoms, molecules or clusters which are multiply ionized in such reactions [191]. For a relativistic *n*CTMC calculation at this energy see [167].

4.2.2. Transfer ionization

As for double ionization, one might distinguish different mechanisms for transfer ionization (TI), i.e. the simultaneous capture of one target electron and emission of a second one. Within an independent-electron approximation, TI is a result of one step where a target electron is captured, and a second step where by a projectile–electron interaction the second electron is emitted to the continuum (TSTI). If one takes the electron–electron correlation in the initial ground state into account, two new mechanisms are present in theoretical models: shake-off [177] and shake-over [192]. In the first case one electron is captured and the second one is emitted due to the change of the effective target potential after the loss of the first electron. In the case of shake-over [192] the first electron is emitted by a projectile electron interaction and the second one is captured by a relaxation of the target wave function partly to bound projectile states. Finally, if one takes not only the static initial-state correlation into account, but also allows for a dynamic electron–electron correlation during the collision, a fourth mechanism (eeTI) becomes possible. This process of (eeTI) has already been proposed on grounds of classical mechanics by Thomas in 1927 [193]. Assuming the electrons at rest for simplicity, the projectile knocks the first electron to a angle of 45° to the beam axis with the velocity $\sqrt{2} \times v_{\mathrm{pro}}$. In a second step with some probability this electron scatters from the second electron into the forward direction with velocity v_{pro} where it can be captured by the projectile ion. In this case the other electron is emitted perpendicular to the beam with an identical velocity v_{pro}. This momentum exchange leads to a scattering angle of 0.55 mrad for a proton, independent of the projectile energy. In a pioneering experiment Palinkas and coworkers identified the electrons from this process experimentally [194]. Horsdal and coworkers [195] searched for the (eeTi) in the scattering angle dependence of the TI process (see [182,196,197] for an explanation of the experimental findings of [195] a TSTI). Quantum mechanical calculations of the eeTI process in second Born approximation have been reported in [198–200].

Multiple differential cross-sections measurable by COLTRIMS allow for a detailed examination of these mechanisms. The determination of the longitudinal momentum distribution alone allows for some qualitative conclusions already. Such experiments have been reported by Wu and coworkers [88] and Kambara and coworkers [133] (a). The first kinematical complete experiment for transfer ionization has been reported by Mergel and coworkers [68,69]. They measured the projectile momenta in coincidence with the recoil momentum vector for *p*–He collisions and obtained complete images of the square of the correlated three body wave function in the final state.

This experiment allows for the first time a detailed and quantitative analysis of the two-step and the Thomas double-scattering mechanism (b).

(a) Wu and coworkers have measured the longitudinal momentum distributions for single target ionization, single electron capture (Fig. 21) and transfer ionization for 20–60 MeV MeV O^{7+} and F^{8+} impact on He with a resolution of 0.75 a.u. [88]. For single ionization they found the distribution centered around $k_{\|\mathrm{rec}} = 0$ with the width of approximately the Compton profile in agreement with the findings for fast p impact reported in Section 4.1.2.2. To test the assumption of a two-step process within the independent-electron approach, they calculated the impact parameter dependence for single ionization and single capture and found that the ionization probability is constant and approaches unity in the range of impact parameters where single capture is significant. Thus, within the simplest version of the independent-electron model the $k_{\|\mathrm{rec}}$-distribution for transfer ionization is given by the distribution for single capture, folded with the one for single ionization. Fig. 41 shows the measured distribution for transfer ionization together with the results of this independent electron model. Very good agreement is observed.

At a much lower impact energy of 8.7 MeV Kambara and coworkers performed the equivalent experiment [133]. They found, that the distribution for transfer ionization is slightly backward shifted compared to the single capture distribution. They concluded that while single capture leads to final states $n = 4$ and higher TI leads mainly to $n = 2 - 3$. This can be understood qualitatively

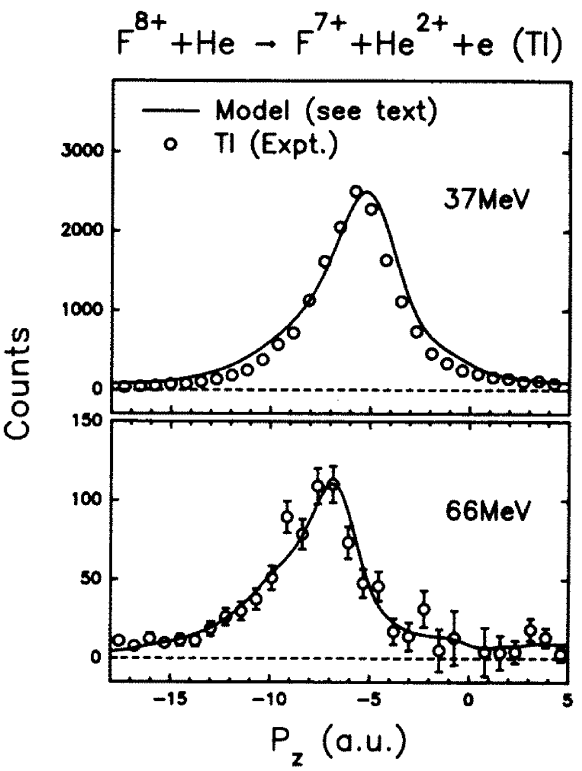

Fig. 41. Recoil ion longitudinal momentum distribution for $F^{8+} + He \rightarrow F^{7+} + He^{2+} + e^{-}$. The full line shows results from the independent electron model (from [88]).

in a refined two-step model [201]. In a two step process it is most likely that ionization is the first step due to the lower ionization potential for the first electron. In this case the second step would be a capture from a He^{1+} ion, which may lead to more tightly bound final states as observed in the experiment.

(b) A kinematically complete experiment for the reaction

$$0.3 - 1.4\,\mathrm{MeV}\ p + \mathrm{He} \rightarrow \mathrm{H} + \mathrm{He}^{2+} + e^{-} \tag{23}$$

has been reported by Mergel et al. [68,69]. They have measured the three momentum components of the recoiling ion in coincidence with the two momentum components of the scattered hydrogen atom perpendicular to the beam. Since there are three particles in the final state and it is known that the capture leads predominately to the ground state, the measurement of 5 momentum components together with momentum and energy conservation provides the complete kinematic information on the process. Thus, even if the electron is not directly measured its momentum can be calculated from the measured quantities. The momentum space of the recoiling He^{2+} ion gives a simple criterion to distinguish the (eeTI) from all the other processes (TSTI, Shake-off, Shake-over). The Thomas mechanism for transfer ionization (eeTI) does not require the nucleus to balance the momentum. In this process the forward momentum of the captured electron is compensated by the second electron. The target nucleus acts only as a spectator. All other TI processes involve one step where one target electron is kinematically captured by the projectile and therefore the target nucleus has to compensate the electron forward momentum yielding a backward momentum transfer of $-v_{\mathrm{pro}}/2 - Q/v_{\mathrm{pro}}$ to the recoil ion. In addition the (eeTI) leads to a scattering angle of 0.55 mrad for the projectile.

Fig. 42 shows the momentum distribution of the He^{2+} recoil ions for projectile polar scattering angles between 0.45–0.65 mrad. The plane shown is defined by the beam axis (z direction, vertical) and the momentum vector of the scattered projectile. The projectile is scattered towards positive k_x. The data are integrated over the recoil ion momenta in the k_y direction. Contributions from the TSTI process are expected along the (dashed) line of $k_z = -v_{\mathrm{pro}}/2 - Q/v_{\mathrm{pro}}$. While at 0.5 MeV this is by far the dominant process, at 1 MeV impact energy clearly a second peak from the (eeTI) arises. At 1.4 MeV this correlated Thomas capture already is the dominant contribution at the critical projectile polar scattering angle. This interpretation was further supported by nCTMC calculations. In these calculations the electron–electron interaction can be switched on and off. They showed that the peak at momentum zero only arises if the electron–electron interaction is taken into account on during the collision. They do, however, not yield the correct cross-section.

Mergel and coworkers also obtained the total cross-sections for the contribution of the (eeTI) from the data shown in Fig. 42. They found a scaling of the cross-section with $v_{\mathrm{pro}}^{-7.4\pm1}$ where v_{pro} is the projectile velocity. This is in striking contradiction to the predictions of the classical Thomas model and second-order Born calculations. Both theories predict the same scaling like v_{pro}^{-11} at asymptotically high velocities. At 1.4 MeV the experimental cross-section is already a factor of 10 larger than predicted by theory.

The process of (eeTI) is a unique probe of initial-state correlation in the helium atom. First, the cross-section for this process directly reflects the spatial distance between the two electrons and, thus, is sensitive to the correlation in coordinate space. Second, the momentum distribution of the left behind He^{2+} nucleus reflects the sum momentum of both electrons in the initial state and, hence, the correlation in momentum space. The (eeTI) at high velocities acts as a very fast knife

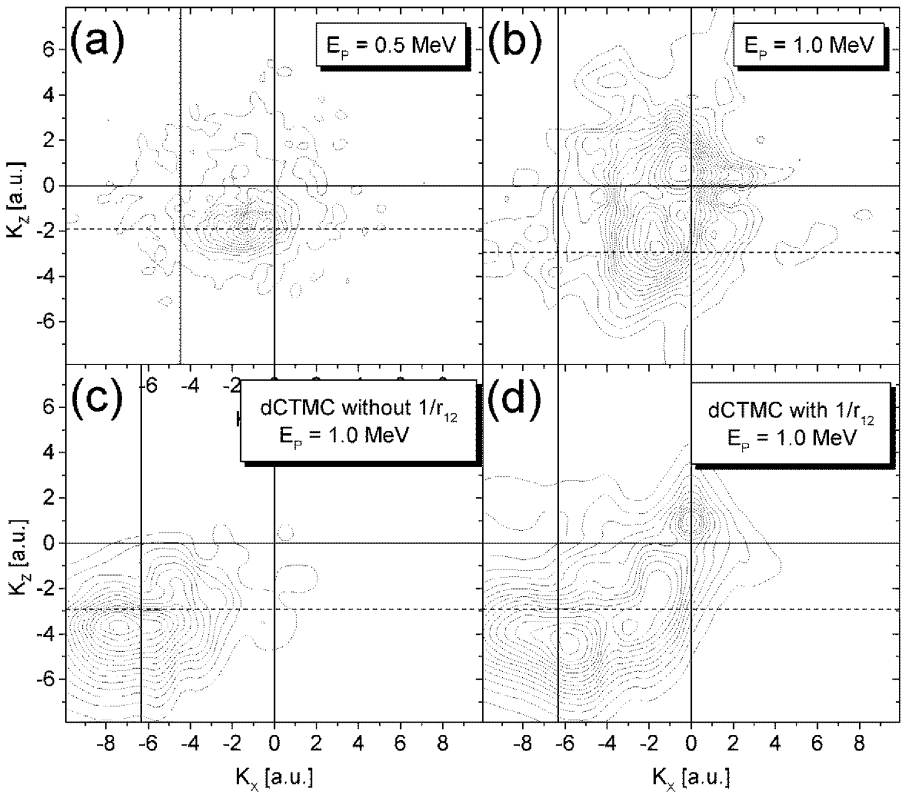

Fig. 42. Momentum distribution of recoil ions for the reaction $p + \mathrm{He} \rightarrow \mathrm{H} + \mathrm{He}^{2+} + e^{-}$. The plane is defined by the incoming beam (z direction) and the momentum vector of the scattered projectile (toward positive k_x). All distributions are for a fixed scattering angle of 0.45–0.65 mrad of the projectile and are integrated over the recoil ion momentum in y direction. The dashed lines show the longitudinal momentum where events from two-step processes and shake-off processes are expected. The (eeTI) Thomas process is expected close to the origin (from [69]).

which cuts almost instantaneously the bond between the three particles in the He atom. It minimizes all kind of post collision interactions which smear out the signature of the initial state in the final state.

The fully differential cross-sections can be transformed to emission patterns for the electron. For 0.3 MeV it was demonstrated this way that the scattering of the projectile in the region of the critical scattering angle is mainly caused by a hard binary collision with the emitted electron. This is the analog to the findings for single ionization reported in Section 4.1.2.2. It explains the sharp peak found in the ratio between transfer ionization to single capture cross-sections at 0.55 mrad by Horsdal and coworkers [195]. This peak is caused by binary-encounter scattering of the projectile at the emitted target electrons, similar to the peak at 0.9 mrad in the ratio of double to single ionization [151] discussed in Section 4.2.1.

A puzzling new feature in the electron emission is found for the small scattering angles (< 0.3 mrad). At these angles the electrons are found to be emitted backward. No conclusive interpretation has been given for this unusual emission pattern. It has been speculated [68] that it

may be a result of the initial state correlation, since for capture a forward directed momentum component of the electron in the initial state is needed. In this case the left-over second electron maybe backward directed.

4.2.3. Electron–electron interaction in electron-loss reactions

In all processes discussed so far only electrons from the target have been involved. A new and even more complex situation arises if projectile electrons are actively involved in the collision. For this case where a projectile electron is emitted two mechanisms have been discussed in the literature. The projectile electron can either be emitted by an interaction with the target nucleus (*ne*) or with one of the target electrons (*ee*) [202–211]. With the use of COLTRIMS a break through in this investigations has been achieved since the measurement of the recoil ion momentum allows an experimental separation of the two mechanisms [66,88,89,212]. The explanation for this is similar to the case of transfer ionization discussed in Section 4.2.2. For the (*ne*) mechanism the target nucleus must be actively involved in the collision receiving large forward and transverse momenta, while for the (*ee*) mechanism, the target nucleus acts as a spectator, receiving only little momentum transfer. The longitudinal momentum balance for these reactions can be seen in more details from Eqs. (6) and (7). The loss of kinetic energy of the projectile necessary for ionization corresponds to backward momentum transfer to the projectile. This projectile longitudinal momentum loss has to be compensated by the target atom. If now the target is ionized, the forward momentum can be either transferred to the recoiling ion, which occurs in the case of an (*ne*) interaction, or to the emitted target electron, which occurs in the case of an (*ee*) interaction. Thus, measuring $k_{\parallel \mathrm{rec}}$ allows the separation of the two mechanisms. In both cases the recoil ion momentum is smeared out by the momentum transfer caused by the target ionization. In addition to the difference in $k_{\parallel \mathrm{rec}}$ one expects larger $k_{\perp \mathrm{rec}}$ for the (*ne*) than for the (*ee*) mechanism, since for the (*ne*) mechanism the impact parameter between the nuclei needs to be in the range of the projectile electron shell radius [206,207,209,210] and thus smaller than for the (*ee*) process.

Fig. 43 shows the momentum distribution of the recoiling ions for the reaction

$$0.5 - 2\,\mathrm{MeV}\ \mathrm{He}^{1+} + \mathrm{He} \rightarrow \mathrm{He}^{2+} + \mathrm{He}^{1+} + 2e^{-} \tag{24}$$

from Ref. [66]. The two maxima at 1 MeV can be attributed to the contribution of the (*ee*) interaction (close to the origin) and the (*ne*) mechanism (forward shifted). The long dashed line shows the position where one expects the contributions of the (*ne*) according to Eq. (7). In addition Fig. 43(f) shows the He^{1+} momentum distribution resulting from electron-impact ionization at velocity equal to 1 MeV He impact. The maximum nicely coincides with the (*ee*) contribution in (c) illustrating the analogy of the (*ee*) mechanism with electron-impact ionization. The threshold for electron impact ionization of He^{1+} is at a velocity equivalent to 0.4 MeV, thus the contribution of the (*ee*) mechanism disappears at the lowest energy investigated. For increasing energies the (*ee*) mechanism is dominating, since it involves only one interaction while the (*ne*) requires one interaction from target–nucleus and projectile–electron as well as an additional interaction from projectile–nucleus and target–electron. The experimental momentum distributions as well as the absolute cross-sections are very well described by two-center *n*CTMC calculations (see Refs. [66,212] for a detailed comparison). At the lowest energies investigated here these calculations predict a third mechanism which is a double target ionization followed by a capture of the

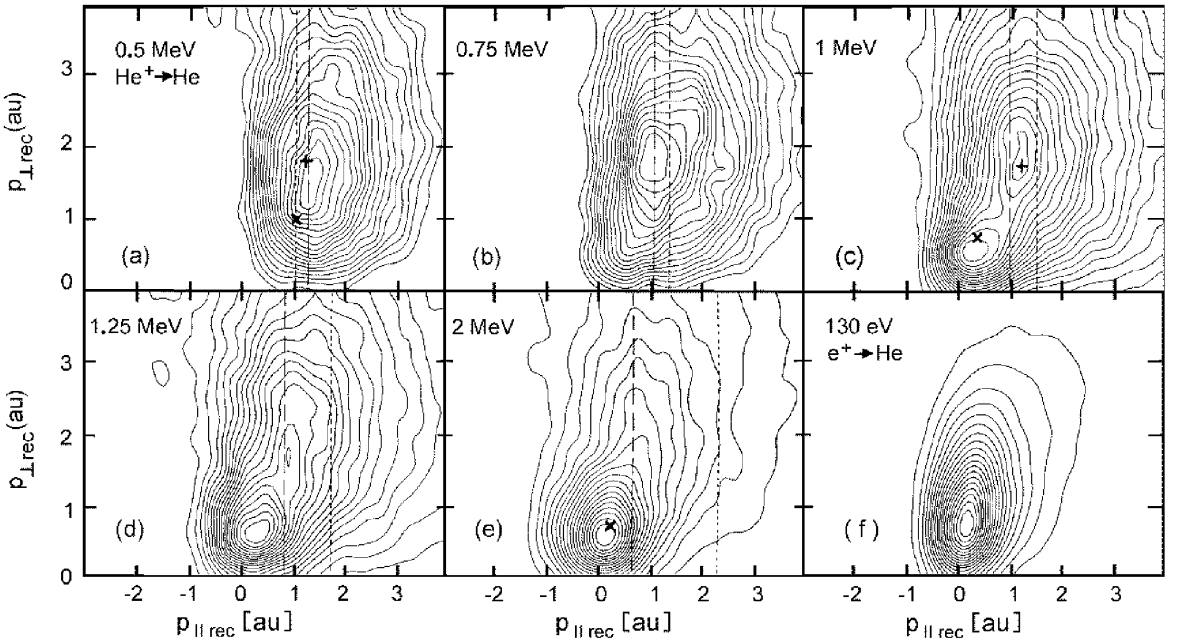

Fig. 43. (a–e) Momentum distributions of recoil ions for the reaction (24) for variable impact energy. The vertical axis shows the recoil ion transverse momentum, the horizontal axis the longitudinal momentum. The contour lines are linear and equally spaced in cross-section. The two maxima for 1 MeV impact result from the (*ee*) and (*ne*) interaction, respectively. The long dashed line indicates the position of expected longitudinal momentum for the (*ne*) contribution from Eq. (7). (f) Momentum distribution of He^{1+} ions from 130 eV electron impact, which is equivalent in velocity to 1 MeV He (from [66]).

projectile electron to the target. The expected $k_{\|\mathrm{rec}}$ for this three-step mechanism (see Eqs. (6) and (7)) is shown by the short dashed line in Fig. 43.

For highly charged ion impact the separation of the (*ee*) and (*ne*) mechanism in the longitudinal momentum increases because of the larger binding energy of the projectile electrons and it becomes possible to determine quantitatively the individual cross-sections for both mechanisms. Wu and coworkers have investigated O^{7+} on He collisions and extracted the ratio of (*ee*) and (*ne*) contributions (see Fig. 44). They found very good agreement with a simple model using a scaled Plane-Wave-Born cross-section for the (*ne*) mechanism and folding a free-electron impact ionization cross-section with the Compton profile of the target (for a more detailed discussion see also [88]).

4.2.4. Double electron capture

Capture of both electrons in He^{2+} on He collisions is one of the fundamental two electron processes. Ground state capture (resonant) is expected to be by far the dominant channel [213] for this reaction. This transition however cannot be accessed by energy gain spectroscopy or coincident detection of photons or Auger [214] electrons [215], since the ejectile is neutral and in the ground state. Thus, COLTRIMS is the only experimental approach allowing to separate this dominant channel. Dörner and coworkers [111] found a ratio of about $16 \pm 3\%$ for double

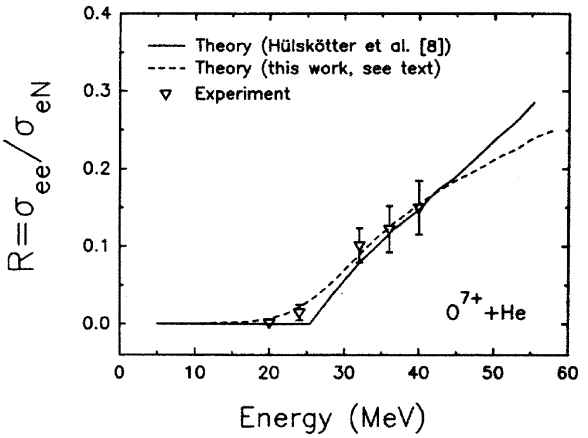

Fig. 44. Ratio of cross-sections for the (*ee*) and (*ne*) contribution to simultaneous target and projectile ionization for O^{7+} – He collisions, as function of impact energy. Triangles: Experimental data obtained from integrating over the respective range of recoil ion momenta for each process, solid line: Theoretical calculation from [243,244], dashed line theoretical estimate from [89], see text (from [87]).

capture to nonautoionizing exited states to ground state capture for double capture by 0.25–0.75 MeV He^{2+} impact on He, by measuring the $k_{\|\mathrm{rec}}$ distribution of the He^{2+} ions. This is in good agreement with *n*CTMC predictions by Tökesi and Hock [216]. Much theoretical effort has been put into the calculation of total as well as scattering angle differential double capture cross-sections (see, for example [201,217–233]). Most of those calculation depend to some degree on treating the two electrons independently during the collision. Only recently new approaches have been developed which preserve the full 4-body nature of the problem [213,234–239]. Effects of dynamical electron–electron correlation during the collision can be most sensitively probed in differential cross-sections. From the scattering angle dependence of single capture at fast collisions it is well known, that the transverse momentum exchange up to 3 a.u. is mostly mediated through the captured electron [240,241]. Thus, the correlated electronic momenta should be reflected in the differential double capture cross-sections (see [242] for a first experiment). State-selective differential cross-sections at 0.25 MeV He^{2+} impact energy obtained by COLTRIMS (Fig. 45) show that capture to excited states results in larger transverse momentum exchange between projectile and target than ground state double capture. This indicates the necessity of smaller impact parameters for exothermic channels. For higher impact energies significant structure in the differential cross-section resulting from three different Thomas type scattering mechanism have been predicted [221,245]. COLTRIMS experiments searching for such structures are under way.

4.2.5. Multiple ionization and capture

As for single ionization, the longitudinal and transverse momentum transfers are completely decoupled for multi-electron processes induced by fast ion impact. Contrary to single ionization, however, in multiple electron processes the transverse momenta are often much larger than the longitudinal momenta, since many electron processes require closer impact parameters. The first experiments concentrated on this transverse momentum exchange, aiming for determination of the impact parameter dependence of the reactions. Historically, the data were often presented in terms

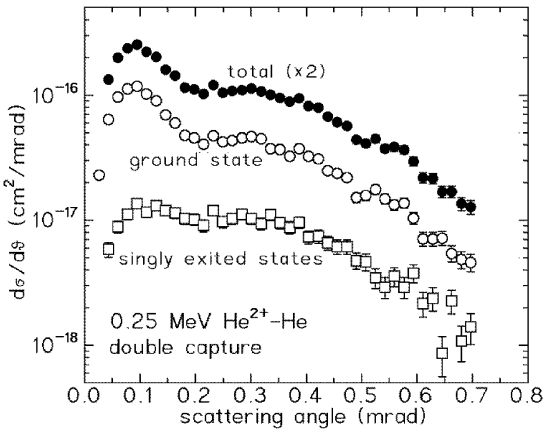

Fig. 45. Scattering angle distributions for double electron capture for 0.25 MeV He^{2+} on He collisions obtained by measuring the transverse recoil ion momentum. Full circles: All final states (data multiplied by 2). Open circles: Ground-state capture. Open squares: Double capture to nonautoionizing excited states (from [111]).

of mean energies of the recoil ions for different reaction channels [46,49,62,99,246–248] partly to get information on the ionization mechanism and partly because of the practical relevance of the recoil ion energies for the brightness and energy spread of heavy-ion beam pumped secondary ion sources [42,249,250]. The general trend for all collision systems is a steeply increasing recoil ion energy with increasing ion charge state. One typical example of such data is shown in Fig. 46. The experiment was performed using an extended gas target at room temperature and the data are thus influenced by the target thermal motion at the lower energies.

For a detailed comparison with model predictions it is, however, more informative to discuss these data in terms of cross-sections singly differential in $k_{\perp\mathrm{rec}}$. We first discuss the results of the pioneering experiments on $k_{\perp\mathrm{rec}}$ distributions by Ullrich and coworkers for fast U^{32+} and U^{65+} impact on Ne and Ar. Second, we discuss results for the collision system $F^{7+,8+,9+}$ on Ne, for which different groups investigated the transverse momentum balance between projectile, recoil ion and emitted electrons [60–62,99]. All of these studies had low resolution in the recoil ion momentum. Finally, experiments on the longitudinal momentum balance for multi-electron processes involving capture and ionization by three different groups [62,82,99,185] are reviewed.

4.2.6. Transverse momentum transfer in fast multiply ionizing collisions

Ullrich and coworkers have performed the first experiments to measure the transverse momentum distribution of Ne and Ar recoil ions created by fast U^{32+} and U^{65+} [50]. These experiments have been performed using a field-free gas cell at room temperature. It allowed them to access for the first time the transverse momentum exchange in a fast heavy ion collision on the level of accuracy equivalent to scattering angles of 10^{-6} rad.

Fig. 47 shows the recoil ion transverse momentum distributions for 1.4 MeV/u U^{32+} and 5.9 MeV/u U^{65+} on Ne impact summed over all charge states of the ions. At large transverse momentum exchange the differential cross-sections are well described by the Rutherford cross-section (i.e. they decrease with $1/k^3_{\perp\mathrm{rec}}$). At small momenta the data deviate significantly from

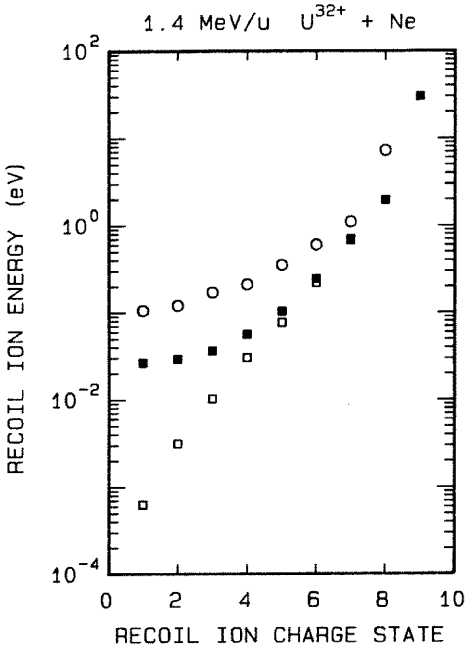

Fig. 46. Mean transverse recoil ion energy as a function of recoil ion charge state for 1.4 MeV U^{32+}–Ne collisions. Open circles: Experiment. Open squares: *n*CTMC. Full squares: *n*CTMC folded with target thermal motion (from [42]).

a Rutherford distribution folded with the thermal motion of the target. *n*CMTC calculations show that the momenta of the emitted electrons dominate the transverse momentum exchange in this regime. The calculations indicated that the projectile will even be scattered to negative scattering angles for impact parameters greater than 3 a.u. at the attractive negative potential of the strongly polarized electron cloud. This first evidence of the strong influence of the emitted electrons on the heavy-particle motion was confirmed by the latest high-resolution studies using supersonic gas-jet targets (for single ionization see Section 4.1.2.3 and Refs. [76,79,121]).

While Fig. 47 displays $d\sigma/dk_{\perp rec}$ summed over all ionic charge states, cross-sections differential in the recoil ion charge state have been obtained simultaneously. These differential cross-sections for multiple ionization can either be used directly for a detailed test of theoretical models which calculate the momentum exchange like the *n*CTMC [159], or they can be used to obtain ionization probabilities. Since the total scattering follows a Rutherford-like shape at larger transverse momentum transfers one can obtain probabilities for each charge state as a function of $k_{\perp rec}$, which is at these large $k_{\perp rec}$ related to the impact parameter. Horbatsch and coworkers [251,252] have found that these probabilities can be described in a consistent way by an independent electron model calculating single particle ionization probabilities and neglecting all electron–electron correlation effects.

For fast (0.5–1 MeV/u) $F^{7-9+} \rightarrow$ Ne collisions different groups have reported differential cross-sections for ionization, single and double capture and the emission of up to 6 electrons to the continuum. In these studies the recoil ion transverse momentum and charge state has been

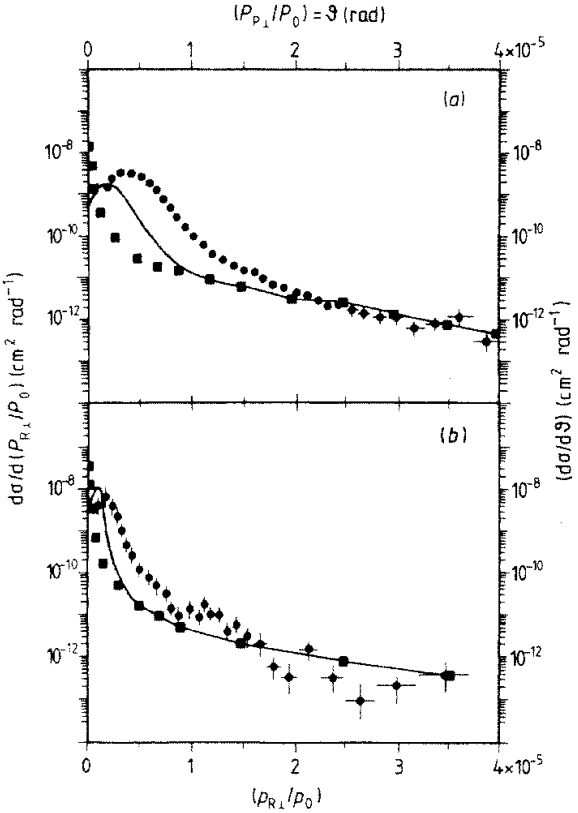

Fig. 47. Recoil ion transverse momentum distributions for (a) 1.4 MeV/u U^{32+} and (b) 5.9 MeV/u U^{65+} impact on Ne, summed over all recoil ion and projectile charge states. Full circles: experiment; open squares: *n*CTMC; full line: *n*CTMC folded with thermal momentum distribution at room temperature (from [50]).

measured in coincidence with the projectile scattering angle and charge state [60–62,99]. One of the goals of these experiments was to obtain information on the sum momentum of the emitted electrons from the difference between projectile and recoil ion momenta. Within the experimental resolution of the projectile momentum measurement of about 20–40 a.u. (which is worse than the $k_{\perp\mathrm{rec}}$ measurement) all the experiments agreed that no deviation is found from a two-body scattering between projectile and target nucleus. Thus, on this scale even the sum momentum of 6 emitted electrons plays no essential role on the transverse momentum balance. This refutes the findings of Gonzales and coworkers [253], who reported a strong 'out-of-plane' scattering of projectile and target nucleus caused by very high electron momenta. In general, increasing transverse momenta of projectile and recoil ion are found with increasing number of emitted electrons, indicating smaller impact parameters.

Unverzagt and coworkers reported on such data for 5.9 MeV/u U^{65+} on Ne collisions. They found excellent agreement between experiment and *n*CTMC calculations (see Fig. 48). Similar data for Xe^{44+} impact on Ar have been reported by Jardin and coworkers [185]. In both experiments also the longitudinal momenta of the ion have been measured (see next sections).

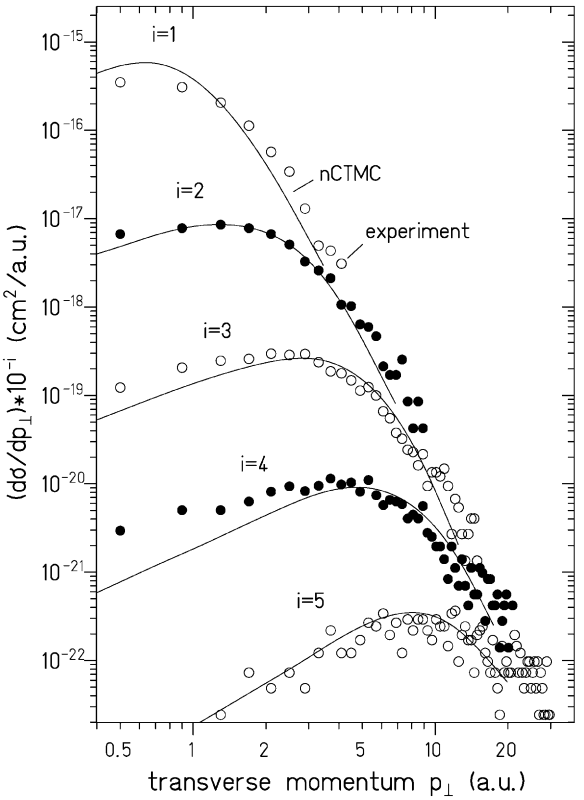

Fig. 48. Recoil ion transverse momentum distribution for 5.9 MeV/uU^{65+} + Ne → U^{65+} + Ne^{i+} + ie^- (from [82]).

4.2.7. Longitudinal momentum transfer for fast highly charged ion impact

The longitudinal momentum balance for multiple ionization has been investigated by Unverzagt and coworkers for 5.9 MeV/u U^{65+} on Ne and for Xe^{44+} on Ar collisions by Jardin and coworkers. Both groups found backward emission of the ions. The momentum position of the maxima as well as the widths of the distribution increase roughly linear with the ionic charge (see Fig. 49). The data are again in excellent agreement with *n*CTMC calculations.

No electron is captured in these collisions, thus the $k_{||\mathrm{rec}}$ is given by $k_{||\mathrm{rec}} = \Delta E_{\mathrm{pro}}/v_{\mathrm{pro}} - \sum k_{||e}$ (see Eqs. (4)–(7)). Where ΔE_{pro} is the energy loss of the projectile, i.e. the sum over the electron continuum energies, the binding energies and excitation energies of the residual ion. However, since $v_{\mathrm{pro}} \approx 16$ a.u. the ratio $\Delta E_{\mathrm{pro}}/v_{\mathrm{pro}}$ is in most cases small compared to the sum of the longitudinal electron momenta. Thus, the backward recoil ion momenta prove that the electrons are collectively forward emitted with a mean longitudinal sum energy of 5 eV for single ionization up to 1.1 keV for Ne^{6+}. This forward emission is not a trivial result of a binary-encounter between projectile and electron, since it has been shown in Section 2 that binary encounter electrons result in no momentum transfer to the ion. The forward emission of the electrons as well as the backward emission of the ions is a consequence of the strong long-range force of the highly charged projectile on the outgoing path of the trajectory similar to what has been observed for single ionization of He

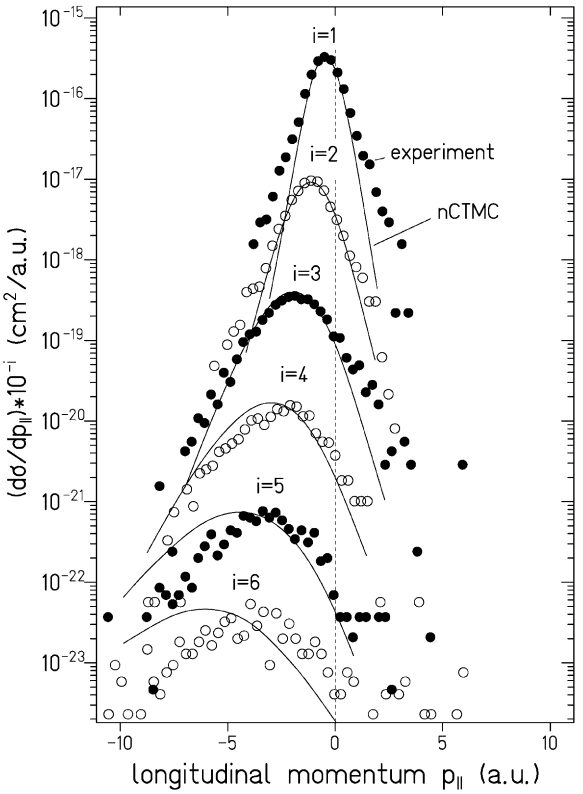

Fig. 49. Recoil ion longitudinal momentum distribution for 5.9 MeV/u $U^{65+} + Ne \rightarrow U^{65+} + Ne^{i+} + ie^-$ (from [82]).

(see Fig. 35). The same trend has been seen for double ionization of He [185]. Backward emission of highly charged Ne recoil ions by fast highly charged ion impact has first been seen in an experiment by Gonzales-Lepra and coworkers [48].

For multiple ionization involving additionally the capture of 1–3 electrons Frohne and coworkers observed an unexpected opposite trend. They investigated 19 MeV F^{9+} Ne collisions determining the number of captured (0–3) and continuum electrons (0–5). Using a warm effusive gas target the mean value of the longitudinal momentum of the recoil ion was measured. Within their resolution they found the distribution centered around zero for the pure ionization channel and up to 5 electrons emitted to the continuum. For capture of n electrons and no emission to the continuum they saw backward emission following the $(n \times v_{pro}/2)$ law as expected from Eq. (5). However, for capture accompanied by emission of m electrons to the continuum they observed increasing forward recoil ion momenta compared to the pure capture channels (see Fig. 50). This is opposite to the prediction of the *n*CTMC calculations and from what one would expect from the effect of post collision interaction. As discussed in Section 4.2.2 Mergel and coworkers [69] have even found mainly backward scattered electrons for transfer Ionization in fast proton on He collisions. No conclusive interpretation of this behaviour has been found.

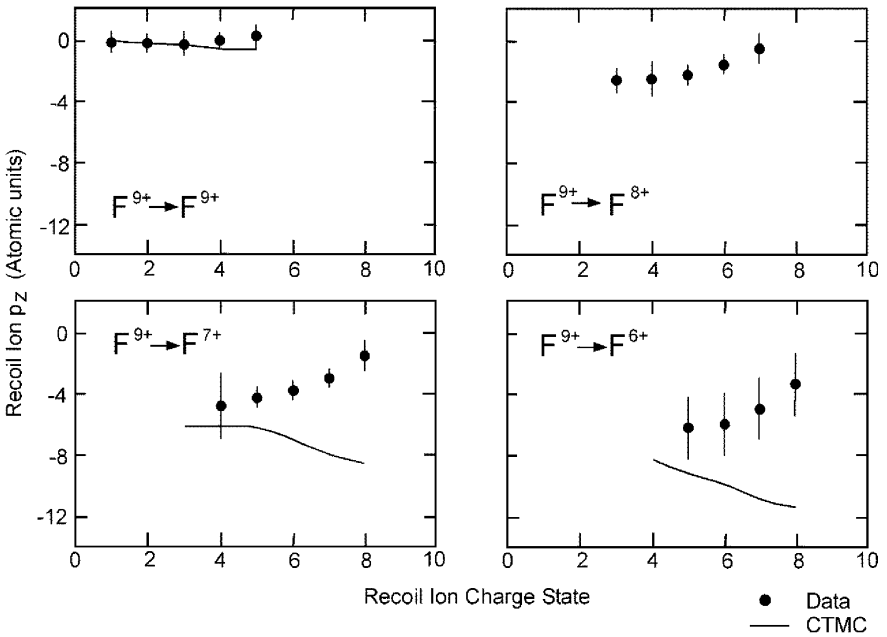

Fig. 50. Mean recoil ion longitudinal momentum as function of the ion charge state q for the reaction 19 MeV $F^{9+} + Ne \rightarrow F^{p+} + Ne^{q+} + (p + q - 9)e^-$. Full line: nCTMC (from [99]).

4.3. Multiple electron processes in slow collisions

Early experiments performed on many-electron transition, at slow impact velocities at Kansas State University have used a warm effusive gas-jet target. They were therefore not able to resolve the line structure in the $k_{||\mathrm{rec}}$ distribution but they did provide important information on the mean Q-value and on the transverse-momentum distribution.

Wu and coworkers performed systematic studies on transfer ionization and double capture reactions in $O^{7,8+}$ and N^{7+} on He collisions at 0.2–1.7 a.u. impact velocity. At these slow velocities direct ionization is negligible and, thus, transfer ionization proceeds via double capture followed by autoionization. The measurement of the Q-value, the ratio between transfer ionization and true double capture, along with the transverse momentum distributions allows one to obtain information on which states have been populated and whether the transfer of the electrons occurs in one or two steps. Significant differences between the O^{8+} projectile on one and the N^{7+} and O^{7+} on the other side have been observed. For O^{8+} the ion momentum distributions in $k_{||\mathrm{rec}}$ and $k_{\perp\mathrm{rec}}$ direction are similar for transfer ionization and double capture. The authors conclude that asymmetric states, i.e. states where the main quantum number of the two captured electrons is very different, are populated in both cases by a two-step process. In contrary for O^{7+} and N^{7+} the $k_{||\mathrm{rec}}$ and $k_{\perp\mathrm{rec}}$ distributions are different between double capture and transfer ionization (see Fig. 51). For double capture with successive autoionization the momenta are consistent with the capture channel to $(n, n') = (3,3)$ and (3,4) in a one step process. For double capture very asymmetric states $(2, > 10)$ are observed. From the scattering-angle dependence one can conclude that these states are

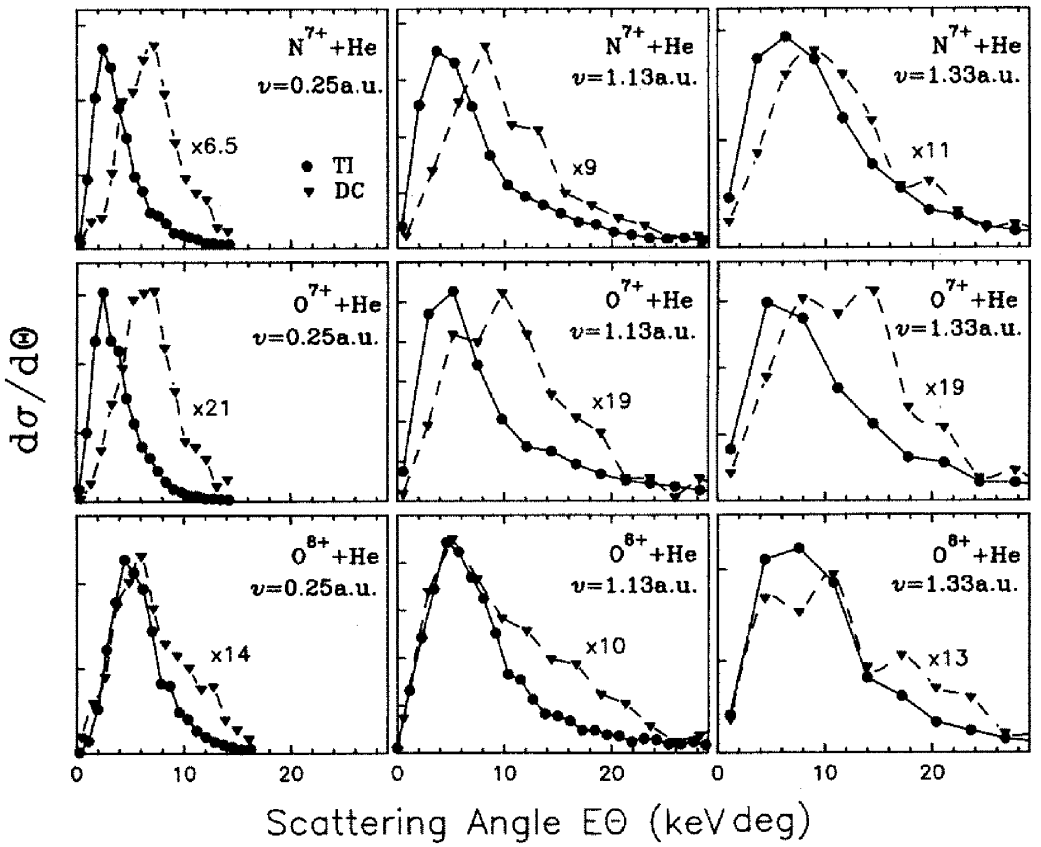

Fig. 51. Angular differential cross-sections for transfer ionization (filled circles) and double capture (filled triangles). The lines are drawn to connect the symbols. The projectile scattering angle has been measured via the transverse recoil ion momentum (from [100]).

populated via a capture plus excitation process which can be described within the independent electron model and a correlated double electron capture as discussed by Stolterfoht for O^{6+} impact [254] can be ruled out.

The first experiment where the longitudinal recoil ion momentum has been measured in order to determine the Q-value of the reaction has been performed by Ali and coworkers [63]. They investigated the capture of up to 5 electrons in 50 keV Ar^{15+} on Ar collisions. Up to now it is completely impossible to calculate the details of such a many-electron transition processes from first principles. However, a classical over-the-barrier model which has been extended and intensively applied by Niehaus (for a review see [255]) has proven to successfully predict cross-sections, impact-parameter dependences, and final-state distributions of such transitions. Since COLTRIMS provides the Q-value and the scattering angle dependence for all reaction channels it allows also for a sensitive test of this model. Ali and coworkers found very good agreement between experimental and predicted mean Q-values for the above collision systems. A later systematical study of multiple capture by slow highly charged ions using the recoil technique has been reported by Raphaelian and coworkers [256].

Abdallah and coworkers [257] have investigated single and double electron capture in Ar^{16+} on He collisions at velocities from 0.3 to 1.5 a.u. This study thus extends from the low velocity regime where energy matching between intial and final state are determine the main characteristics of the capture process into a transition region where velocity matching already becomes important. For single capture they find a widening of the reaction window (i.e. the energy range of states which are populated) with the square root of the projectile energy and a decreasing energy gain with increasing velocity. The scattering angles for a given Q-value is for the lowest velocity centered around half the coulomb angle ($\vartheta_c = Q/2E_{\mathrm{pro}}$ with E_{pro} being the projectile laboratory energy (see also [109]). This indicates an about equal probability of transfer on the way in and out. If the electron transfer occurs on the way in (out) scattering angles smaller (larger) than ϑ_c can be expected. At 1.5 a.u. velocity however the peak in the scattering angle distribution is shifted to significantly larger angles than ϑ_c.

The results for double capture at 1 a.u. are shown in Fig. 52. Fig. 52(a) shows the channel of true double capture (TDC), where both electrons are kept by the projectile, (b) is the channel of transfer ionization (TI). Here the capture to a doubly excited state has lead to autoionization. TI contributes about 70% to the total double capture cross-section. All double capture channels are found to peak at much larger scattering angles than ϑ_c. This shows that the double capture does not occur in a single transition in the crossing of the incident channel with the outgoing channel, but in a two steps of successive single transfers where at least one transition occurs on the way in.

4.4. Electron impact ionization

The field of electron impact ionization was one of the first in which kinematically complete experiments have been performed. For single ionization very successful and comprehensive work by many groups has been reported (for reviews see e.g. [9–11]). In these so called (e,2e) experiments the two outgoing electrons are detected in coincidence. With this technique recently even (e,3e) experiments have been done [12–18].

In this field also one of the first experiments measuring recoil ion momenta has been performed by McConkey and coworkers for electron impact on He and Ne. They used a gas cell at room temperature and detected the recoil ion through a rotatable slit with a mass spectrometer. With this apparatus they integrated over the ion momenta and measured the angular distribution. In (e,2e) experiments two maxima in the angular distribution of one electron for a fixed angle of the other electron are found at low momentum transfers. One maximum is related to a binary collision of the projectile and target electron and a second from a backscattering of one of the electrons at the target nucleus (recoil peak). McConkey et al. [43] could support this interpretation by measuring the angular distribution of the recoiling ion.

Recently, two experiments using COLTRIMS to investigate electron impact ionization have been reported. Dörner et al. [66] have measured the He^{1+} momentum distribution for 130 eV electron impact to compare it to the ionization by electrons which are bound to a projectile. This has been discussed in Section 4.2.3. Jagutzki and coworkers have explored the use of COLTRIMS for (e,3e)-experiments [64,105,258]. They measured the recoil ion momentum distributions for single and double ionization of He by 270–3200 eV electron impact. For single ionization by 500 eV electrons they found the recoil ion momentum distribution (integrated over all emission angles) to be very close to the momentum distribution of the slow emitted electron (see Fig. 53).

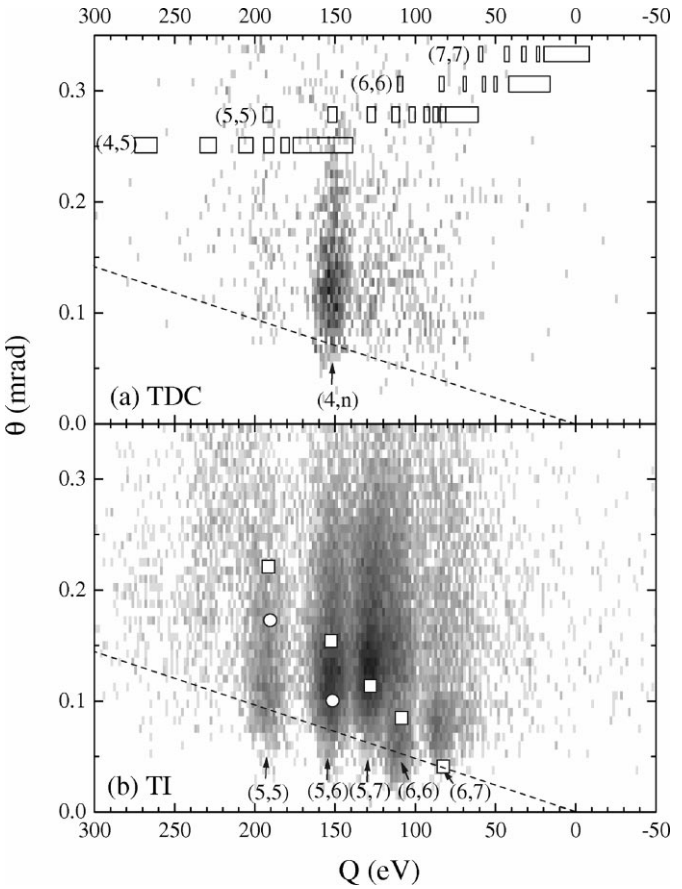

Fig. 52. Double electron capture in Ar^{16+} on He collisions at a projectile velocity of 1 a.u.. The horizontal axes shows the Q value of the collision, the vertical axis the projectile scattering angle. Both are measured via the momentum of the recoiling He^{2+} ion. (a) shows the true double capture channel, where both electrons are kept by the projectile. (b) shows the channel of transfer ionization, where the doubly excited projectile emits one electron by autoionization. The location of final states (n,n') are shown in the figure. The dashed line shows the location of $\vartheta_c = Q/2E_{\mathrm{pro}}$ assuming a one step transition (see the text). The open circles and squares indicate the deflection angles calculated assuming a two step transition with $n = 7$ and $n = 6$, respectively, as the enabling first step single capture transition (from [257]).

This is consistent with the findings of numerous (*e*,2*e*)-experiments that these collisions are dominated by small momentum transfer from the fast projectile. The momentum distribution is very close to the Compton profile of the initial state, similar to the case of fast proton impact (see Section 4.1.2.2). For double ionization the He^{2+} momentum distribution is found to be broader by about a factor of 2–3. The two-dimensional momentum distribution ($k_{\perp\mathrm{rec}}$ versus $k_{||\mathrm{rec}}$) shows a ridge along the kinematic line for a two-body collision of the projectile with the target nucleus. Thus, the He^{2+} momentum distribution is significantly forward shifted compared to the He^{1+} ions. The distribution along the kinematic line indicates that double ionization is dominated by much closer impact parameters (between projectile and target nucleus) than single ionization. *n*CTMC calculation yield good agreement for the momentum distribution of the He^{1+} ions but does not

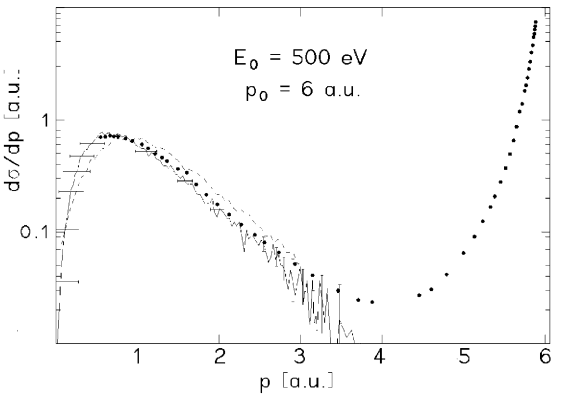

Fig. 53. Recoil ion momentum distribution (integrated over emission angle) for single ionization of He by 500 eV electrons. Line: Experiment. Dashed line: *n*CTMC calculation (scaled by 2.9). The dots show the electron momentum distribution calculated from (*e*,2*e*)-data [259,260] (from [105]).

find the ridge along the kinematic line for double ionization. One reason may be that the *n*CTMC does not include the shake-off and the interception process for double ionization.

Complete (*e*,3*e*)-experiments require either the coincident detection of all three electrons [12–18] or the coincident detection of two electrons in addition to the recoiling ion. Such experiments are under way [138,139,17],

5. Experimental results for photon impact

The latest field to which COLTRIMS has been applied are studies on photon-induced ionization. So far experiments on He and D_2 targets in the energy range from the double ionization threshold (79 eV for Helium) to 90 keV have been reported. The work covers measurements of the ratio of double to single ionization by photoabsorption $R = \sigma^{2+}/\sigma^{+}$ from threshold to 400 eV [92], the separation of Compton scattering and photoabsorption between 9 and 100 keV [93,104,261], the determination of fully differential cross-sections for photoabsorption [70,115,116,123] and a study of the electron emission in double photoionization from fixed-in-space D_2 molecules. In this section we first illustrate the role of the recoil ion for the photoabsorption process for He single ionization and show how this can be used to eliminate systematical errors for the determination of R at low photon energies (Section 5.1). We then show how fully differential cross-sections for He double photoionization can be obtained by detecting one electron in coincidence with the ion (Section 5.2). In Section 5.5 we discuss how the detection of the recoil ion momentum allows the separation of photo absorption from Compton scattering processes. The common theme of the COLTRIMS studies of photo double ionization is to explore the role of electron–electron correlations. Their motivation is therefore similar to that of many of the ion and electron impact studies reviewed in the previous sections. One might distinguish the role of correlation in the initial-state, in the final-state and dynamical correlation during the double ionization process. The latter has been termed scattering correlation and is often discussed in a simple picture of an electron–electron collision. The studies at low photon energies are mainly aiming at correlation in

the final state and scattering correlation. High photon energies in turn are well suited for the investigation of initial state correlation since the electrons are so fast that any scattering on their way out of the atom is negligible (see [70] for detailed references).

For a complete review of the rapidly expanding field of photoionization of atoms and molecules using synchrotron radiation the reader is referred to [262].

5.1. He single ionization and the ratio of double to single ionization

Momentum conservation requires, that the recoiling ion from single ionization induced by absorption of a single photon compensates for the continuum momentum of the emitted photoelectron, which carries almost all of the excess energy (see Eq. (13)). COLTRIMS allows for the first time to really visualize this basic fact of text book physics. It then exploits this fact to obtain detailed information on the process itself. Fig. 5 shows the momentum distribution of He^{1+} ions resulting from absorption of 80 eV linearly polarized photons, measured at the Advanced Light Source at LBNL. The figure displays a slice through the three-dimensional momentum distribution in the plane perpendicular to the photon beam axis. The light from an undulator is linear polarized with the main axis of the polarization ellipse along the x-axis. The outermost ring results from He^{+} ions in the ground state, the concentric rings result from ions in successive excited states. The momentum resolution in the x direction (which is the direction of the electric field of the spectrometer, where the momentum is measured via the TOF) is 0.09 a.u. corresponding to an energy resolution of 5 eV for the electrons of 55.8 eV leading to the $n = 1$ state and about 0.6 eV for $n \to \infty$ at an energy of 1 eV.

If one integrates the momentum distribution over all angles one obtains a width of 0.14 a.u. reflecting not the local resolution but the linearity of the system. Contrary to traditional electron spectroscopy the full angular range (4π solid angle) is detected at one time. There is no need to rotate the spectrometer with respect to the beam axis and there is no range of nonaccessible angles. In the off-line analysis the data can be sorted according to any angular and energy conditions in any coordinate system. For example Fig. 54 shows the ions sorted versus the cosine of their angle with respect to the polarization axis, for the $n = 1$ and $n = 2$ levels, respectively. The angular distribution of the electrons and hence the one of the recoil ions can be described by

$$\frac{d^2\sigma(\vartheta, \phi)}{d\Omega} = \frac{\sigma}{4\pi}\left(1 + \beta\left(\frac{3}{4}\,(1 - \sin\phi^2 \sin\vartheta^2 + S_1\cos\vartheta^2 - S_1\cos\phi^2\sin\vartheta^2) - \frac{1}{2}\right)\right). \tag{25}$$

In the case of the Stokes parameter $S_1 = 1$ (fully linear polarized light) the equation simplifies to

$$\frac{d^2\sigma(\vartheta, \phi)}{d\Omega} = \frac{\sigma}{4\pi}\left(1 + \beta\left(\frac{3}{2}\cos\vartheta^2 - \frac{1}{2}\right)\right). \tag{26}$$

The $n = 1$ level can be used to determine the Stokes parameter S_1, since the beta parameter is $\beta = 2$ (we obtain $S_1 = 0.99 \pm 0.01$ for the data shown in Fig. 54). Using this value the β parameter for the higher n levels can be determined (see figure). Qualitatively, the difference in the angular distributions for the higher n levels can already be seen in Fig. 5. For $n \to \infty$ the beta parameter becomes negative at 80 eV photon energy.

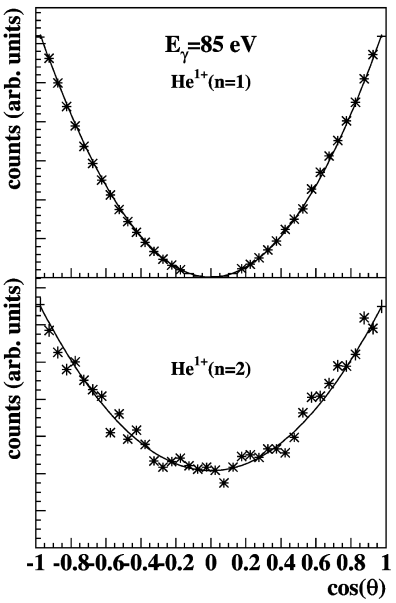

Fig. 54. Count rate versus $\cos\vartheta$ of the ion with respect to the direction of the linear polarized light, for He^{1+} ions produced by 85 eV photon impact, for the $n = 1$ and $n = 2$ ionic state. The data are integrated over all azimuthal angles (from [70]).

By integrating over the momentum distributions for He^{1+} and He^{2+} ions one obtains the ratio R of the total cross-sections. Many experimental and theoretical studies have been devoted to the photon energy dependence of R. Close to threshold the double ionization cross-section rises with $E^{1.056}$ as predicted by the Wannier threshold law [263]. R reaches a maximum at around 200 eV and slowly drops to an asymptotic value of 1.7%. The threshold behavior has been experimentally confirmed by Kossmann and coworkers [264], the asymptotic value has only recently been established [265–267,93], it will be discussed in Section 5.5 in more detail. Dörner and coworkers [92] have recently used COLTRIMS to determine precise values of R in the energy region from 85–400 eV. The results are shown in Fig. 55 together with most of the available experimental and theoretical results. The data of this work are about 25% lower than most of the previous experimental results, which have been obtained by detecting the time of flight of the ions only. The application of COLTRIMS allows to eliminate all possible sources of experimental errors which have been discussed in the literature of this subject so far, since the charge state and the three-dimensional momentum vector as well as the pulse height of the channel-plate detector signal are recorded for each ion. For example, admixture of low-energy stray light or higher harmonics would show up as larger diameter rings in Fig. 5 as well as charge exchange by secondary collisions and electron impact ionization by secondary electrons. Also, any H_2^+ contribution to the He^{2+} would have been seen in the momentum distribution. For more details on this discussion see [92,261,268]. This revision of the established data of R at lower photon energy by the COLTRIMS technique has later been confirmed by Samson and coworkers [269] (compare also [267]).

As can be seen in Figs. 55(b) and (c), the new data have severe impact on the evaluation of the available theoretical results. They clearly favor the most recent calculations by Tang and

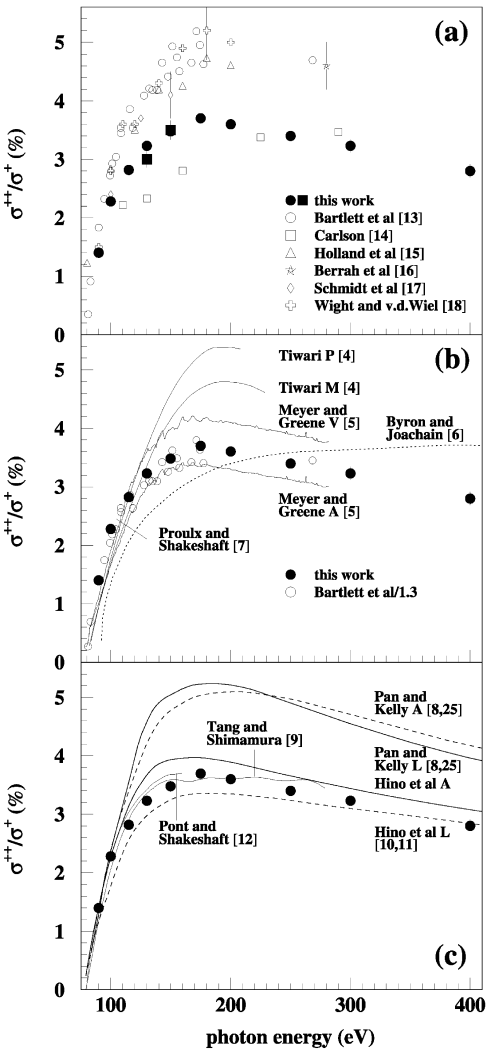

Fig. 55. Ratio of double to single ionization for photoabsorption as a function of photon energy. Full circles: COLTRIMS data taken at the ALS, full squares: COLTRIMS data taken at Hasylab. The open circles in (b) are the same data as in (a) but scaled down by 1.3 (see text). V, A, L stand for results obtained in the velocity, acceleration or length form, respectively (from [92], see there for the references given in the figure).

Shimamura [270] and Pont and Shakeshaft [271]. They are also in good agreement with calculations by Meyer and Green [272], Kheifets and Bray [273], Pindzola and Robicheaux [274] and Qui et al. [275]. Today for the full range of photon energies from threshold to the asymptotic regime the question of the ratio of total cross-section resulting from photoabsorbtion can be considered as settled.

The calculations by Pont and Shakeshaft and those of Kheifets and Bray also provide fully differential cross-sections, angular and momentum distributions of the He^{2+} ions. This will be discussed in more detail in the following section.

5.2. Multiple differential cross-sections for He photon double ionization

For double ionization of He by photon impact a complete kinematical determination of the final state requires the coincident detection of five momentum components of any of the three particles in the final state (the 4 remaining momentum components are then given by energy and momentum conservation laws, see Section 2.3). The first pioneering complete experiment on He has been performed by Schwarzkopf and coworkers [19] by detecting the two electrons in coincidence. This kind of experiment can be performed much more efficiently by measuring the recoil ion momentum in coincidence with one of the electrons. Results have been reported by Dörner and coworkers [115]. They used a spectrometer as shown in Fig. 12 with a position-sensitive electron detector facing the recoil detector. Similar to many experiments for ion impact discussed above, the data obtained with COLTRIMS differ from those obtained in coincident photoelectron detection in at least two ways which have more than technical importance. First, the complete momentum space (4π solid angle) for the ion and one of the electrons and are recorded in 'event mode'. This means that the final momenta of all three particles are determined for *every double ionization event*, with no necessity to choose 'a priori' a particular angle or energy for either electron. Thus, the entire final five-dimensional momentum space of the escaping 3 particles is sampled without prejudice, and the physical process itself determines which parts of this space are the most important ones. In principle, a similar measurement could be performed by measuring coincident photoelectrons for all angle and energy combinations, but this is an experimentally hopeless task with the solid angles of typical electron spectrometers. The overall data collection efficiency using the recoil technique is orders of magnitude higher than that realized by the coincidence photoelectron technique. Second, the recoil momentum itself, which is equal and opposite to the center-of-mass momentum of the ejected electron pair, appears to be a particularly convenient coordinate for the description of the physical process at hand. The eventmode sampling of the entire final-state momentum space allows one to transform the data into any set of collective coordinates like hyperspherical or Jacobi coordinates. Dörner and coworkers analyze their data in Jacobi coordinates $\boldsymbol{k}_r = (\boldsymbol{k}_1 + \boldsymbol{k}_2)$ (which is equal and opposite to the recoil ion momentum) and $\boldsymbol{k}_R = 1/2(\boldsymbol{k}_1 - \boldsymbol{k}_2)$. $\boldsymbol{k}_R$ describes the motion of the electrons with respect to the center of mass of the electron pair, while $\boldsymbol{k}_r$ gives the motion of this center of mass (or the Wannier saddle point of the electronic potential) in the laboratory frame (for more details see Refs. [276,277]).

Experimental results for a photon energy of 1 eV above threshold are shown in Fig. 56. The recoil ion momentum distribution appears qualitatively dipole like in character, even so close to threshold. The β parameter for the ionic motion is found to be around 0.9 at 1 eV, increasing almost to $\beta = 2$ at 80 eV above threshold. This is in qualitative agreement with two simple two-step models of double photoionization. In model (a) suggested by Samson [278] a first step of photo single ionization is followed by a second step of photo-electron impact ionization of He^{1+}. In this case the photon is absorbed in the first step by the charge dipole of the nucleus on one side and one electron on the other side. In model (b), which might be more plausible for very low photon energies, the photon is absorbed in the first step by the dipole formed by the nucleus on one side and the center of charge of the electron pair on the other side. In a second step this emitted 'dielectron' breaks then up. From both models one would qualitatively expect the observed dipole pattern of the ionic emission pattern while the electrons lose this dipolar characteristics in the

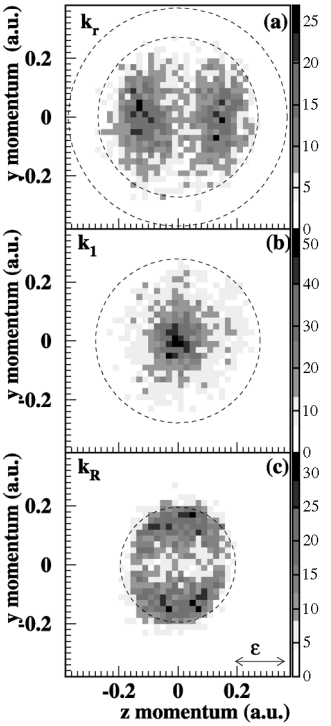

Fig. 56. Density plots of projections of the momentum spectra from double ionization of He by 80.1 eV photons. The z and y components of the momentum are plotted on the horizontal and vertical axes, respectively. The polarization vector of the photon is in the z-direction and the photon propagates in the x-direction. Only events with $-0.1 < k_{rx} < 0.1$ a.u. are projected onto the plane. (a) shows he recoil ion (or $-\boldsymbol{k}_r$) momentum distribution. The outer circle indicates the maximum calculated recoil ion momentum, and the inner circle is the locus of events for which the $\boldsymbol{k}_r$ motion has half of the excess energy. (b) shows the distribution of single electron momenta ($\boldsymbol{k}_1$ or $\boldsymbol{k}_2$). The circle locates the momentum of an electron which carries the full excess energy. (c) shows the relative electron momentum (or $\boldsymbol{k}_R$) distribution. The circle identifies the maximum possible value for $\boldsymbol{k}_R$ (from [115], see [123] for similar results 20 eV above threshold).

second step due to the strong electron–electron correlation (see Fig. 56 and the work using traditional electron spectroscopy [279,280]).

Fig. 56(c) shows the distribution of the Jakobi-momentum $\boldsymbol{k}_R = 1/2(\boldsymbol{k}_1 - \boldsymbol{k}_2)$. This reflects the motion of the electrons along the interelectronic axis of the electron pair. The electron pair breaks up preferentially perpendicular to the polarization axis of the light which is horizontal in the figure. This orientation of the interelectronic axis shows directly the preferred population of the state with a quantum number $K = 1$ over the $K = 0$ state, where K is the projection of the angular momentum along the Wannier ridge.

The excess photon energy E_{ex} is split between the $\boldsymbol{k}_R$ and $\boldsymbol{k}_r$ motion ($E_{ex} = \frac{1}{4}k_r^2 + k_R^2$). Fig. 57 demonstrates that as the photon energy approaches threshold a greater fraction of the excess energy goes into the breakup motion of the electron pair (k_R^2), while the recoil ion motion is 'cooled' on the Wannier saddle (see [277] for a detailed discussion within 4th order Wannier theory). The

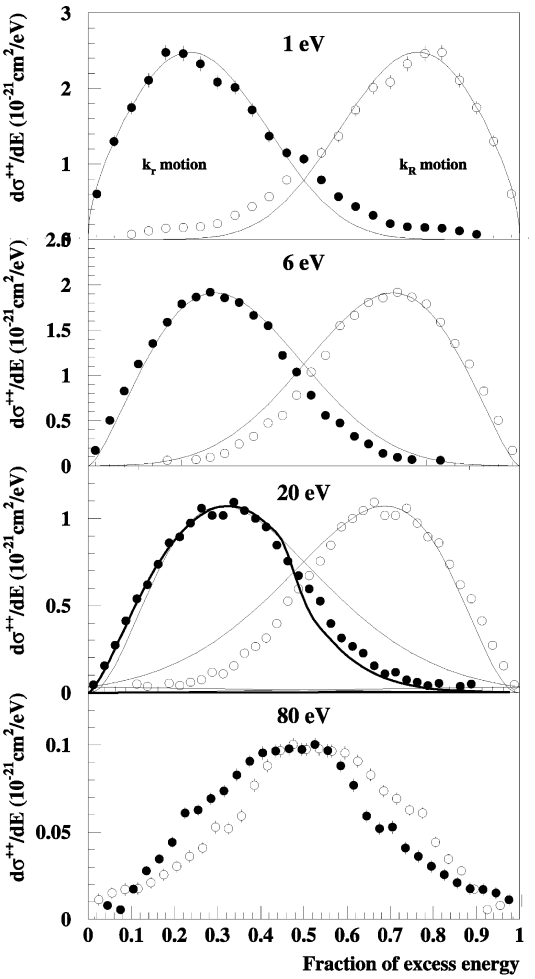

Fig. 57. Cross-sections differential in kinetic energy plotted as a function of the fraction of the excess energy in the $\boldsymbol{k}_r$ (scaled recoil ion motion) (filled circles) or $\boldsymbol{k}_R$ (breakup motion of the 'dielectron') (open circles) motion. The solid curve in the upper three figures is from the fourth-order Wannier calculation. The theoretical curves are normalized to the experiment, which is on an absolute scale. Thick line in (c) calculation by Pont and Shakeshaft [281], which is on absolute scale. The symmetry of the curves is by definition, since both fractional energies have to add up to 1 (partly from [115]).

physical reason for this behavior is that for low excess energy only those ions close to the saddle end up in the double ionization channel. Thus, the apparent 'cooling' is rather a selection of cold ions in the double ionization channel. In a recent 'a priori' calculation Pont and Shakeshaft succeeded in reproducing the relative shape as well as the absolute height of the recoil ion momentum distribution [281]. Their results at 20 eV are shown in Fig. 57. In addition, their calculated β parameter for the ionic motion is in good agreement with the experiment.

The COLTRIMS studies of fully differential cross-sections have been extended to 20 eV above threshold, by adding a solenoidal magnetic field to ensure 4π solid angle for all electrons up to

10 eV. Surprisingly, Bräuning et al. found no qualitative change in the $\boldsymbol{k}_r$-distribution compared to the data 1 eV above threshold [123]. We now change the perspective on double photoionization from collective Jacobi momentum coordinates to the more traditional point of view of single electron momenta.

For He double ionization by a single photon the two electrons in the continuum have to be coupled to a $^1P^o$ state. The internal structure of the square of this correlated continuum wave function is shown in Fig. 58. Neglecting the (small) photon momentum the vector momenta of ion and both electrons have to be in one plane. Fig. 58 shows the electron momentum distribution in this plane. The data are integrated over all orientations of the polarization axis with respect to this plane, the x-axis is chosen to be the direction of one electrons. The structure of the observed momentum distribution is dominated by two physical effects. First the electron–electron repulsion leads to almost no intensity for both electron in the same half plane. Second, the $^1P^o$ symmetry leads to a node in the square of the wave function at the point $\boldsymbol{k}_1 = -\boldsymbol{k}_2$ [19,282–284]. At 1 eV this nodal point extends to all energy sharings (see in addition [24,70]).

By omitting the integration over the orientation of the polarization, one obtains the conventional fivefold differential (FDCS) cross-sections $\mathrm{d}^5\sigma/\mathrm{d}\theta_1\,\mathrm{d}\theta_2\,\mathrm{d}\Phi_1\,\mathrm{d}\Phi_2\,\mathrm{d}E_1$, where direction and energy of one electron is fixed and the polar angle of the second electron is plotted. Some authors name such cross-sections triply differential because they replace $\mathrm{d}\theta_1\,\mathrm{d}\theta_2\,\mathrm{d}\Phi_1\,\mathrm{d}\Phi_2$ by $\mathrm{d}\Omega_1\,\mathrm{d}\Omega_2$. At low energies the linear momentum of the photon can be neglected (dipole approximation), yielding rotational symmetry around the photon polarization axes. This results in a reduction from a fivefold to a fourfold differential cross-section.

Two comprehensive set of such FDCS obtained by COLTRIMS have been published [70,286]. Since these experiments are not restricted to any particular plane by the geometry of the detectors one obtains an overview of the correlated electron emission. This is illustrated in Fig. 59 where the

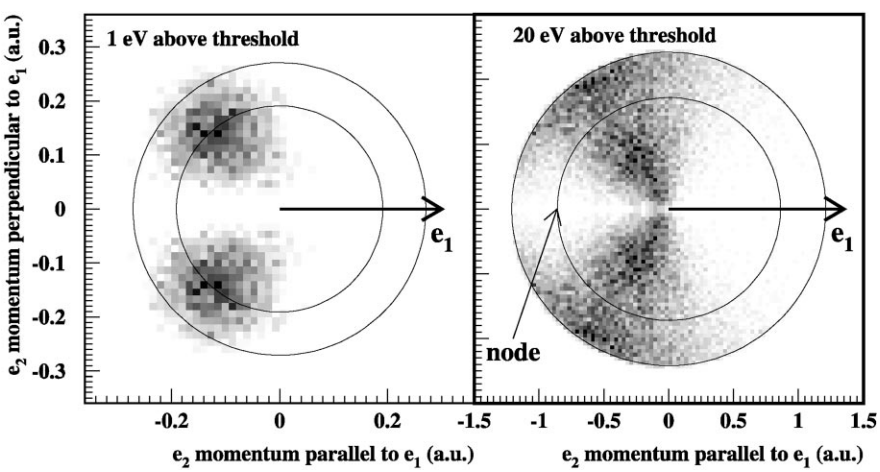

Fig. 58. Photo double ionization of He at 1 and 20 eV above threshold by linear polarized light. Shown is the momentum distribution of electron 2 for fixed direction of electron 1 as indicated. The plane of the figure is the momentum plane of the three particles. The data are integrated over all orientations of the polarization axis with respect to this plane. The figure samples the full cross-sections, for all angular and energy distributions of the fragments. The outer circle corresponds to the maximum possible electron momentum, the inner one to the case of equal energy sharing (from [285]).

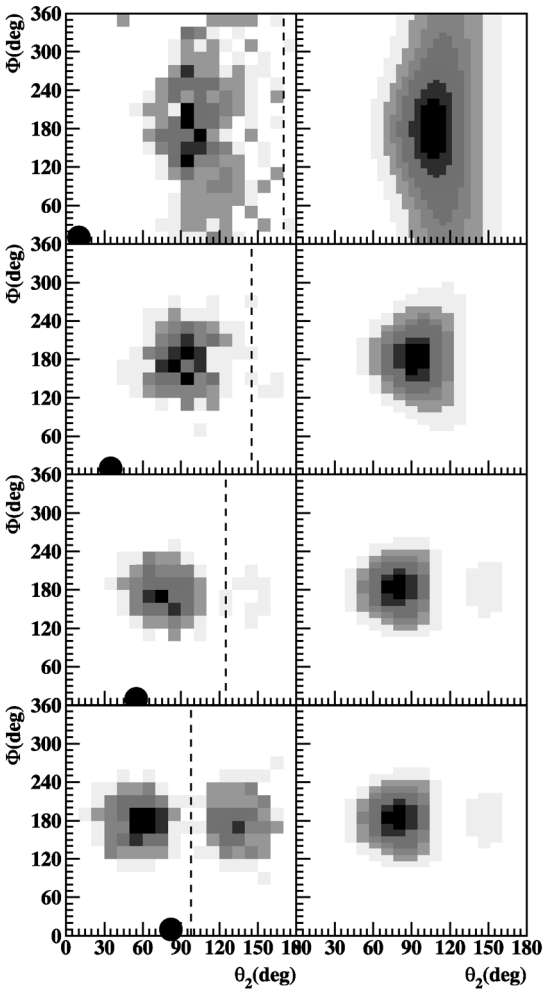

Fig. 59. $d^4\sigma/d\vartheta_1\, d\vartheta_2\, dE_1\, d\Phi$ for photo double ionization of He by 85 eV photons. Horizontal axis: polar angle of fast electron with respect to the polarization axis. Vertical axis: azimuthal angle between the electrons. The energy of the fixed electron is $E_1 = 0.1$–1 eV, $\vartheta_1 = 0$–20°, $\vartheta_1 = 30$–40, $\vartheta_1 = 50$–60°, $\vartheta_1 = 75$–90°(from top tobottom). The direction of the fixed electron is indicated by the dot. The dashed line shows the location of a node for the case of equal energy sharing. Left column: Experiment. Right column: 4th-order Wannier calculations (from [70]).

evolution of the angular distribution of the second electron for unequal energy sharing for the angle ϑ_1 varying from 0° to 90° with respect to the polarization axis for a photon energy 6 eV above the double ionization threshold is shown. Here the energy of the first electron is selected to be in 0.1–1 eV (thus the energy of the second electron is between 5 and 5.9 eV). The grey scale of the figure is linear in the cross-section $d^4\sigma/d\vartheta_1\, d\vartheta_2\, dE_1\, d\Phi$. Fig. 59 demonstrates that at all angles ϑ_1 the FDCS is maximum for $\phi = 180°$. This correspond to the coplanar geometry to which all experiments by coincident electron–electron detection have been confined. The emission of the second electron changes from a cone for ϑ_1 close to 0° to one main lobe in the intermediate range of angles, which rotates with ϑ_1. Finally, a second lobe grows as 90° is approached. It has been pointed out by

several authors [191,282–284] that such FDCS are governed by strict selection rules, especially in the case of equal energy sharing. Maulbetsch and Briggs [283] have shown that for equal energy sharing there is a node at $\vartheta_2 = 180 - \vartheta_1$. The location of this node is marked with a line in Fig. 59. The node indicated in Fig. 58 is part of this line. For unequal energy sharing this selection rule does not hold strictly. At 6 eV excess energy, however, the selection rules still seem to govern the process even for an energy sharing of 1/5.

The multiple differential cross-sections for photo double ionization obtained by COLTRIMS can easily be normalized to the absolute total cross-section for photoabsorption. This can be done since the total yield of He^{1+} and He^{2+} ions are always detected at the same time by the time-of-flight measurement. Therefore, no knowledge about the total number of photons and the gas pressure is necessary for the normalization procedure [21]. For more details see [70,286]. Such absolute values are of great interest since the different theoretical approaches for double photoionization disagree more on the absolute magnitude of the FDCS than their relative angular shape [287–289].

Fig. 60 shows the variation of the FDCS at 6 eV above threshold with energy sharing and azimuthal angle between the two electrons. The left column shows the coplanar geometry. When the second electron is pointing out of the plane defined by the first electron and the polarization vector (middle and right columns) the overall cross-section drops dramatically, with the main lobe at -270° decreasing faster than the smaller lobe. As has been shown already by Lablanquie et al. [24] the shape of the FDCS is very similar for all energy sharings such close to threshold.

5.3. Circular dichroism in He photon double ionization

If the double ionization process is induced by absorption of circularly polarized light (instead of linearly polarized), an interesting new questions arises: How is the helicity of the photon, which is absorbed by the spherical symmetric He ground state, transferred to the three-body Coulomb continuum? For photoabsorption by magnetic substances or chiral molecules it is well known that the differential cross-section depends on the helicity of the light (see [290] for a recent review). This dependence is termed circular dichroism (CD). Berakdar coworkers [291,292] have first theoretically predicted CD for photo double ionization of He. They have argued that in any geometry where the two electrons have unequal energy and are not in one plane with the photon direction, the FDCS can depend on the helicity of the photon. First experimental evidence for the existence of this effect has been seen by Viefhaus and coworkers [26]. They detected the two electrons in coincidence using time-of-flight electron spectrometers. Mergel et al. [117] and Achler [293] have used COLTRIMS to map the angular and energy dependence of CD in detail for 20 and 95 eV excess energy. They have used a spectrometer similar to the one shown in Fig. 12 and detected the fast electron in coincidence with the recoil ion. The fast electron was selected by a retarding field in front of the electron detector. Their experiment has used circular polarized light from an elliptical undulator at the Photon Factory (KEK, Tsukuba, Japan).

The measured momentum distributions for an excess energy of 20 eV are shown in Fig. 61. The photons propagate into the plane of the paper, the fast electron is fixed to the right, indicated by the arrow. The upper spectra show the He^{2+} momentum distribution. The lower spectra show the momentum distribution of the slow electron calculated from the data in the upper row event by event. Without the existence of CD these distributions would be symmetric with respect to the

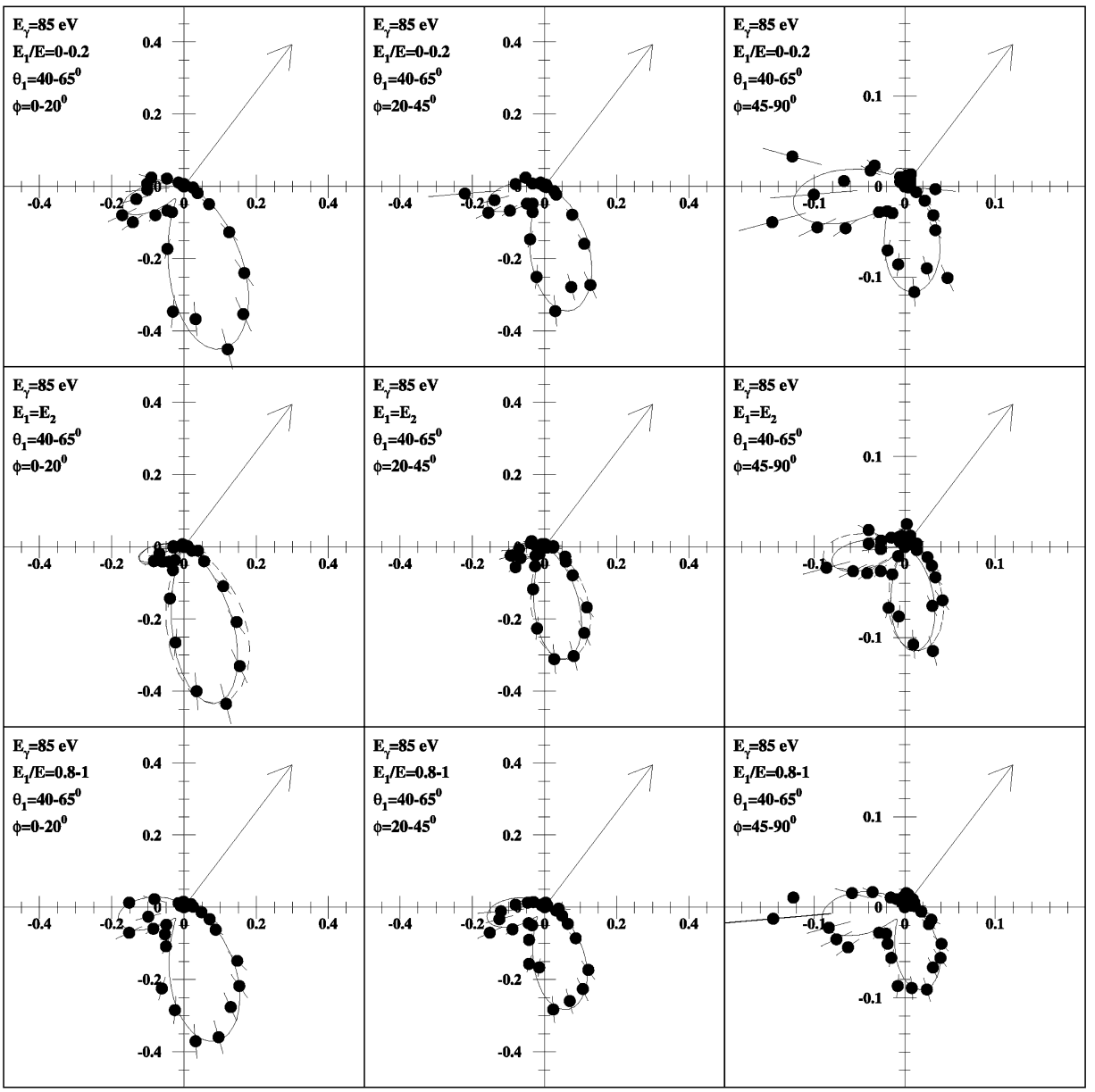

Fig. 60. $d^4\sigma/d(\cos(\vartheta_1))d(\cos(\vartheta_2))\,d\phi\,dE$ photo double ionization of He by 85 eV photons. The first electron is emitted to a polar angle range of $\vartheta_1 = 40$–$65°$. Each row is for a different energy sharing, each column for varying azimuthal angle between the two electrons as given in the figure. The dashed lines show a fit with a Gaussian correlation function with $FWHM = 84.7°$. Full line: Fourth-order Wannier calculation. The data are on absolute scale in 10^{-4} a.u., the lines are scaled to the data (from [70]).

horizontal axis of $\boldsymbol{k}_1$ (similar to those shown for linear polarized light in Fig. 58). The data show, however, that CD is a very strong effect, the handedness of the photon changes the three-body breakup pattern dramatically.

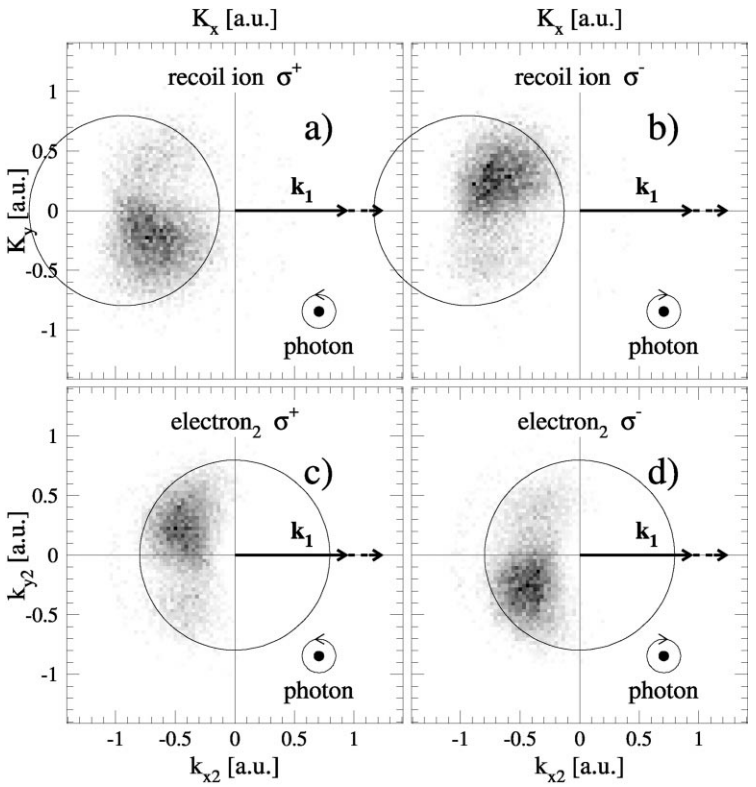

Fig. 61. Recoil ion and electron momentum distribution for photo double ionization of He by circularly polarized light at 20 eV excess energy. Shown is the plane perpendicular to the photon propagation (into the plane of the paper). Left row: σ^+ (right helicity) photons, right row σ^- (left helicity). The fast electron (11.5–20 eV) is fixed along the arrow (from [117]).

5.4. Electron emission from spatially aligned molecules

The investigation of molecular fragmentation is a further domain for the three-dimensional momentum space imaging of RIMS. A special but interesting case occurs when the ionic energies resulting from molecular fragmentation are in the eV regime and, thus, much bigger than those from most of the atomic ionization processes discussed so far. In molecular fragmentation the recoil ion momentum is usually not mainly a result of the many-body momentum exchange between electrons and heavy fragments. In contrary to the atomic case the heavy fragment motion and the electron motion are fully decoupled. Mostly the axial recoil approximation holds [294]. It assumes that one can split the process into two independent subprocesses: First, an electronic transition in which the electrons are emitted or excited while the nuclei can be assumed to stay fixed and second, a much slower process of dissociation of the leftover molecular ion. The ionic momenta measured long after both steps result mainly from the Coulomb repulsion of the nuclei in the second step. Several groups have used position-sensitive detectors capable of handling multiple hits and projection spectrometers to measure the fragmentation pattern from this second step of

molecular fragmentation. This work is beyond the scope of the present review. The reader is referred to [295,296] and references therein for work concerning ion impact and to [297] and references therein for work concerning photon impact. Only a few studies so far have tried to relate the two steps, i.e. the ejection of the electron(s) and the molecular fragmentation. Those studies combine electron and ionic fragment detection [129,298–302]. If the time scale for fragmentation is short compared to typical rotation times of the molecule, the ion direction can be taken as indication for the orientation of the molecule at the instant of the electronic excitation.

Shigemasa et al. [299,301] and Watanabe et al. [302] have used traditional electron spectrometers and channeltrons for ion detection to measure the first angular dependence of photo electrons from fixed-in-space molecules. They were able to see direct evidence for a shape resonance in the electron angular distribution from N_2 [299,303–306], CO_2 [302] and CO [301]. Studies on the carbon K electron emission from CO have also been reported by Heiser and coworkers [298]. They used imaging with a position sensitive multihit detector for the fragment-ion detection.

Golovin et al. [300] have measured the angular distribution of autoionization electrons from superexcited $O_2^{\ddagger}$ with respect to the molecular axis (see also [307]). They have used a projection spectrometer and a position-sensitive detector for the recoil ion momentum measurement and combined it with a simple time-of-flight spectrometer without position resolution for electron detection. They found first evidence for an intra molecular scattering of the 0.16 eV electron at the second nucleus of the O_2. The ejection characteristics is shown in Fig. 62.

For comparison with the He work reviewed above, double ionization of H_2, the corresponding molecular two-electron system, is of particular interest. Here, in principle much more complex electron angular distribution becomes possible [308], since angular momentum can be coupled to the nuclear motion. In addition an interference originating from electron emission from the two identical centers has been predicted [309,310]. Pioneering experimental work detecting the two fragment ions, integrating over the electrons can be found in [311,312] and the first experiments detecting both electrons in coincidence, but integrating over the ionic momentum distributions has been reported by two groups [27,313,314]. Dörner et al. [129] have used a COLTRIMS setup with two-dimensional position-sensitive detectors and solenoidal magnetic field for 4π momentum

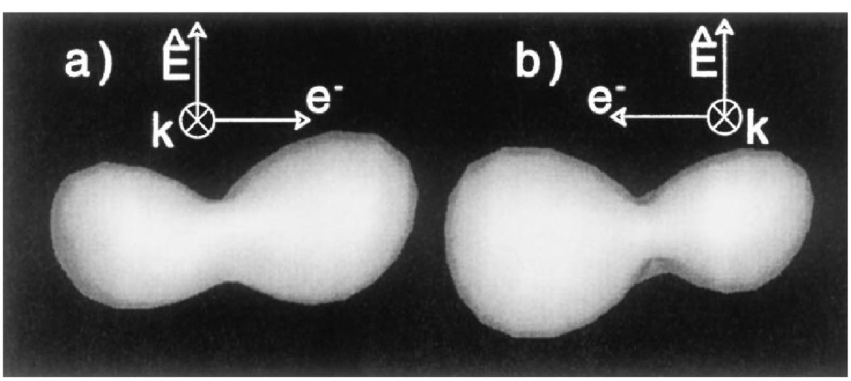

Fig. 62. Distribution of O^+-ions coincident with 0.16 eV electrons from photoabsorption of O_2 at a photon energy of 22.36 eV. The light propagates into the plane shown, the slow electron and the polarization are indicated in the figure (from [300]).

space mapping of both heavy fragments and one of the two electrons from photo double ionization of D_2. In this study a supersonic gas-jet target and a delay-line detector as shown in Fig. 18 is used for detection of both d^+ ions. They illustrated how the total available excess energy is partitioned between the four fragments. This leads to an electron-energy distribution with a smooth upper threshold, significantly different from double photoionization of an atom (e.g. Helium). In turn, the energy deposited in the electronic motion yields ion energies smaller than expected from pure Coulomb repulsion of the two nuclei following instantaneous removal of the electrons. Such behavior has been first predicted by LeRouzo [315,316]. The angular distribution of the electrons shows no reminiscence of the broken spherical symmetry in the molecule. Even so the electron angular distribution from spatially aligned molecules can in general not be described by Eq. (25). They found that for D_2 double ionization close to threshold the energy integrated electron angular distributions could be well fitted with a β parameter. This β is found to be more positive for D_2 than for He. In addition, the β parameter depends on the orientation of the molecular axis (see Fig. 63).

5.5. Separation of photoabsorption and Compton scattering

It has been predicted as early as 1967 [317] that the ratio R of double to single ionization for photoabsorption will approach an asymptotic value of 1.7% for $E_\gamma \to \infty$. In calculating the process of double photoionization most of the theoretical problems result from the electron–electron correlation in the final state. For high photon energy, however, this final state

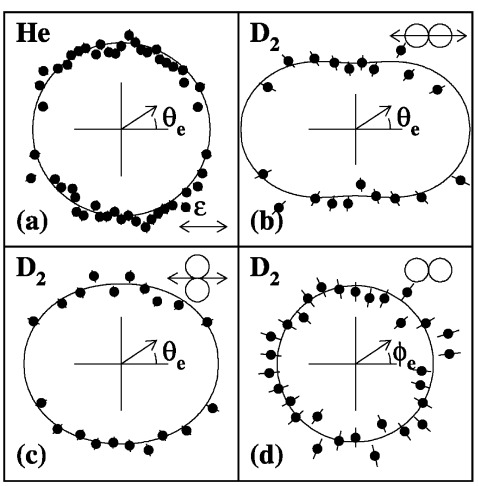

Fig. 63. Polar representation of the angular distribution of one of the two photoelectrons from photo double ionization of helium at 7 eV excess energy and of D_2 also at about 7 eV excess energy (cf. Fig. 1(e)). The data have been integrated over all electron energies. (a) $d\sigma/d\cos\vartheta_e$ for helium with ε along the horizontal. The line shows a fit with $\beta_e = 0 \pm 0.04$. (b) $d\sigma/d\cos\vartheta_e$ for D_2 with ε along the horizontal and the molecular axis held fixed parallel to ε. The line shows a fit with $\beta_e = 0.4 \pm 0.1$. (c) Similar to (b) but for alignment of the molecule perpendicular to ε. The data are integrated over all azimuthal angles. The line shows a fit with $\beta_e = 0.14 \pm 0.08$. (d) $d\sigma/d\phi_e$ for D_2 with $70^\circ < \vartheta_e < 110^\circ$ (90° is the plane of the paper). The molecule is held fixed perpendicular to ε, *which now points out of the paper*. The full line is a circle to guide the eye (from [129]).

correlation becomes negligible and, thus, the asymptotic value of R is believed to be a one of the benchmark tests for our understanding electron–electron correlation in the initial ground state of the He. It tests the wave function at the Cusp condition (i.e. for one of the electrons at the nucleus). Only recently, with the availability of modern synchrotron light sources this question has been accessed experimentally. Levin and coworkers have performed the first experiment at 2.7 keV in the hope that the asymptotic value might have been reached already [265]. It has been pointed out by Samson and coworkers [318,319] that at 4 keV the contribution of Compton scattering to the He^{1+} production is comparable to the contribution from photoabsorption. Therefore, all experiments which detect only the charge state of the ion do not measure R for photoabsorption (R_p) but the mean value of R_p and R_c weighted with the corresponding cross-sections. Although agreement between various calculation has been reached on the predicted asymptotic value of R_p (see, e.g. [320–327,289,177,275]) the calculated values for R_c differ by more than a factor of 2 (see, e.g. [328–331] and Fig. 65).

COLTRIMS offers a natural way to distinguish for each ion, whether it resulted from a Compton scattering or a photoabsorption process, and, thus, allows to determine R_p and R_c separately [93,104,268,332,333,319]. As has been outlined in Section 5.1 momentum conservation for photoabsorption requires that the ion compensates the electron (sum-)momentum leading to large recoil ion momenta. In a Compton scattering event, however, the photon delivers momentum and energy to the electron in a binary collision leaving the nucleus a spectator to the process. Thus, the recoil ion will show mainly the initial-state momentum distribution (Compton profile). This is very similar to ionization by charged particle impact in the Bethe–Born limit, where the transition matrix is identical to the one obtained for photon scattering as pointed out by Bethe [334] as early as 1930. We have encountered this situation for single ionization by 0.5 MeV p impact (Section 4.1.2.2(a)), the process of projectile ionization by (e–e) interaction (see Section 4.2.3) and the process of (e–e) Thomas scattering in transfer ionization (see Section 4.2.2). All these reaction the maximum contribution to the cross-section results kinematical conditions with a minimum momentum transfer to the nucleus, the so called 'Bethe ridge' [334].

The resulting momentum distributions of the recoil ions at around 9 keV photon energy from the pioneering work of Spielberger et al. [93] is shown in Fig. 64. In this experiment 'broad-band' light from an undulator had to be used to obtain sufficient counting rate. The He^{1+} momentum distribution reflects this energy spread.

From Eq. (13) it can be seen that for photoabsorption the sphere of ion momenta is shifted forward by the momentum of the photon ($p_\gamma = 2.4$ a.u. at 9 keV), while this does not hold for Compton scattering (this does not show up in Fig. 64 since both axis plotted are perpendicular to the photon beam propagation). By integrating the respective areas in momentum space one obtains the ratio R_c and R_p. Fig. 65 shows the measured ratios for Compton scattering.

For photoabsorption at 9 keV very good agreement with the predicted value of 1.7% is found. The physical parameter to which the limes applies is not the photon energy, but the velocity with which the primary electron leaves its atom. For photoabsorption at high photon energy, photon and electron energy approach each other. Compton scattering, however, produces a broad distribution of electron energies. Thus, very high photon energies are needed in order to obtain mainly Compton electrons with high energies [320,330,338–341]. In a precision measurement Spielberger et al. explored the photon energy dependence of R_C up to 100 keV photon energy. They found a value of $R_C = 0.98 \pm 0.09$ (see Fig. 65). In a theoretical analysis of these results the authors

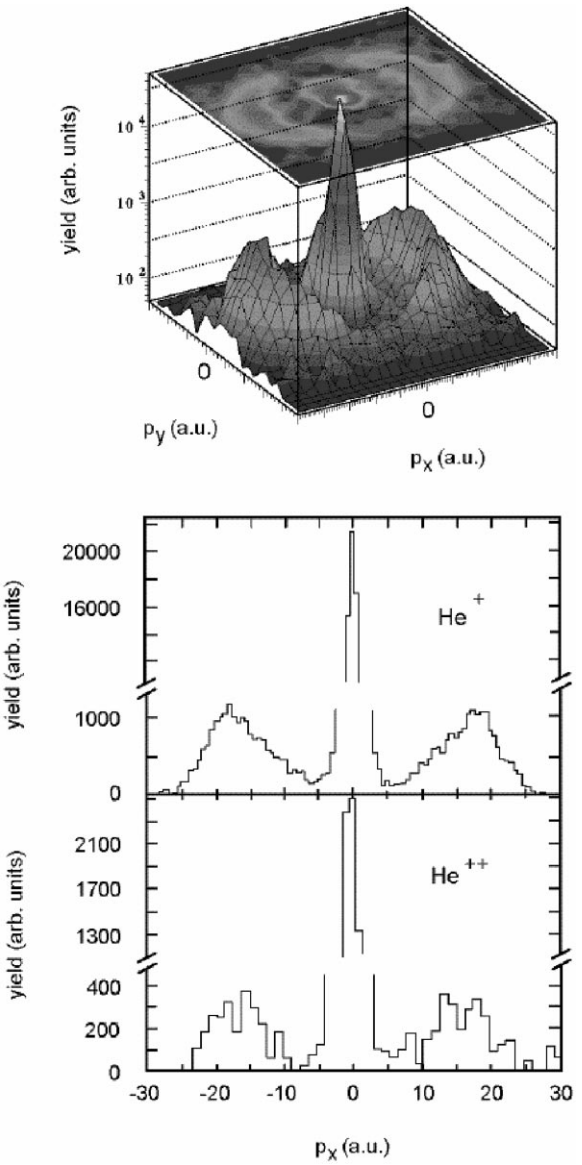

Fig. 64. Momentum distribution of He ions from photon impact at about 9 keV. Upper figure: Momentum distribution of He^{1+} ions. The circular reef is due to photoabsorption, the narrow spike at zero momentum due to Compton scattering. The light propagates into the plane of the figure, the polarization is along the x-axis. Middle: Distribution of He^{1+} ion momenta along the polarization axis, integrated over both other directions. Lower: As middle but for He^{2+} ions (from [93]).

showed that this value is still slightly influenced by a contribution of slow electrons and not yet the asymptotic value.

These studies have clearly proven that the probability for shaking of the second electron differs significantly whether the first electron is removed by photoabsorption or by Compton scattering.

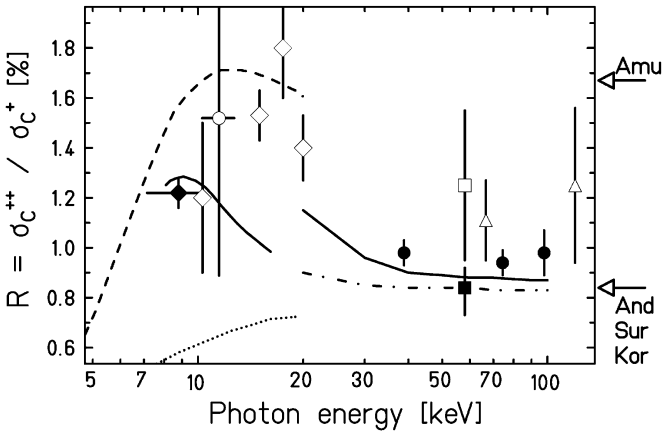

Fig. 65. Ratio of He^{2+}/He^{1+} ions created by Compton scattering as function of the photon energy. Full symbols: COLTRIMS data from [261,104,93] (circles,diamond,square). Open Circle: [266]. Open diamonds: [267]. Open square: [335]. Open triangle pointing up: [336]. Open triangle pointing down: [337]. Dashed line: Calculation (BBK-type wavefunction) [329]. Dotted line: [330], Full line: BBK-type final state [261]. Dashed-dotted line: [261]. The arrows indicate the predicted asymptotic values of upper arrow [328], lower arrow [329–331] (adapted from [261]).

The physical differences responsible for this can be seen in the recoil ion momentum distribution. While photoabsorption picks only that fraction of the wave function where one electron (and the ionic core) have large momenta (i.e. where the electron is found close to the nucleus), Compton scattering samples the whole momentum space wave function [339]. In both cases the fraction of the initial state wave function which is selected by the process is mirrored in the recoil ion momentum.

6. Outlook

The investigation of many-particle atomic collision systems, where small momentum transfers between the collision partners dominate might be the most important application of COLTRIMS. To study the correlated motion of few electron systems in momentum and spin space, wherever the latter is possible too, is of fundamental interest. Here COLTRIMS can provide a momentum resolution which is about a factor hundred better than the mean momentum of the most weakly bound electron in any stable atom. Measuring the sum momentum of two or more ejected electrons or one electron momentum with respect to another given electron momentum in atomic systems, one can obtain detailed information on the correlated motion of electrons in atoms.

In this section we will present some ideas of experiments in atomic and molecular physics as well as in other fields, e.g. neutrino physics and surface science, which so far were not possible with existing detection techniques. This list is just an introduction to a new direction of research and it might stimulate other colleagues to use COLTRIMS in different areas of physics or chemistry.

(a) *QED effects in the inner-shell binding energies in H-like uranium ions*: To determine QED effects, e.g. in the binding energy of the 1s state of H-like uranium ions an absolute energy determination of about 0.1 eV is desirable [5,342–344]. Different attempts have been made, to

measure these binding energies by detecting the innershell X-ray transition energies. Presently, however, no X-ray detection system is available which can provide the required precision at large enough solid angle. As outlined in Section 2.1.1 the 1s binding energy of U^{91+} ions can be determined by measuring the recoil ion longitudinal momentum in the following capture reaction:

$$U^{92+} + He \rightarrow U^{91+}(1s) + He^{1+}(1s). \tag{27}$$

For decelerated ions with $v_{pro} = 14$ a.u. the He^{1+} longitudinal momentum is $k_{||rec} = 630$ a.u. If this is measured with 0.05 a.u. precision one might obtain an overall Q-value resolution of 10 eV. Thus, the required 0.1 eV resolution for the center of its distribution seems to be feasible. Serious difficulties of the experiment are the very weak capture cross-section into the uranium 1s state, the small impact parameters probably contributing to 1s capture (large transverse recoil momenta) and the second He electron being very likely emitted during the capture. Work is in progress to explore the feasibility of such experiments.

(b) *Dynamics of correlated multi-electron processes in highly charged ion–atom collision; Resonant Electron Transfer-Excitation Process* (RTE): It has been shown that one of the important electron transfer processes between fast ions colliding with atoms is due to the interaction of a projectile electron with a target electron. This process can occur, when both electrons share in a resonant way their energy yielding a resonant excitation of the projectile electron and simultaneous capture of a target electron. Due to the width of the target momentum distribution (Compton profile) the resonance as a function of the projectile velocity shows a broad distribution. Since no electron is freed in this process discrete values for the longitudinal recoil ion momenta will be found. The transverse recoil ion momentum distribution, however, will reflect the full dynamics of this correlated process and allows to access the electron momentum during the transition (see [345–347]).

(c) *Multidifferential studies of Compton scattering in momentum space*: Differential studies of double ionization of He and other atoms and molecules (such as aligned H_2) become feasible by measuring the slow shake-off electron in coincidence with recoil ion momentum. This will provide a much more refined test of ground state correlation as total cross-sections. For aligned molecules and laser prepared atoms a coincident measurement of Compton scattered photons with the ion momentum gives access to three-dimensional Compton profiles. This is analogue to the most advanced coincident Compton scattering studies at solids in which the scattered photon and the Compton electron are measured in coincidence [348].

(d) *Molecular fragmentation induced by photons*: Momentum space imaging of all ions and all electrons from photoionization and/or excitation is one of the most sensitive probes for molecular structure and chemical dynamics. With the high resolution of the available photon sources highly selective excitation of the molecules can be achieved and the imaging of all the fragment momenta with multi-hit detection devices allows in detail to investigate the internal dynamics in the molecule after the ionization/excitation.

(e) *Molecular fragmentation following ion impact*: Slow highly charged ions are well suited for a soft removal of many electrons of a molecule leading to multiple fragmentation. Relativistic highly charged ion impact can be used also for inducing a complete fragmentation of molecules. Complete momentum space imaging of ionic fragments and electrons (as it has already been demonstrated for atoms by Moshammer and coworkers, see Sections 4.1.2.3 and 4.2.1 and references given there) gives access to electronic and geometric structure of the molecules. The high

resolution for the ionic momenta achievable with COLTRIMS will also allow to address the fundamental question of the coupling of electronic and nuclear motion in a molecule.

(f) *Multiphoton double ionization*: For double ionization of He in intense laser fields so far only total rates can be measured (see [349] and references therein). For a sensitive probe of theoretical models, however, differential cross-sections for this process are highly desirable. The determination of the momentum distribution of the He^{2+} ions is the most promising candidate for differential cross-section measurements, since contrary to electron detection, the signal is already discriminated against single ionization.

(g) *EPR-which-way experiment in momentum space*: Photo single ionization of a very cold He atomic beam by an extremely focussed photon beam produced by a free-electron laser (FEL) provides a very monoenergetic electron source with a long coherence length (see Fig. 5 for an example for the emission characteristics). Such electrons can create interference patterns behind a double slit device, due to the superposition of the two different coherent scattering amplitudes. Möllenstedt and Düker [350,351] have first demonstrated such interference by using a special electron gun and a biprisma interferometer they invented for the double slit. If the electrons are, however, produced by photoionization of very cold atoms in thin gas phase, each electron emission is accompanied by a recoiling ion which has exactly opposite momentum (see Section 2.3 and Fig. 5). Thus, measuring the recoil ion momentum in coincidence with the electron after the double slit, one can try to use the recoil ion direction to infer through which of the slits the electron was directed. In terms of the EPR paradoxon [352] the ion and the electron form an entangled state and this is an attempt to measure the momentum on one subsystem and the position on the other. This proposed experiment is a realization of a thought experiment which Einstein brought up already in his discussions with Bohr [353–355]. He suggested measuring the recoil momentum on a tiny hole which forms the source of a double slit experiment. An adaption of Bohr's famous refutation of Einstein's thought experiment in the present context shows that one would have to focus the photon beam such that its focal diameter times its transverse momentum are smaller than allowed by the uncertainty principle. A detailed quantum mechanical analysis of such an experiment can be found in [356].

(h) *Angular correlation between electron and neutrino in the tritium- β-decay and measurement of the neutrino rest mass*: One of the historically first recoil ion momentum measurements has been the experimental determination of the recoil effect of the neutrino from orbital electron capture decay of ^{37}Ar to ^{37}Cl by Rodenback and Allen [357] and its precursors (see for example [358–360]). For a beta decay leading to a free electron a precision measurement of the electron and nuclear recoil momentum together with the precise knowledge of the Q-value allows via energy and momentum conservation a determination of energy, momentum and emission angle of the neutrino for each decay. Since energy and momentum of the neutrino are measured, one can deduce in principle the neutrino rest mass for each single neutrino. This measurement does not depend on a statistical evaluation of a spectrum like measurements of the Curie-plot-endpoint (see, e.g. [361] and references therein) or on model assumptions. The most suitable would be the tritium decay. If a TH or T_2 molecular gas target can be cooled by laser cooling or other techniques to approximately $10\,\mu K$ temperature the momentum of the recoiling H^3He^{1+} molecule can be measured by a sufficiently large spectrometer device (about 5 m length) with approximately 0.001 a.u. precision. The absolute momentum vector is obtained by detecting the recoil with a large position-sensitive detector, which measures the TOF and the emission angle. All recoil ions can be projected by

proper field configurations on such a detector yielding nearly 4π solid angle. The electron momentum vector has to be determined with equivalent high precision too, which might be achieved by collecting all electrons in a long solenoidal field configuration and projecting them on a second position sensitive channel-plate detector. The TOF of electron and recoil might be obtained by detecting the Lyman photon emission of the excited $^3He^{1+}$-ion in coincidence with the recoil ion and the electron. To yield the angular $e^- \nu_e$ correlation only the electron position has to be measured. For the above given resolution the angular resolution between both particles can be as good as 10^{-3} rad. Estimates for the neutrino mass resolution yield about 10 eV/c for each single detected event (if the electron energy is within 50 eV to the upper limit).

(i) *Laser controlled targets*: The implementation of laser prepared and laser cooled targets for COLTRIMS opens a wide field of applications in atomic collision physics. Compared to gas-jet targets much lower internal temperature and thus higher momentum resolution is obtainable with such targets. This was recently demonstrated in pioneering work by Wolf and coworkers [362]. The target density achievable in MOT traps is already today high enough to allow for collision experiments with external beams. In addition to the improved resolution such targets open the way to multi-differential studies of charged particle and photon interaction with excited and specially prepared states. For example for reactions with Rydberg atoms highly differential cross-sections can be studied. Such experiments are in preparation in several laboratories.

(j) *Imaging of surface ionization*: The adaption of the COLTRIMS ion imaging technique to electron imaging as outlined in Section 3.5 has a wide application for the study of single and multiple electron emission from surfaces (see Ref. [124] for an imaging spectrometer for surface studies). One example is the correlated emission of two electrons by absorption of one photon from a surface (see, e.g. [363–365] and references therein). Such studies will strongly profit from the large solid angle of imaging spectrometers. They can yield information on the correlated motion of electrons in solids. Equally interesting is the electron emission from solids by charged particle impact. In a first multi coincidence study Moshammer and coworkers detected up to 10 electrons emitted by impact of one single fast projectile.

Besides electrons from surfaces also ions released from surfaces can be observed by such imaging techniques. In particular sputtered ions emitted from slow highly charged ion impact on surfaces are an interesting candidate new types of microscopes.

(k) *QED effects in 80 GeV/u U on Au collisions*: Theory has predicted that in ultrarelativistic heavy-ion heavy-atom collisions at small internuclear distances (R) the pair creation probability can exceed unity. Thus, the QED calculations cannot be based on perturbation theory and must include the higher order effects in an accurate way. The regime of strong perturbation (i.e. small (R)) can experimentally only be explored, if the pair creation is measured for a given projectile scattering angle. In these encounters the angles of interest are below 10^{-6} rad and, therefore, not resolvable with traditional detection devices. Measuring the recoil ion transverse and longitudinal momentum components complete information on the scattering angle and on the pair creation is obtained. Since for the collisions of interest the recoil momenta are several 10^4 a.u. even thin solid targets can be used for these measurements.

We could only present here a biased and incomplete list of the exciting future prospects of COLTRIMS and related new imaging techniques. We tried to give a flavor of the huge potential of this field, which is compared to traditional electron or photon spectroscopy still very young. The recent developments started with drift-time measurements of ions in field-free gas cells. In a series

of innovations cold gas cells, effusive gas jets, supersonic jets, precooled supersonic jets and in a first experiment even laser trapped atoms were used as target. The spectrometer development went from early drift tubes to projection fields involving three-dimensional focussing for ions and magnetic confinement for electrons. These latest combined electron-ion imaging devices are equipped with multi-hit detectors for multiple-electron and multiple-ion detection. This rapid technical development in the field reviewed here went along with an even more impressive widening of the scope of fundamental physical problems tackled. Today momentum space studies already cover electron impact, photon impact from threshold to 100 keV and ion impact from keV protons to GeV/u U^{92+} projectiles. The unprecedented resolution and completeness of many of those investigations allowed the resolution of some long-standing puzzles in atomic collision physics but at the same time raised even more fundamental questions. Similar impact of such imaging techniques can be expected for the future for other fields in physics, chemistry and related areas.

Acknowledgements

Many people have been involved in the development of COLTRIMS reviewed here. Most of the experimental work and technical development has been done, like mostly in todays experimental physics, by collaborators who left academic physics after they received their Diploma or Ph.D. They are to numerous to mention all of them. The work was driven by a longstanding close collaboration between several experimental and theoretical groups. Here we are particularly grateful to our friends and colleagues C.L. Cocke, R.E. Olson, M.H. Prior, J. Feagin, W. Schmitt, Th. Weber, Kh. Khayyat, H. Bräuning, M. Achler, J. McGuire, T. Kambara, Y. Awaya, Y. Azuma, R. Dreizler, S. Keller, H.J. Ast, H.J. Lüdde, A. Cassimi, A. Lahmam-Bennani, R. Ali, U. Buck, V. Schmidt, B. Krässig, M. Schulz, D. Gemmel, S. Hagmann, J. Burgdörfer, C. Wheelan, R. Shakeshaft, Dz. Belkic, B. Sonntag and to C. Freudenberger for the help with many figures of this review.

We acknowledge financial support from BMBF, DFG, GSI, the Max Planck Forschungspreis, Alexander von Humboldt Stiftung, the Habilitandenprogramm der DFG, DFG within SFB276 (project B7,B8), DOE, DAAD, Studienstiftung des deutschen Volkes (V.M.), 'Freunde und Förderer der Universität Frankfurt' and the Graduiertenförderung des Landes Hessen.

References

[1] H. Dehmelt, Rev. Mod. Phys. 62 (1990) 525.
[2] N.F. Ramsey, Rev. Mod. Phys. 62 (1990) 541.
[3] P.J. Mohr, G. Soff, Phys. Rev. Lett. 70 (1993) 158.
[4] W.R. Johnson, G. Soff, At. Data Nucl. Data Tables 33 (1985) 405.
[5] Th. Stöhlker, P.H. Mokler, K. Becker, F. Bosch, H. Eickhoff, B. Franske, M. Jung, T. Kandler, O. Klepper, C. Kozhuharov, R. Moshammer, F. Nolden, H. Reich, P. Rymuza, P. Spädtke, M. Steck, Phys. Rev. Lett. 71 (1993) 2184.
[6] G. Werth, Phys. Scripta 191 (1987) T22.
[7] M. Weitz, F. Schmidt-Kaler, T.W. Hänsch, Phys. Rev. Lett. 68 (1992).
[8] Th. Udem, A. Huber, B. Gross, J. Reichert, M. Prevedelli, Phys. Rev. Lett. 79 (1997) 2646.
[9] M.A. Coplan et al., Rev. Mod. Phys. 66 (1994) 985 and References therein.

[10] I.E. McCarthy, E. Weigold, Rep. Prog. Phys. 54 (1991) 789.
[11] A. Lahmam-Bennani, J. Phys. B 24 (1991) 2401.
[12] B. El Marji, A. Lahmam-Bennani, A. Duguet, T.J. Reddish, J. Phys. B 29 (1996) L1.
[13] B. El Marji, C. Schröter, A. Duguet, A. Lahmam-Bennani, M. Lecas, L. Spielberger, J. Phys. B 30 (1997) 3677.
[14] C. Schröter, B. El Marji, A. Lahmam-Bennani, A. Duguet, M. Lecas, L. Spielberger, J. Phys. B 31 (1998) 131.
[15] M.J. Ford, J.D. Doering, M.A. Coplan, J.W. Cooper, J.H. Moore, Phys. Rev. A 51 (1995) 418.
[16] A. Lahmam-Bennani, C. Dupré, A. Duguet, Phys. Rev. Lett. 63 (1582) 1989.
[17] A. Dorn, R. Moshammer, C.D. Schröter, T. Zouros, W. Schmitt, H. Kollmus, R. Mann, J. Ullrich, Phys. Rev. Lett. 82 (1999) 2496.*
[18] I. Taouil, A. Lahmam-Bennani, A. Duguet, A. Duguet, L. Avaldi, Phys. Rev. Lett. 81 (1998) 4600.*
[19] O. Schwarzkopf, B. Krässig, J. Elmiger, V. Schmidt, Phys. Rev. Lett. 70 (1993) 3008.***
[20] O. Schwarzkopf, B. Krässig, V. Schmidt, F. Maulbetsch, J. Briggs, J. Phys. B 27 (1994) L347–L350.*
[21] O. Schwarzkopf, V. Schmidt, J. Phys. B 28 (1995) 2847.
[22] A. Huetz, P. Lablanquie, L. Andric, P. Selles, J. Mazeau, J. Phys. B 27 (1994) L13.
[23] G. Dawber, L. Avaldi, A.G. McConkey, H. Rojas, M.A. MacDonald, G.C. King, J. Phys. B 28 (1995) L271.
[24] P. Lablanquie, J. Mazeau, L. Andric, P. Selles, A. Huetz, Phys. Rev. Lett. 74 (1995) 2192.
[25] J. Viefhaus, L. Avaldi, F. Heiser, R. Hentges, O. Gessner, A. Rüdel, M. Wiedenhöft, K. Wielczek, U. Becker, J. Phys. B 29 (1996) L729.
[26] J. Viefhaus, L. Avaldi, G. Snell, M. Wiedenhöft, R. Hentges, A. Rüdel, F. Schäfer, D. Menke, U. Heinzmann, A. Engelns, J. Berakdar, H. Klar, U. Becker, Phys. Rev. Lett. 77 (1996) 3975.
[27] J.P. Wightman, S. Cveejanovic, T.J. Reddish, J. Phys. B 31 (1998) 1753.
[28] A.J. Murray, F.H. Read, Phys. Rev. A 47 (1993) 3727.
[29] J. Ullrich, R. Dörner, V. Mergel, O. Jagutzki, L. Spielberger, H. Schmidt-Böcking, Comm. At. Mol. Phys. 30 (1994) 285.
[30] R. Dörner, V. Mergel, L. Spielberger, O. Jagutzki, S. Nüttgens, M. Unverzagt, H. Schmidt-Böcking, J. Ullrich, R.E. Olson, K. Tökesi, W.E. Meyerhof, W. Wu, C.L. Cocke, in: AIP Conference Proceedings Vol. 360, 1995. L.J. Dube, J.B.A. Mitchell, J.W. McConckey, C.E. Brion (Eds.), AIP Press, New York, 1995.
[31] R. Dörner, V. Mergel, L. Spielberger, M. Achler, Kh. Khayyat, T. Vogt, H. Bräuning, O. Jagutzki, T. Weber, J. Ullrich, R. Moshammer, M. Unverzagt, W. Schmitt, H. Khemliche, M.H. Prior, C.L. Cocke, J. Feagin, R.E. Olson, H. Schmidt-Böcking, Nucl. Instr. and Meth. B 127 (1997) 225–231.
[32] J. Ullrich, W. Schmitt, R. Dörner, O. Jagutzki, V. Mergel, R. Moshammer, H. Schmidt-Böcking, L. Spielberger, M. Unverzagt, R.E. Olson, The Physics of Electronic and Atomic Collision, XX, AIP Conference 1998, in print.
[33] J. Ullrich, R. Moshammer, R. Dörner, O. Jagutzki, V. Mergel, H. Schmidt-Böcking, L. Spielberger, J. Phys. B 30 (1997) 2917. Topical Rev.*
[34] J.T. Park, in: R.G. Cook (Ed.), Collision Spectroscopy, Plenum Press, New York, 1978, p. 19.
[35] W. Wu, S. Datz, N.L. Jones, H.F. Krause, B. Rosner, K.D. Sorge, C.R. Vane, Phys. Rev. Lett. 76 (1996) 4324.
[36] R. Schuch, H. Schöne, P.D. Miller, H.F. Krause, P.F. Dittner, S. Datz, R.E. Olson, Phys. Rev. Lett. 60 (1988) 925.
[37] J. Ullrich, H. Schmidt-Böcking, Phys. Lett. A 125 (1987) 193.***
[38] B. Fastrup, in: Methods of experimental Physics, Vol. 17, Academic Press, New York, 1980, p. 149ff.
[39] E. Everhart, Q.C. Kessel, Phys. Rev. Lett. 14 (1995) 247.
[40] Q.C. Kessel, E. Everhart, Phys. Rev. 146 (1996) 16.
[41] N.V. Federenko, V.V. Afrosimov, Sov. Phys.-Tech. Phys. 1 (1956) 1872.
[42] C.L. Cocke, R.E. Olson, Phys. Rep. 205 (1991) 155.
[43] J.W. McConkey, A. Crowe, M.A. Hender, Phys. Rev. Lett. 29 (1972) 1.
[44] L.J. Puckett, D.W. Martin, Phys. Rev. A 5 (1976) 1432.
[45] W. Steckelmacher, R. Strong, M.W. Lucas, J. Phys. B 11 (1978) 1553.
[46] J.C. Levin, R.T. Short, O.S. Elston, J.P. Gibbons, I.A. Sellin, H. Schmidt-Böcking, Phys. Rev. A 36 (1987) 1649.
[47] J.P. Grandin, D. Hennecart, X. Husson, D. Lecler, I. Lesteven-Vaisse, D. Lisfi, Europhys. Lett. 6 (1988) 683.
[48] C.E. Gonzales Lepra, M. Breinig, J. Burgdörfer, R. DeSerio, S.B. Elston, J.P. Gibbons, H.P. Hülskötter, L. Liljeby, R.T. Short, C.R. Vane, Nucl. Instr. and Meth. B 24/25 (1987) 316.
[49] J. Ullrich, H. Schmidt-Böcking, C. Kelbch, Nucl. Instr. and Meth. A 268 (1988) 216.

[50] J. Ullrich, R.E. Olson, R. Dörner, V. Dangendorf, S. Kelbch, H. Berg, H. Schmidt-Böcking, J. Phys. B 22 (1989) 627.***
[51] R. Dörner, J. Ullrich, H. Schmidt-Böcking, R.E. Olson, Phys. Rev. Lett. 63 (1989) 147.**
[52] J. Ullrich, R. Dörner, R.E. Olson, H. Schmidt-Böcking, in: A. Dalgarno, R.S. Freund, P.M. Koch, M.S. Lubell, T.B. Lucatorto (Eds.), The Physics of Electronic and Atomic Collisions, Invited Papers of the ICPEAC, Vol. XVI, AIP, New York, 1989, p. 372.
[53] R. Dörner, J. Ullrich, O. Jagutzki, S. Lencinas, A. Gensmantel, H. Schmidt-Böcking, in: W.R. MacGillivray, I.E. McCarthy, M.C. Standage (Eds.), Electronic and Atomic Collisions, Invited Papers of the ICPEAC, Vol. XVII, Adam Hilger, Bristol, 1991, p. 351.
[54] R. Dörner, J. Ullrich, O. Jagutzki, S. Lencinas, H. Schmidt-Böcking, R.E. Olson, Z. Phys. D 21 (1991) 57.
[55] R. Dörner, J. Ullrich, R.E. Olson, O. Jagutzki, H. Schmidt-Böcking, Phys. Rev. A 47 (1993) 3845.
[56] J. Ullrich, R. Dörner, S. Lencinas, O. Jagutzki, H. Schmidt-Böcking, U. Buck, Nucl. Instr. and Meth. B 61 (1991) 415.
[57] J. Ullrich, R. Dörner, O. Jagutzki, S. Lencinas, A. Gensmantel, E. Forberich, K. Ullmann, R.E. Olson, H. Schmidt-Böcking, SHIM, Book of Invited Talks, 1992.
[58] C. Meng, R.E. Olson, R. Dörner, J. Ullrich, H. Schmidt-Böcking, J. Phys. B 26 (1993) 3387.
[59] A. Gensmantel, J. Ullrich, R. Dörner, R.E. Olson, K. Ullmann, E. Forberich, S. Lencinas, H. Schmidt-Böcking, Phys. Rev. A 45 (1992) 4572.*
[60] E. Forberich, R. Dörner, J. Ullrich, R.E. Olson, K. Ullmann, A. Gensmantel, J. Phys. B 24 (1991) 3613.
[61] S. Lencinas, J. Ullrich, R. Dörner, R.E. Olson, W. Wolff, L. Spielberger, S. Hagmann, M. Horbatsch, C.L. Cocke, H. Schmidt-Böcking, J. Phys. B 27 (1994) 287.
[62] V. Frohne, S. Cheng, R. Ali, M. Raphaelian, C.L. Cocke, R.E. Olson, Phys. Rev. Lett. 71 (1993) 696.
[63] R. Ali, V. Frohne, C.L. Cocke, M. Stöckli, S. Cheng, M.L.A. Raphaelian, Phys. Rev. Lett. 69 (1992) 2491.***
[64] O. Jagutzki, Dissertation Unversität Frankfurt, 1994, unpublished.
[65] P. Jardin, J.P. Grandin, A. Cassimi, J.P. Lemoigne, A. Gosseling, X. Husson, D. Hennecart, A. Lepoutre, in AIP Conference Proceedings, Vol. 274, AIP, New York, 1993, p. 291.
[66] R. Dörner, V. Mergel, R. Ali, U. Buck, C.L. Cocke, K. Froschauer, O. Jagutzki, S. Lencinas, W.E. Meyerhof, S. Nüttgens, R.E. Olson, H. Schmidt-Böcking, L. Spielberger, K. Tökesi, J. Ullrich, M. Unverzagt, W. Wu, Phys. Rev. Lett. 72 (1994) 3166.***
[67] V. Mergel, Diplomarbeit Universität Frankfurt, 1994.
[68] V. Mergel, Ph.D. Thesis, Universität Frankfurt, Shaker, Aachen, 1996.*
[69] V. Mergel, R. Dörner, M. Achler, Kh. Khayyat, S. Lencinas, J. Euler, O. Jagutzki, S. Nüttgens, M. Unverzagt, L. Spielberger, W. Wu, R. Ali, J. Ullrich, H. Cederquist, A. Salin, R.E. Olson, Dž. Belkić, C.L. Cocke, H. Schmidt-Böcking, Phys. Rev. Lett. 79 (1997) 387.***
[70] R. Dörner, H. Bräuning, J.M. Feagin, V. Mergel, O. Jagutzki, L. Spielberger, T. Vogt, H. Khemliche, M.H. Prior, J. Ullrich, C.L. Cocke, H. Schmidt-Böcking, Phys. Rev. A 57 (1998) 1074.
[71] S.D. Kravis, M. Abdallah, C.L. Cocke, C.D. Lin, M. Stöckli, B. Walch, Y. Wang, R.E. Olson, V.D. Rodriguez, W. Wu, M. Pieksma, N. Watanabe, Phys. Rev. A 54 (1996) 1394.
[72] M. Abdallah, S. Kravis, C.L. Cocke, Y. Wang, V.D. Rodriguez, M. Stöckli, Phys. Rev. A 56 (1997) 2000.
[73] R. Dörner, H. Khemliche, M.H. Prior, C.L. Cocke, J.A. Gary, R.E. Olson, V. Mergel, J. Ullrich, H. Schmidt-Böcking, Phys. Rev. Lett. 77 (1996) 4520.
[74] M. Abdallah, C.L. Cocke, W. Wolff, H. Wolf, S.D. Kravis, M. Stöckli, E. Kamber, Phys. Rev. Lett. 81 (1998) 3627.
[75] M. Abdallah, W. Wolff, H. Wolf, C.L. Cocke, M. Stöckli, Phys. Rev. A 58 (1998) R3379.
[76] R. Moshammer, J. Ullrich, M. Unverzagt, W. Schmidt, P. Jardin, R.E. Olson, R. Mann, R. Dörner, V. Mergel, U. Buck, H. Schmidt-Böcking, Phys. Rev. Lett. 73 (1994) 3371.***
[77] R. Moshammer, M. Unverzagt, W. Schmitt, J. Ullrich, H. Schmidt-Böcking, Nucl. Instr. and Meth. B 108 (1996) 425.
[78] O. Jagutzki, V. Mergel, K. Ullmann-Pfleger, L. Spielberger, U. Meyer, R. Dörner, H. Schmidt-Böcking, Nucl. Instr. and Meth., in: SPIE-Proc. No. 3438 'Imaging Spectroscopy IV' (Proceedings of the International Symposium on Optical Science, Engineering, and Instrumentation), San Diego, CA, USA, 19–24.7.98, 1998, in print.

[79] R. Moshammer, J. Ullrich, H. Kollmus, W. Schmitt, M. Unverzagt, O. Jagutzki, V. Mergel, H. Schmidt-Böcking, R. Mann, C.J. Woods, R.E. Olson, Phys. Rev. Lett. 77 (1996) 1242.***
[80] M. Schulz, R. Moshammer, W. Schmitt, J. Ullrich, Phys. Rev. Lett. 1999, submitted for publication.
[81] R. Moshammer, J. Ullrich, W. Schmitt, H. Kollmus, A. Cassimi, R. Dörner, R. Dreizler, O. Jagutzki, S. Keller, H.-J. Lüdde, R. Mann, V. Mergel, R.E. Olson, T. Prinz, H. Schmidt-Böcking, L. Spielberger, Phys. Rev. Lett. 79 (1997) 3621.
[82] M. Unverzagt, R. Moshammer, W. Schmitt, R.E. Olson, P. Jardin, V. Mergel, J. Ullrich, H. Schmidt-Böcking, Phys. Rev. Lett. 76 (1996) 1043.*
[83] V.D. Rodriguez, Y.D. Wang, C.D. Lin, Phys. Rev. A 52 (1995) R9.
[84] Th. Weber, Master's Thesis, Diploma Thesis, University Frankfurt, 1998, unpublished.
[85] L.C. Tribedi, P. Richard, Y.D. Wang, C.D. Lin, R.E. Olson, Phys. Rev. Lett. 77 (1996) 1996.
[86] L.C. Tribedi, P. Richard, Y.D. Wang, C.D. Lin, R.E. Olson, L. Gulyas, Phys. Rev. A 58 (1998) 3626.
[87] L.C. Tribedi, P. Richard, Y.D. Wang, C.D. Lin, R.E. Olson, Phys. Rev. Lett. A 58 (1998) 3689.
[88] W. Wu, K.L. Wong, E.C. Montenegro, R. Ali, C.Y. Chen, C.L. Cocke, R. Dörner, V. Frohne, J.P. Giese, V. Mergel, W.E. Meyerhof, M. Raphaelian, H. Schmidt-Böcking, B. Walch, Phys. Rev. A 55 (1997) 2771.
[89] W. Wu, R. Ali, C.L. Cocke, V. Frohne, J.P. Giese, B. Walch, K.L. Wong, R. Dörner, V. Mergel, H. Schmidt-Böcking, W.E. Meyerhof, Phys. Rev. Lett. 72 (1994) 3170.**
[90] H. Schmidt-Böcking, C.L. Cocke, R. Dörner, O. Jagutzki, T. Kambara, V. Mergel, R. Moshammer, M.H. Prior, L. Spielberger, W. Schmitt, K. Ullmann, M. Unverzagt, J. Ullrich, W. Wu, in: S.M. Shafroth, J.C. Austin (Eds.), Accelerator-Based Atomic Physics Techniques and Applications, American Institute of Physics, Woodbury, New York, 1996, pp. 723–745.
[91] T. Vogt, Diploma Thesis, University Frankfurt, 1995, unpublished.
[92] R. Dörner, T. Vogt, V. Mergel, H. Khemliche, S. Kravis, C.L. Cocke, J. Ullrich, M. Unverzagt, L. Spielberger, M. Damrau, O. Jagutzki, I. Ali, B. Weaver, K. Ullmann, C.C. Hsu, M. Jung, E.P. Kanter, B. Sonntag, M.H. Prior, E. Rotenberg, J. Denlinger, T. Warwick, S.T. Manson, H. Schmidt-Böcking, Phys. Rev. Lett. 76 (1996) 2654.
[93] L. Spielberger, O. Jagutzki, R. Dörner, J. Ullrich, U. Meyer, V. Mergel, M. Unverzagt, M. Damrau, T. Vogt, I. Ali, Kh. Khayyat, D. Bahr, H.G. Schmidt, R. Frahm, H. Schmidt-Böcking, Phys. Rev. Lett. 74 (1995) 4615.***
[94] G.W. Fraser, Nucl. Instr. and Meth. A 221 (1984) 115.
[95] G.W. Fraser, M.A. Barstow, J.F. Pearson, Nucl. Instr. and Meth. in Phys. Res. A 273 (1988) 667–672.
[96] G.W. Fraser, M.A. Barstow, J.F. Pearson, Nucl. Instr. and Meth. in Phys. Res. A 273 (1988) 667–672.
[97] J. Ullrich, Ph.D. Thesis, Institut für Kernphysik, J.W. Goethe Universität, 1987.
[98] R. Dörner, J. Ullrich, H. Schmidt-Böcking, GSI Report, GSI-91-28, 1991.
[99] V. Frohne, S. Cheng, R. Ali, M. Raphaelian, C.L. Cocke, R.E. Olson, Phys. Rev. A 53 (1996) 2407.
[100] W. Wu, J.P. Giese, Z. Chen, R. Ali, C.L. Cocke, P. Richard, M. Stöckli, Phys. Rev. A 50 (1994) 502.
[101] D.R. Miller, in: G. Scoles, D. Bassi, U. Buck, D. Lainé (Eds.), Atomic and Molecular Beam Methods, Vol. 14, Oxford University Press, New York, 1988.
[102] L. Pedemonte, G. Bracco, R. Tatarek, Phys. Rev. A 59 (1999) 3084.
[103] G. Brusdeylins, J.P. Toennies, R. Vollmer, Perugia, 1989, p. 98.
[104] L. Spielberger, O. Jagutzki, B. Krässig, U. Meyer, Kh. Khayyat, V. Mergel, Th. Tschentscher, Th. Buslaps, H. Bräuning, R. Dörner, T. Vogt, M. Achler, J. Ullrich, D.S. Gemmel, H. Schmidt-Böcking, Phys. Rev. Lett. 76 (1996) 4685.
[105] O. Jagutzki, L. Spielberger, R. Dörner, S. Nüttgens, V. Mergel, H. Schmidt-Böcking, J. Ullrich, R.E. Olson, U. Buck, Zeitschrift für Physik D 36 (1996) 5.
[106] H.T. Schmidt, H. Cederquist, R. Schuch, L. Bagge, A. Kalleberg, J. Hilge, K.G. Rensfelt, V. Mergel, M. Achler, R. Dörner, O. Jagutzki, H. Schmidt-Böcking, J. Ullrich, H. Reich, M. Unverzagt, W. Schmitt, R. Moshammer, Hyperfine Interactions 108 (1997) 339–354.
[107] W.C. Wiley, I.H. McLaren, Rev. Sci. Instr. 26 (1955) 1150.
[108] V. Mergel, R. Dörner, J. Ullrich, O. Jagutzki, S. Lencinas, S. Nüttgens, L. Spielberger, M. Unverzagt, C.L. Cocke, R.E. Olson, M. Schulz, U. Buck, E. Zanger, W. Theisinger, M. Isser, S. Geis, H. Schmidt-Böcking, Phys. Rev. Lett. 74 (1995) 2200.***

[109] A. Cassimi, S. Duponchel, X. Flechard, P. Jardin, P. Sortais, D. Hennecart, R.E. Olson, Phys. Rev. Lett. 76 (1996) 3679.
[110] X. Flechard, S. Duponchel, L. Adoit, A. Cassimi, P. Roncin, D. Hennecart, J. Phys. B 30 (1997) 3697.
[111] R. Dörner, V. Mergel, L. Spielberger, O. Jagutzki, H. Schmidt-Böcking, J. Ullrich, Phys. Rev. A 57 (1998) 312.
[112] R. Dörner, V. Mergel, L. Zhaoyuan, J. Ullrich, L. Spielberger, R.E. Olson, H. Schmidt-Böcking, J. Phys. B 28 (1995) 435.
[113] A.T.J.B. Eppkin D.H. Parker, Rev. Sci. Instr. 69 (9) (1997) 3477.
[114] H. Helm, N. Bjerre, M.J. Dyer, D.L. Huestis, M. Saeed, Phys. Rev. Lett. 70 (1993) 3221.
[115] R. Dörner, J. Feagin, C.L. Cocke, H. Bräuning, O. Jagutzki, M. Jung, E.P. Kanter, H. Khemliche, S. Kravis, V. Mergel, M.H. Prior, H. Schmidt-Böcking, L. Spielberger, J. Ullrich, M. Unverzagt, T. Vogt, Phys. Rev. Lett. 77 (1996) 1024, see also erratum in Phys. Rev. Lett. 78 (1997) 2031.***
[116] T. Vogt, R. Dörner, O. Jagutzki, C.L. Cocke, J. Feagin, M. Jung, E.P. Kanter, H. Khemliche, S. Kravis, V. Mergel, L. Spielberger, J. Ullrich, M. Unverzagt, H. Bräuning, U. Meyer, H. Schmidt-Böcking, in: C.T. Whelan, H.R.J. Walters (Eds.), Proceedings of the Euroconference Ionization Coincidence Spectroscopy, Plenum Press, New York, 1997.
[117] V. Mergel, M. Achler, R. Dörner, Kh. Khayyat, T. Kambara, Y. Awaya, V. Zoran, B. Nyström, L. Spielberger, J.H. McGuire, J. Feagin, J. Berakdar, Y. Azuma, H. Schmidt-Böcking, Phys. Rev. Lett. 80 (1998) 5301.**
[118] Kh. Khayyat, Ph.D. Thesis, University Frankfurt, 1998, unpublished.
[119] Kh. Khayyat, Th. Weber, R. Dörner, M. Achler, V. Mergel, L. Spielberger, O. Jagutzki, U. Meyer, J. Ullrich, R. Moshammer, H. Knudsen, U. Mikkelsen, P. Aggerholm, V.D. Roderiguez, S.F.C. O'Rourke, S.P. Moeller, R.E. Olson, P. Fainstein, J.H. McGuire, H. Schmidt-Bcking, J. Phys. B 32 (1999) L73.
[120] H. Kollmus, W. Schmitt, R. Moshammer, M. Unverzagt, J. Ullrich, Nucl. Instr. and Meth. B 124 (1987) 377.
[121] R. Moshammer, J. Ullrich, M. Unverzagt, W. Schmitt, P. Jardin, R.E. Olson, R. Dörner, V. Mergel, H. Schmidt-Böcking, Nucl. Instr. and Meth. B 107 (1996) 62.
[122] R. Moshammer, J. Ullrich, H. Kollmus, W. Schmitt, M. Unverzagt, H. Schmidt-Böcking, C.J. Wood, R.E. Olson, Phys. Rev. A 56 (1997) 1351.**
[123] H.P Bräuning, R. Dörner, C.L. Cocke, M.H. Prior, B. Krässig, A. Bräuning-Demian, K. Carnes, S. Dreuil, V. Mergel, P. Richard, J. Ullrich, H. Schmidt-Böcking, J. Phys. B 30 (1997) L649.
[124] V. Mergel, O. Jagutzki, L. Spielberger, K. Ullmann-Pfleger, R. Dörner, H. Schmidt-Böcking, Conference Proceedings of the MRS, 1997.
[125] A. Martin, P. Jenlinsky, M. Lampton, R.F. Malina, Rev. Sci. Instr. 52 (7) (1981) 1067.
[126] G. Battistone, P. Campa, V. Chiarella, U. Denni, E. Iarocci, G. Nicoletti, Nucl. Instr. and Meth. 202 (1982) 459.
[127] S.E. Sobottka, M.B. Williams, IEEE Trans. Nucl. Sci. 35 (1988) 348.
[128] I. Ali, Ph.D. Thesis, University Frankfurt, 1996, unpublished.
[129] R. Dörner, H. Bräuning, O. Jagutzki, V. Mergel, M. Achler, R. Moshammer, J. Feagin, A. Bräuning-Demian, L. Spielberger, J.H. McGuire, M.H. Prior, N. Berrah, J. Bozek, C.L. Cocke, H. Schmidt-Böcking, Phys. Rev. Lett. 81 (1998) 5776.
[130] M. Schulz, J. Modern Phys. B 9 (1995) 3269.
[131] W.C. Keever, E. Everhart, Phys. Rev. A 43 (1966) 150.
[132] V. Mergel, R. Dörner, J. Ullrich, O. Jagutzki, S. Lencinas, S. Nüttgens, L. Spielberger, M. Unverzagt, C.L. Cocke, R.E. Olson, M. Schulz, U. Buck, H. Schmidt-Böcking, Nucl. Instr. and Meth. B 96 (1995) 593.
[133] T. Kambara, J.Z. Tang, Y. Awaya, B.D. dePaola, O. Jagutzki, Y. Kanai, M. Kimura, T.M. Kojima, V. Mergel, H. Schmidt-Böcking, I. Shimamura, J. Phys. B 28 (1995) 4593.
[134] M. Abdallah, C.L. Cocke, S. Kravis, E.C. Montenegro, R. Moshammer, L. Saleh, J. Ullrich, S.L. Varghese, W. Wolff, H. Wolff, in: J.L. Duggan, I.L. Morgan (Eds.), Applications of Accelerators in Research Industry, AIP Conference Proceedings, Vol. 392, 1997, 209.
[135] R.E. Olson, Electronic Atomic Collisions, Elsevier Science Publishers, Amsterdam, 1988, p. 271.
[136] R.E. Olson, A. Salop, Phys. Rev. A 16 (1977) 531.
[137] M.A. Abdallah, W. Wolff, H.E. Wolf, E. Sidky, E.Y. Kamber, M. Stöckli, C.D. Lin, C.L. Cocke, Phys. Rev. A 58 (1998) 4373.

[138] E. Ertürk, L. Spielberger, M. Achler, L. Schmidt, R. Dörner, Th. Weber, O. Jagutzki, V. Mergel, Kh. Khayyat, A. Lahmam-Bennani, H. Schmidt-Böcking, in: H.H. Macek, C.T. Whelan, R.M. Dreizler, in H.R.J. Walters et al. (Eds.), New Directions in Atomic Physics, Plenum Press, New York, 1999, p. 179.
[139] A. Dorn, R. Moshammer, C.D. Schröter, T. Zouros, W. Schmitt, H. Kollmus, R. Mann, J. Ullrich, in H.R.J. Walters et al. (Eds), New Directions in Atomic Physics, Plenum Press, New York, 1999, p. 203.
[140] W. Wu, C.L. Cocke, J.P. Giese, F. Melchert, M.L.A. Raphaelian, M. Stöckli, Phys. Rev. Lett. 75 (1995) 1054.
[141] S. Ovchinnikov J. Macek, Phys. Rev. Lett. 75 (1995) 2474.
[142] M. Pieksma, S.Y. Ovchinnikov, J. Phys. B 27 (1994) 4573.
[143] A. Barany, S. Ovchinnikov, Phys. Scr. T 46 (1993) 243.
[144] E.A. Solovev, Phys. Rev. A 42 (1990) 1331.
[145] J. Macek, S.Yu. Ovchinnikov, Phys. Rev. Lett. 80 (1998) 2298.*
[146] R.E. Olson, Phys. Rev. A 27 (1983) 1871.
[147] R.E. Olson, Phys. Rev. A 33 (1986) 4397.
[148] R.E. Olson, T.J. Gay, H.G. Berry, E.B. Hale, V.D. Irby, Phys. Rev. Lett. 59 (1987) 36.
[149] E.Y. Kamber, C.L. Cocke, S. Cheng, S.L. Varghese, Phys. Rev. Lett. 60 (1988) 2026.***
[150] E.Y. Kamber, C.L. Cocke, S. Cheng, J.H. McGuire, S.L. Varghese, J. Phys. B 21 (1988) L455.
[151] J.P. Giese, E. Horsdal, Phys. Rev. Lett. 60 (1988) 2018.
[152] J.P. Giese, E. Horsdal, Nucl. Instr. and Meth. B 40/41 (1989) 201.
[153] F.G. Kristensen, E. Horsdal-Pedersen, J. Phys. B 23 (1990) 4129.
[154] R.E. Olson, J. Ullrich, R. Dörner, H. Schmidt-Böcking, Phys. Rev. A 40 (1989) 2843.*
[155] H. Schmidt-Böcking, R. Dörner, J. Ullrich, J. Euler, H. Berg, E. Forberich, S. Lencinas, O. Jagutzki, A. Gensmantel, K. Ullmann, R.D. DuBois, F. Jiazhen, R.E. Olson, A. Gonzales, S. Hagmann, in: D. Bereny, G. Hock (Eds.), High-Energy Ion-Atom-Collisions, Springer, Berlin, 1991, p. 268.
[156] W.R. DeHaven, C. Dilley, A. Landers, E.Y. Kamber, C.L. Cocke, Phys. Rev. A 57 (1998) 292.
[157] H. Fukuda, I. Shimamura, L. Vegh, T. Watanabe, Phys. Rev. A 44 (1991) 1565.
[158] H. Fukuda, T. Watanabe, I. Shimamura, L. Vegh, Nucl. Instr. and Meth., 1991.
[159] R.E. Olson, J. Ullrich, H. Schmidt-Böcking, Phys. Rev. A 39 (1989) 5572.
[160] R. Dörner, V. Mergel, L. Zaoyuan, J. Ullrich, L. Spielberger, R.E. Olson, H. Schmidt-Böcking, J. Phys. B 28 (1994) 435.
[161] A. Salin, J. Phys. B 22 (1989) 3901.
[162] S.F.C. ORourke, I. Shimamura, D.S.F. Crothers, Proc. R. Soc. London 452 (1996) 175.
[163] Y.D. Wang, L.C. Tribedi, P. Richard, C.L. Cocke, V.D. Rodriguez, C.D. Lin, J. Phys. B 29 (1996) L203.
[164] C.J. Wood, C.R. Feeler, R.E. Olson, Phys. Rev. A 56 (1997) 3701.
[165] C.F. von Weizäcker, Zeitschrift für Physik 88 (1934) 612.
[166] E.J. Williams, Phys. Rev. 45 (1934) 729.
[167] C.J. Wood, R.E. Olson, W. Schmitt, R. Moshammer, J. Ullrich, Phys. Rev. A 56 (1997) 3746.
[168] C. Bertulani, G. Baur, Phys. Rep. 163 (1988) 299.
[169] S. Keller, H.J. Lüdde, R. Dreizler, Phys. Rev. A 55 (1997) 4215.
[170] J. Ullrich, R. Moshammer, M. Unverzagt, W. Schmidt, P. Jardin, R.E. Olson, R. Dörner, V. Mergel, H. Schmidt-Böcking, Nucl. Instr. and Meth. B 98 (1995) 375.
[171] W. Schmitt, Ph.D. Thesis, University Frankfurt, 1998, unpublished.
[172] W. Schmitt, R. Moshammer, F.S.C. O'Rourke, H. Kollmus, L. Sakardi, R. Mann, S. Hagmann, R.E. Olson, J. Ullrich, Phys. Rev. Lett. 81 (1998) 4337.
[173] S.F.C. ORourke, D.S.F. Crothers, J. Phys. B 30 (1997) 2443.
[174] S.F.C. ORourke, R. Moshammer, J. Ullrich, J. Phys. B 30 (1997) 5281.
[175] R.D. DuBois, N. Stolterfoht, R.D. Rivarola, Springer, Berlin, 1997.
[176] J. Ullrich, R. Moshammer, H. Berg, R. Mann, H. Tawara, R. Dörner, J. Euler, H. Schmidt-Böcking, S. Hagmann, C.L. Cocke, M. Unverzagt, S. Lencinas, V. Mergel, Phys. Rev. Lett. 71 (1993) 1697.*
[177] J.H. McGuire, N. Berrah, R.J. Bartlett, J.A.R. Samson, J.A. Tanis, C.L. Cocke, A.S. Schlachter, J. Phys. B 28 (1995) 913.

[178] B. Skogvall, G. Schiwietz, Phys. Rev. Lett. 65 (1990) 3265.
[179] J.F. Reading, A.L. Ford, X. Fang, Phys. Rev. Lett. 62 (1989) 245.
[180] X. Fang, J.F. Reading, Nucl. Instr. and Meth. B 53 (1991) 453.
[181] J. Ullrich, R. Dörner, O. Jagutzki, S. Lencinas, A. Gensmantel, E. Forberich, K. Ullmann, R.E. Olson, H. Schmidt-Böcking, Radiation Effects and Defects in Solids, 1993, p. 77.
[182] R. Gayet, A. Salin, in: D. Bereny, G. Hock (Eds.), High-Energy Ion-Atom-Collisions and Proceedings of the 4th Workshop, Debrecen, September 1990, Lecture Notes in Physics, Vol. 376, Springer, Berlin, Heidelberg, 1991, 1990.
[183] J. Ullrich, R. Dörner, H. Berg, C.L. Cocke, J. Euler, K. Froschauer, S. Hagmann, O. Jagutzki, S. Lencinas, R. Mann, V. Mergel, R. Moshammer, H. Schmidt-Böcking, H. Tawara, M. Unverzagt, Nucl. Instr. and Meth. B 87 (1994) 70.
[184] P. Jardin, A. Cassimi, J.P. Grandin, H. Rothard, J.P. Lemoigne, D. Hennecart, X. Husson, A. Lepoutre, Nucl. Instr. and Meth. B 98 (1995) 363.
[185] P. Jardin, A. Cassimi, J.P. Grandin, H. Rothard, J.P. Lemoigne, D. Hennecart, X. Husson, A. Lepoutre, Nucl. Instr. and Meth. B 107 (1996) 41.
[186] A.L. Ford, J.F. Reading, Nucl. Instr. and Meth. B 10/11 (1985) 12.
[187] A.L. Ford, J.F. Reading, J. Phys. B 21 (1988) L685.
[188] A.L. Ford, J.F. Reading, J. Phys. B 23 (1990) 2567.
[189] A.L. Ford, J.F. Reading, Nucl. Instr. and Meth. B 56/57 (1991) 196.
[190] J.F. Reading, A.L. Ford, Phys. Rev. Lett. 58 (1987) 543.
[191] J. Ullrich, R. Moshammer, R. Dörner, Physikalische Blätter 54 (1998) 140.
[192] J.H. McGuire, N.C. Deb, Y. Aktas, Phys. Rev. A 38 (1988) 3333–3338.
[193] L.H. Thomas, Proc. Roy. Soc. A 114 (1927) 561–576.*
[194] J. Palinkas, R. Schuch, H. Cederquist, O. Gustafsson, Phys. Rev. Lett. 63 (22) (1989) 2464–2467.
[195] E. Horsdal, B. Jensen, K.O. Nielsen, Phys. Rev. Lett. 57 (12) (1986) 1414–1417.*
[196] R. Gayet, Jou. de Phys. 1 C (1989) C1–53–70.
[197] R. Gayet, A. Salin, Nucl. Instr. and Meth. B 56/57 (1991) 82–85.*
[198] J.S. Briggs, K. Taulbjerg, J. Phys. B 12 (1979) 2565–2573.
[199] T. Ishihara, J.H. McGuire, Phys. Rev. A 38 (1988) 3310–3318.
[200] J.H. McGuire, J.C. Straton, W.J. Axmann, T. Ishihara, E. Horsdal-Pedersen, Phys. Rev. Lett. 62 (1989) 2933.
[201] K.M. Dunseath, D.S.F. Crothers, J. Phys. B 24 (1991) 5003.
[202] D.R. Bates, G. Griffin, Proc. Phys. Soc. London A 66 (1953) 961.
[203] D.R. Bates, G. Griffin, Proc. Phys. Soc. London A 67 (1954) 663.
[204] D.R. Bates, G. Griffin, Proc. Phys. Soc. London A 68 (1955) 90.
[205] H.-P. Hülskötter, B. Feinberg, W.E. Meyerhof, A. Belkacem, J.R. Alonso, L. Blumenfeld, E.A. Dillard, H. Gould, G.F. Krebs, M.A. McMahan, M.E. Rhoades-Brown, B.S. Rude, J. Schweppe, D.W. Spooner, K. Street, P. Thieberger, H.E. Wegner, Phys. Rev. 44 (1991) 1712.
[206] E.C. Montenegro, W.E. Meyerhof, Phys. Rev. A 44 (1991) 7229.
[207] E.C. Montenegro, W.E. Meyerhof, Phys. Rev. A 46 (1992) 5506.
[208] E.C. Montenegro, W.S. Melo, W.E. Meyerhof, A.G. dePinho, Phys. Rev. Lett. 69 (1992) 3033.**
[209] E.C. Montenegro, A. Belkacem, D.W. Spooner, W.E. Meyerhof, M.B. Shah, Phys. Rev. A 47 (1993) 1045.
[210] N.M. Kabachnik, J. Phys. 26 (1993) 3803.
[211] T.J.M. Zouros, D.H. Lee, P. Richard, Phys. Rev. Lett. 62 (1989) 2261.
[212] R. Dörner, V. Mergel, R. Ali, U. Buck, C.L. Cocke, K. Froschauer, O. Jagutzki, S. Lencinas, W.E. Meyerhof, S. Nüttgens, R.E. Olson, H. Schmidt-Böcking, L. Spielberger, K. Tökesi, J. Ullrich, M. Unverzagt, W. Wu, Nucl. Instr. and Meth. B 98 (1995) 367.
[213] M.S. Gravielle, J.E. Miraglia, Phys. Rev. A 45 (1992) 2965, four body impulse.
[214] H.O. Folkerts, R. Hoekstra, L. Meng, R.E. Olson, W. Fritsch, R. Morgenstern, H.P. Summers, J. Phys. B 26 (1993) L619–L624.
[215] T.J.M. Zouros, D. Schneider, N. Stolterfoht, Phys. Rev. A 35 (1987) 1963.
[216] K. Tökesi, G. Hock, J. Phys. B 29 (1996) L119.

[217] D.S.F. Crothers, R. McCarroll, J. Phys. B 20 (1987) 2835.
[218] N.C. Deb, D.S.F. Crothers, J. Phys. B 23 (1990) L799.
[219] R. Shingal, C.D. Lin, J. Phys. B 24 (1991) 251.
[220] T.C. Theisen, J.H. McGuire, Phys. Rev. A 20 (1979) 1406.
[221] A.E. Martinez, R. Gayet, J. Hanssen, R.D. Rivarola, J. Phys. 27 (1994) L375.
[222] R. Gayet, R.D. Rivarola, A. Salin, J. Phys. B 14 (1981) 2421.
[223] M. Gosh, C.R. Madal, S.C. Mukharjee, J. Phys. B 18 (1985) 3797.
[224] G. Deco, N. Grün, Zeitschrift für Physik D 18 (1991) 339.
[225] R. Gayet, J. Hanssen, J. Martinez, R.D. Rivarola, Zeitschrift für Physik D 18 (1991) 345.
[226] W. Fritsch, J. Phys. B 27 (1994) 3461.
[227] M. Kimura, J. Phys. B 21 (1988) L19.
[228] C. Harel, A. Salin, J. Phys. B 13 (1980) 785.
[229] K. Gramlich, N. Grün, W. Scheidt, J. Phys. B 22 (1989) 2567.
[230] K.R. Sandhya, J.D. Garcia, J. Phys. B 16 (1980) 2837.
[231] K.J. Schaudt, N.H. Kwong, J.D. Garcia, Phys. Rev. A 43 (1991) 2294.
[232] W. Stich, H.J. Lüdde, R.M. Dreizler, J. Phys. B 18 (1985) 1195.
[233] C. Chaudhuri, S. Sanyal, T.K. RaiDastidar, Phys. Rev. A 52 (1995) 1137.
[234] Dz. Belkic, Phys. Rev. A 47 (1993) 189, CB1 four body.
[235] Dz. Belkic, J. Phys. B 26 (1993) 497.
[236] Dz. Belkic, I. Mancev, Phys. Scr. 47 (1993) 18.
[237] Dz. Belkic, I. Mancev, Phys. Scr. 45 (1993) 35.
[238] Dz. Belkic, Phys. Rev. 47 (1993) 3824.
[239] R. Gayet, J. Hanssen, J. Martinez, R.D. Rivarola, Nucl. Instr. and Meth. B 86 (1994) 158.
[240] Dž Belkić, A. Salin, J. Phys. B 11 (1978) 3905–3911.
[241] Dz. Belkic, A. Salin, J. Phys. B 11 (1978) 3905.
[242] R. Schuch, E. Justiniano, H. Vogt, G. Deco, N. Grün, J. Phys. B 24 (1991) L133.
[243] H.-P. Hülskötter, W.E. Meyerhof, E.A. Dillard, N. Guardala, Phys. Rev. Lett. 63 (1989) 1938.
[244] H.-P. Hülskötter, B. Feinberg, W.E. Meyerhof, A. Belkacem, J.R. Alonso, L. Blumenfeld, E.A. Dillard, H. Gould, G.F. Krebs, M.A. McMahan, M.E. Rhoades-Brown, B.S. Rude, J. Schweppe, D.W. Spooner, K. Street, P. Thieberger, H.E. Wegner, Phys. Rev. 44 (1991) 1712.
[245] Dz. Belkic, Phys. Rev. A 47 (1993) 189.
[246] O. Heber, R.L. Watson, G. Sampoll, Nucl. Instr. and Meth. B 56 (1991) 232.
[247] J.C. Levin, C. Biederman, H.O. Cederquist, C.S. Short, I.A. Sellin, Nucl. Instr. and Meth. B 40/41 (1989) 402.
[248] J.C. Levin, R.T. Short, C. Biedermann, H. Cederquist, O.S. Elston, I.A. Sellin, Phys. Rev. A 49 (1994) 228.
[249] J. Ullrich, C.L. Cocke, S. Kelbch, R. Mann, P. Richard, H. Schmidt-Böcking, J. Phys. B 17 (1984) L785.
[250] A. Gosselin, P. Boduch, D. Hennecart, S. Hicham, X. Husson, D. Lecler, A. Lepoutr, A. Cassimi, J.P. Grandin, J. Phys. III France 9 (1994) 1765.
[251] M. Horbatsch, J. Phys. B 22 (1989) L639.
[252] M. Horbatsch, Phys. Lett. A 137 (1989) 466.
[253] A.D. Gonzales, S. Hagmann, T.B. Quinteros, B. Krässig, R. Koch, A. Skutlartz, H. Schmidt-Böcking, J. Phys. B 23 (1990) L303.
[254] N. Stolterfoht, C.C. Havener, R.A. Paneuf, J.K. Swenson, S.M. Shafroth, F.W. Meyer, Phys. Rev. Lett. 57 (1986) 74.
[255] A. Niehaus, in: R. Marrus (Ed.), Physic of Highly-Ionized Atoms, Vol. 267, Plenum Press, New York, 1989.
[256] M.L.A. Raphaelian, M.P. Stöckli, W. Wu, C.L. Cocke, Phys. Rev. A 51 (1995) 1304.
[257] M.A. Abdallah, W. Wolff, H.E. Wolf, E.Y. Kamber, M. Stöckli, C.L. Cocke, Phys. Rev. A 58 (1998) 2911.
[258] L. Spielberger, O. Jagutzki, R. Dörner, K. Froschauer, A. Gensmantel, H. Schmidt-Böcking, J. Ullrich, U. Buck, in: C.T. Whelan et al. (Eds.), (*e*,2*e*) and Related Processes, Kluwer Academic Publishers, Dordrecht, 1993, pp. 119–129.
[259] C.D. Opal, E.C. Beaty, W.K. Peterson, At. Data 4 (1972) 209.
[260] N. Oda, Rad. Res. 64 (1975) 80.

[261] L. Spielberger, H. Bräuning, A. Muthig, J.Z. Tang, J. Wang, Y. Qui, R. Dörner, O. Jagutzki, Th. Tschentscher, V. Honkimäki, V. Mergel, M. Achler, Th. Weber, Kh. Khayyat, J. Burgdörfer, J. McGuire, H. Schmidt-Böcking, Phys. Rev. 59 (1999) 371.**
[262] V. Schmidt, Electron Spectrometry of Atoms Using Synchrotron Radiation, Cambridge Monographs on Atomic, Molecular and Chemical Physics, Vol. 6, Cambridge University Press, Cambridge, 1997.
[263] G.H. Wannier, Phys. Rev. 90 (1953) 817.
[264] H. Kossmann, V. Schmidt, T. Andersen, Phys. Rev. A 60 (1988) 1266.
[265] J.C. Levin, D.W. Lindle, N. Keller, R.D. Miller, Y. Azuma, N. Berrah Mansour, H.G. Berry, I.A. Sellin, Phys. Rev. Lett. 67 (1991) 968.*
[266] J.C. Levin, I.A. Sellin, B.M. Johnson, D.W. Lindle, R.D. Miller, N. Berrah, Y. Azuma, H.G. Berry, D.H. Lee, Phys. Rev. A 47 (1993) R16.
[267] J. C. Levin, G. B. Armen, I.A. Sellin, Phys. Rev. Lett. 76 (1996) 1220.
[268] L. Spielberger, O. Jagutzki, R. Dörner, V. Mergel, U. Meyer, Kh. Khayyat, T. Vogt, M. Achler, H. Schmidt-Böcking, J. Ullrich, M. Unverzagt, B. Krässig, M. Jung, E.P. Kanter, D.S. Gemmell, M.H. Proir, H. Khemliche, C.L. Cocke, in: J.L. Duggan, I.L. Morgan (Eds.), Applications of Accelerators in Research and Industry, AIP Conference Proceedings, Vol. 392, 1997, 213.
[269] J.A.R. Samson, W.C. Stolte, Z.X. He, J.N. Cutler, Y. Lu, R.J. Bartlett, Phys. Rev. A 57 (1998) 1906.
[270] J.Z. Tang, I. Shimamura, Phys. Rev. A 52 (1995) 1.
[271] M. Pont, R. Shakeshaft, Phys. Rev. A 51 (1995) 494.
[272] K.W. Meyer, J.L. Bohn, C.H. Green, B.D. Esry, J. Phys. B 30 (1997) L641.
[273] A. Kheifets, I. Bray, Phys. Rev. A 57 (1998) 2590.
[274] M.S. Pindzola, F. Robicheaux, Phys. Rev. A 57 (1998) 318.
[275] Y. Qiu, J.Z. Tang, J. Burgdörfer, Phys. Rev. A 57 (1998) R1489.
[276] J.M. Feagin, J. Phys. B 28 (1995) 1495.
[277] J.M. Feagin, J. Phys. B 29 (1996) l551.
[278] J.A.R. Samson, Phys. Rev. Lett. 65 (1990) 2863.
[279] R. Wehlitz, F. Heiser, O. Hemmers, B. Langer, A. Menzel, U. Becker, Phys. Rev. Lett. 67 (1991) 3764.
[280] G. Dawber, R.I. Hall, A.G. McConkey, M.A. MacDonald, G.C. King, J. Phys. B 27 (1994) L341.
[281] M. Pont, R. Shakeshaft, Phys. Rev. A 54 (1996) 1448.
[282] A. Huetz, P. Selles, D. Waymel, J. Mazeau, J. Phys. B 24 (1991) 1917.
[283] F. Maulbetsch, J.S. Briggs, J. Phys. B 28 (1995) 551.
[284] L. Malegat, P. Selles, A. Huetz, J. Phys. B 30 (1997) 251.
[285] R. Dörner, V. Mergel, H. Bräuning, M. Achler, T. Weber, Kh. Khayyat, O. Jagutzki, L. Spielberger, J. Ullrich, R. Moshammer, Y. Azuma, M.H. Prior, C.L. Cocke, H. Schmidt-Böcking, in: E. Oks, M. Pindzola (Eds.), Atomic Processes in Plasmas, AIP Conference Proceedings Vol. 443, AIP, College Park, 1998.
[286] H.P. Bräuning, R. Dörner, C.L. Cocke, M.H. Prior, B. Krässig, A.S. Kheifets, I. Bray, A. Bräuning-Demian, K. Carnes, S. Dreuil, V. Mergel, P. Richard, J. Ullrich, H. Schmidt-Böcking, J. Phys. B 31 (1998) 5149.
[287] M. Pont, R. Shakeshaft, F. Maulbetsch, J.S. Briggs, Phys. Rev. A 53 (1996) 3671.
[288] S.P. Lucey, J. Rasch, C.T. Wheelan, H.R.J. Walters, J. Phys. B 31 (1998) 1237.
[289] A. Kheifets, I. Bray, Phys. Rev. Lett. 81 (1998) 4588.
[290] G. Schönhense, J. Hormes, in: U. Becker, D.A. Shirley (Eds.), VuV and Soft X-Ray Photoionization, Plenum Press, New York, 1996, p. 607.
[291] J. Berakdar, H. Klar, Phys. Rev. Lett. 69 (1992) 1175.
[292] J. Berakdar, H. Klar, A. Huetz, P. Selles, J. Phys. B 26 (1993) 1463.
[293] M. Achler, Ph.D Thesis, Universität Frankfurt, unpublished.
[294] R.N. Zare, Mol. Photochem. 4 (1972) 1.
[295] U. Werner, M.N. Kabachnik, V.N. Kondratyev, H.O. Lutz, Phys. Rev. Lett. 79 (1997) 1662.*
[296] H.O. Folkerts, R. Hoekstra, R. Morgenstern, Phys. Rev. Lett. 77 (1996) 3339.
[297] S. Hsieh, J.H.D. Eland, J. Phys. B 30 (1997) 4515.
[298] F. Heiser, O. Geßner, J. Viefhaus, K. Wieliczec, R. Hentges, U. Becker, Phys. Rev. Lett. 79 (1997) 2435.*
[299] E. Shigemasa, J. Adachi, M. Oura, A. Yagishita, Phys. Rev. Lett. 74 (1995) 359.

[300] A.V. Golovin, F. Heiser, C.J.K. Quayle, P. Morin, M. Simon, O. Gessner, P.M. Guyon, U. Becker, Phys. Rev. Lett. 79 (1997) 4554.**
[301] E. Shigemasa, J. Adachi, K. Soejima, N. Watanabe, A. Yagishita, N.A. Cherepkov, Phys. Rev. Lett. 80 (1998) 1622.
[302] N. Watanabe, J. Adachi, K. Soejima, E. Shigemasa, A. Yagishita, Phys. Rev. Lett. 78 (1997) 4910.
[303] D. Dill, J. Chem. Phys. 65 (1976) 1130.
[304] D. Dill, J. Siegel, J.L. Dehmer, J. Chem. Phys. 65 (1976) 3158.
[305] J.L. Dehmer, D. Dill, Phys. Rev. Lett. 35 (1975) 213.
[306] J.L. Dehmer, D. Dill, J. Chem. Phys. 65 (1976) 5327.
[307] P.M. Guyon, A.V. Golovin, C.J.K. Quayle, V. Vervloet, M. Richard-Viard, Phys. Rev. Lett. 76 (1996) 600.
[308] M. Walter, J.S. Briggs, J. Phys. B 32 (1999) 2487.*
[309] I.G. Kaplan, A.P. Markin, Sov. Phys. Dokl. 14 (1969) 36.
[310] H.D. Cohen, U. Fano, Phys. Rev. 150 (1966) 30.
[311] H. Kossmann, O. Schwarzkopf, B. Kämmerling, V. Schmidt, Phys. Rev. Lett. 63 (1989) 2040.*
[312] G. Dujardin, Phys. Rev. 35 (1987) 5012.
[313] T.J. Reddish, J.P. Wightman, M.A. MacDonald, S. Cvejanovic, Phys. Rev. Lett. 79 (1997) 2438.
[314] N. Scherer, H. Lörch, V. Schmidt, J. Phys. B 31 (1998) L817.
[315] H. LeRouzo, Phys. Rev. A 37 (1988) 1512.
[316] H. LeRouzo, J. Phys. B 19 (1986) L677.
[317] F.W. Byron, C.J. Joachain, Phys. Rev. 164 (1967) 1.
[318] J.A.R. Samson, C.H. Green, R.J. Bartlett, Phys. Rev. Lett. 71 (1993) 201.
[319] J.A.R. Samson, Z.X. He, R.J. Bartlett, M. Sagurton, Phys. Rev. Lett. 72 (1994) 3329.
[320] L.R. Andersson, J. Burgdörfer, Phys. Rev. Lett. 71 (1993) 50.
[321] A. Dalgarno, H.R. Sadeghpour, Phys. Rev. A 46 (1992) R3591.
[322] A. Dalgarno, H.R. Sadeghpour, Comm. At. Mol. Phys. 30 (1994) 143.
[323] E.G. Drukarev, Phys. Rev. A 51 (1995) R2684.
[324] Ken-ichi Hino, T. Ishihara, F. Shimizu, N. Toshima, J.H. McGuire, Phys. Rev. A 48 (1993) 1271.
[325] Ken-ichi Hino, P.M. Bergstrom, J.H. Macek, Phys. Rev. Lett. 72 (1994) 1620.
[326] T. Ichihara, K. Hino, J.H. McGuire, Phys. Rev. A 44 (1991) R6980.
[327] Z.J. Teng, R. Shakeshaft, Phys. Rev. A 49 (1994) 3591.
[328] M. Ya Amusia, A.I. Mikhailov, Phys. Lett. A 199 (1995) 209.
[329] L.R. Andersson, J. Burgdörfer, Phys. Rev. A 50 (1994) R2810.
[330] T. Surić K. Pisk, B.A. Logan, R.H. Pratt, Phys. Rev. Lett. 73 (1994) 790.
[331] M.A. Kornberg, J.E. Miraglia, Phys. Rev. A 53 (1996) R3709.
[332] L. Spielberger, O. Jagutzki, R. Dörner, J. Ullrich, U. Meyer, V. Mergel, M. Unverzagt, M. Damrau, T. Vogt, I. Ali, Kh. Khayyat, D. Bahr, H.G. Schmidt, R. Frahm, H. Schmidt-Böcking, in: L.J. Dubé J.B.A. Mitchell, J.W. McConkey, C.E. Brion (Eds.), The Physics of Electronic and Atomic Collisions, AIP Conference Proceedings, Vol. 360; 1995, p. 773.
[333] L. Spielberger, Ph.D Thesis, Universität Frankfurt, Shaker Verlag, Aachen, 1997, ISBN 3-8265-2607-4.
[334] H. Bethe, Ann. Physik 5 (1930) 325.
[335] J.A.R. Samson, Z.H. He, W.C. Stolte, J.N. Cutler, J. Electron Spectrosc. & Relat. Phenom. 78 (1996) 19.
[336] U. Becker, G. Prümper, J. Viefhaus, M. Wiedehöft, C.J. Levin, I.A. Sellin, Austr. J. Phys., 1999, in print.
[337] R. Wehlitz, R. Hentges, G. Prümper, A. Farhat, T. Buslaps, N. Berrah, J.C. Levin, I.A. Sellin, U. Becker, Phys. Rev. A 1996 (53) R3720.
[338] L.R. Andersson, J. Burgdörfer, in: T. Andersen, B. Fastrup, F. Folkmann, H. Knudsen, N. Andersen (Eds.), The Physics of Electronic and Atomic Collisions, AIP Conference Proceedings, Vol. 295, 1993, p. 836.
[339] L.R. Andersson, J. Burgdörfer, Phys. Rev. A 50 (1994) R2810.
[340] T. Surić, K. Pisk, R.H. Pratt, Phys. Lett. A 211 (1996) 289.
[341] P.M. Bergstrom Jr., K. Hino, J. Macek, Phys. Rev. A 51 (1995) 3044.
[342] T. Beier, G. Plunien, G. Soff, Hyperfine Interactions 108 (1997) 19.
[343] Th. Stöhlker et al., Hyperfine Interactions 108 (1997) 29.
[344] H. Person, S. Salomonson, P. Sunnergren, I. Lindren, M. Gustavson, Hyperfine Interactions 108 (1997) 3.

[345] R. Gayet, J. Hanssen, L. Jacqui, J. Phys B 28 (1995) L2193.
[346] R. Gayet, J. Hanssen, L. Jacqui, M.A. Ourdane, J. Phys B 30 (1997) 2209.
[347] W. Fritsch, C.D. Lin, Phys. Rev. Lett. 61 (1988) 690–693.
[348] F. Kurp, Th. Tschentscher, F. Bell, J.R. Schneider, Europhys. Lett. 35 (1996) 61.
[349] J.B. Watson, A. Sanpera, D.G. Lappas, P.L. Knight, K. Burnett, Phys. Rev. Lett. 78 (1997) 1884.
[350] G. Möllenstedt, H. Düker, Naturwiss 42 (1954) 41.
[351] G. Möllenstedt, H. Düker, Zeitschrift für Physik 145 (1954) 377.
[352] A. Einstein, B. Podolsky, N. Rosen, Phys. Rev. 47 (1935) 777.
[353] J.A. Wheeler, H. Zurec (Eds.), Quantum Theory and Measurement, Princeton University Press, Princeton, 1983.
[354] M. Jammer, The conceptural development of quantum mechanics, McGraw-Hill, New York 1966.
[355] M. Jammer, The Philosophy of Quantum Mechanics, Wiley, New York, 1974.
[356] W.K. Wootters, W.H. Zurek, Phys. Rev. D 19 (1979) 473.
[357] G.W. Rodenback, J.S. Allen, Phys. Rev. 86 (1952) 446.
[358] R. Davis, Phys. Rev. 86 (1952) 976.
[359] J.S. Allen, Phys. Rev. 61 (1942) 19 692.
[360] G.W. Rodenback, J.S. Allen, Phys. Rev. 83 (1951) 215.
[361] Ch. Weinheimer et al., Phys. Lett. B 300 (1993) 210.
[362] S. Wolf, H. Helm, Phys. Rev. A 56 (1997) R4385.
[363] J. Berakdar, S.N. Samarin, R. Herrmann, J. Kirschner, Phys. Rev. Lett. 81 (1998) 3535.
[364] J. Kirschner, O.M. Artamonov, A.N. Terekhov, Phys. Rev. Lett. 69 (1992) 1711.
[365] J. Kirschner, O.M. Artamonov, S.N. Samarin, Phys. Rev. Lett. 75 (1995) 2424.